The Fact Of Fractal Tennis: The Universe As A Fractal Computer Defined by the Star=Electron+Atom=Galaxy Quine

Steven E. Elliott

May 2026

Abstract

We propose a new principle of physics—MATHICCS—requiring that every mathematical axiom used in a physical law must correspond to an operation persistently realizable by a physical subsystem. Applying this criterion motivates reality's geometry as a discrete, self-similar, singularity-free structure: the Apollonian–Soddy Sphere Packing (ASSP). We conjecture that 3D dynamics on this packing is a self-computing fractal: a dynamical computer whose registers are fractal-congruent objects that process angular and linear momentum as cross-scale registers. This fractal quine is proposed as a self-consistent, MATHICCS-valid physical theory. It gives zero-free-parameter derivations of the baseline fine-structure constant $\alpha^{-1}_{\mathrm{TFOFT}} = 4\pi^3 + \pi^2 + \pi = 137.036$, the electron–star logarithmic mass hierarchy, the electron mass, the proton mass, the proton/electron mass ratio, the 77-layer self-encoding register, the hydrogen binding energy, the hydrogen spectral ladder, and the gravitational constant G from atomic structure by two independent first-principles routes. We present empirical cross-checks involving the observed electron–star hierarchy, dark/visible channel fractions 23/27 and 4/27, Fermi-bubble morphology, the 25-arcminute CMB seam, and the near-match between Karlsson quasar logarithmic periodicity and the derived Info-channel leakage. The Karlsson complement also gives a 77-layer mass-channel spot check inside the same 137–139 register interval. We present one pending falsifiable prediction, $\alpha^{-1}_{\mathrm{Yb}} = 137.035998945 \pm 0.000000045$. The framework is presented as a nearly zero free-parameter ontology whose derived consequences are compared against major tensions in observational physics.

1 Principles: The Motivation for MATHICCS

1.1 The Problem: Operational Constraints on Physical Axioms

Modern physics often employs mathematical structures whose physical realization is left implicit. Consider:

1. **Completed infinities** ($\mathbb{N}$ as a finished object): These are invoked in standard analysis and set theory but cannot be instantiated by any physical clock, apparatus, or experiment.
2. **Limit operations at infinity** ($t \to \infty$, $V \to \infty$): No experiment can directly verify behavior at infinite time or volume.
3. **Infinitesimal quantities and derivative-based formalisms**: Defined by ϵ-δ limits that assume completion of infinite sequences.
4. **Infinitely many degrees of freedom in field theory**: The continuum treats space as uncountably many points, exceeding what can be physically instantiated.

5. **Black-hole singularities**: Divergent density and curvature indicate the model has left its domain of operational validity.

These examples motivate a stricter criterion: a mathematical structure is physically admissible only if its defining operations can be realized by a persistent physical procedure.

1.1.1 General Relativity and the DeSitter Collapse of Operational Clocks

General relativity with $\Lambda > 0$ predicts that expanding FLRW solutions generically approach a de Sitter-like late-time regime consistent with the observed cosmological constant [2]. In de Sitter space the Gibbons–Hawking temperature [3]

$$T_{\rm dS} = \frac{\hbar c}{2\pi k_B}\sqrt{\frac{\Lambda}{3}}$$

implies that finite-energy localized configurations are immersed in a horizon-temperature environment. A clock or apparatus of finite energy E therefore has no eternal external reservoir from which to maintain, rebuild, or refine its operations. The de Sitter horizon sets the characteristic late-time decay rate and horizon time scale

$$\gamma_\Lambda \sim c\sqrt{\frac{\Lambda}{3}}, \qquad \tau_\Lambda \sim \gamma_\Lambda^{-1}.$$

This loss is not limited to freely expanding, unbound regions. Gravitationally bound systems do not provide permanent exceptions. In classical GR, all nonstationary bound mass distributions carry time-dependent multipole structure, radiate gravitational waves, inspiral, and therefore lack eternally stable orbits. Bound gravitational motion is therefore a long-lived but finite reservoir of usable mechanical free energy, not a permanent foundation for an eternal limiting procedure.

The local inertial frame in GR also exhibits ordinary radiative physics. The Einstein Equivalence Principle asserts that, in a sufficiently small neighborhood of any event, nongravitational physics reduces to its special-relativistic form on the local Minkowski tangent frame. Thus the same local frame used to define clocks and rods also contains the usual Maxwell and Standard Model radiation channels: accelerated charges radiate by the Larmor channel; neutral but structured matter radiates through time-dependent electric and magnetic multipoles; rotating magnetic configurations lose energy through magnetic dipole radiation; and electroweak processes can carry energy away through neutrinos.

The constructibility argument. The Einstein Equivalence Principle requires that *at any spacetime point, in any state of motion*, one can *construct* a local inertial frame by performing the limiting procedure of building ever-smaller apparatus. This is a **constructibility** claim, not a maintenance claim. The distinction matters.

For any finite energy $E > 0$, define $T_{\rm construct}(E)$ as the cosmic time after which it becomes impossible to construct—not merely maintain—a clock of energy E at an arbitrary point in the expanding spacetime. Because the de Sitter decay rate is nonzero, because bound mechanical stores are radiatively unstable in generic nonstationary configurations, and because the accessible comoving volume available for apparatus construction shrinks due to the cosmological horizon, $T_{\rm construct}(E)$ is finite for every $E > 0$:

$$\exists\, T_{\rm construct}(E) < \infty \quad \forall\, E > 0.$$

Hence no clock of energy E can be constructed everywhere in the universe after cosmic time $T_{\rm construct}(E)$. The set of spacetime regions in which a valid ε-δ measurement apparatus can be *constructed* therefore shrinks to measure zero:

$$\mathcal{V}_{\rm constructible}(t) \to 0 \quad \text{as} \quad t \to \infty.$$

Why the local limit does not rescue EEP. The usual defense of EEP is a spatial limiting argument. In a small freely falling laboratory of characteristic size L, curvature effects enter through tidal terms, schematically

$$\epsilon_{\text{tidal}}(L) \sim RL^2,$$

so the metric becomes Minkowskian to arbitrarily good accuracy as $L \to 0$. This is the standard reason one says curvature can be transformed away at a point.

MATHICCS asks a different question: can the limiting procedure itself be physically constructed and repeated inside the universe described by the same theory? The limit $L \to 0$ is not a magic symbol. It is a sequence of apparatus constructions, synchronizations, refinements, and readouts. In a universe with $\Lambda > 0$, the accessible region and usable free energy available for such constructions shrink exponentially with cosmic time, and the usable free-energy reservoir available for repeated apparatus construction is correspondingly depleted. Thus the physical support of the EEP limiting procedure is time-dependent. The conflict is between two scalings. Spatially, the local inertial approximation improves quadratically:

$$\epsilon_{\text{tidal}}(L) \sim RL^2.$$

Temporally, the set of regions in which the required apparatus can be constructed shrinks exponentially under de Sitter horizon dynamics:

$$\mathcal{V}_{\text{constructible}}(t) \sim \mathcal{V}_0 e^{-\gamma t},$$

for some positive effective decay rate γ. The exact coefficient is not important here; the important point is that the constructible domain decreases monotonically to zero while the EEP limit requires an indefinitely repeatable physical construction.

Thus EEP wins only as a formal spatial limit at fixed time. It does not win as a persistent physical axiom over the full future history of a $\Lambda > 0$ universe. As $t \to \infty$,

$$\mathcal{V}_{\text{constructible}}(t) \to 0,$$

so the limiting procedure required to realize $L \to 0$ has no positive-measure domain left on which to operate. In this sense, EEP holds nowhere in the MATHICCS sense at future infinity: the formal tangent space can still be written down, while the physical procedure that gives the tangent space operational meaning can no longer be instantiated.

The long lifetime of macroscopic clocks delays the collapse of the constructible domain. A finite de Sitter horizon time scale still gives an expiring supply of physical realizers, so foundational axioms cannot depend on arbitrarily prolonged apparatus construction.

This can be stated as a clean theorem-like result:

> **Theorem-like statement.** In any spacetime with $\Lambda > 0$, the standard EEP argument gives a local spatial limit, not a persistent physical realizer. Curvature errors inside a laboratory of size L fall as $O(L^2)$, but the positive-measure domain in which the required sequence of ever-smaller laboratories can be constructed decays to zero exponentially over cosmic time. Therefore, for every finite apparatus energy $E > 0$, there exists a finite cosmic time $T_{\text{construct}}(E)$ after which the constructive limiting procedure required by EEP cannot be carried out at an arbitrary spacetime point. Gravitational binding can delay this failure but cannot eliminate it, because generic bound systems radiate and realistic local matter fields leak energy through electromagnetic and weak channels. EEP is therefore not a MATHICCS-valid foundational axiom: it is an approximation with a finite domain of constructive validity. General relativity with $\Lambda > 0$ is operationally self-limiting under MATHICCS.

1.1.2 The Role of External Formalism

Independence results in set theory, Gödel incompleteness, and non-constructive continuum assumptions indicate that not every mathematically coherent object is automatically physically realizable [4].

MATHICCS does not invalidate calculus as a computational tool. It distinguishes ontological claims (the continuum *is* reality) from effective approximations (the continuum *describes* reality to bounded error). A computable calculus grounded in fractal sphere geometry is fully MATHICCS-valid.

1.2 MATHICCS: The Operational Criterion

We propose the following criterion.

> A mathematical axiom is physically valid if and only if there exists a physical subsystem that can instantiate the operation described by the axiom and do so persistently under the evolution laws of the system partially or wholly described by that same axiom.

This criterion is called MATHICCS: *Mathematical Axioms That Have Infinitely Complete Computable Sanity.*

1.2.1 Definition 1: Mathematical Process P

A mathematical process P is any logical operation that appears in an axiom (quantifier, limit, smoothness assumption, cardinality statement, integral, etc.).

1.2.2 Definition 2: Internal Realizer

An internal realizer is a subsystem S composed of clocks, apparatus, and protocols that can instantiate process P to arbitrary finite precision, with precision arbitrarily improvable by expanding S.

1.2.3 Definition 3: Internal Persistence

Process P has internal persistence if there exists a positive-measure set of initial states under which the creation of realizers of P survives indefinitely under the evolution laws dictated by the axioms containing P.

1.2.4 Definition 4: MATHICCS Axiom M1 — Operational Validity

An axiom A containing process P is MATHICCS-valid only if P has internal persistence. This is the Elliott Math Stability Rule (EMSR).

1.2.5 Definition 5: MATHICCS Axiom M2 — Internal Realization

Physical meaning requires demonstration of internal realization. Axioms drawn purely from external set theory, Peano arithmetic, ZFC, large cardinals, or completed ϵ-δ limit processes are not physically admissible unless grounded in a physical subsystem. This is the Internal Realization Requirement (IRR).

1.2.6 Definition 6: MATHICCS Axiom M3 — Ontological Self-Consistency

An ontology O is valid only if all axioms in O satisfy M1 and M2 simultaneously. An ontology that is MATHICCS-valid and matches universal observations to bounded error satisfies the ontological-epistemological equivalence principle (OEEP).

1.3 Why Self-Describing Systems Must Be Gödel-Free

A self-describing physical system is one in which the laws governing the system are themselves encoded as structures within the system. This is the setting in which MATHICCS applies: the realizers of the axioms must persist under the laws those axioms describe.

> **Theorem (Informal):** A MATHICCS-valid self-describing system cannot be governed by an axiomatic system subject to Gödel incompleteness.

Argument. Suppose the system $\mathcal{U}$ is described by an axiomatic system $\mathcal{A}$ that is Gödel-incomplete. Then there exists a true statement S about $\mathcal{U}$'s dynamics that $\mathcal{A}$ cannot prove. But $\mathcal{U}$ must physically realize its own dynamics, including the dynamics described by S. This means that $\mathcal{U}$ performs an operation that its own descriptive language cannot validate. Under M1 any operation in $\mathcal{U}$ must be persistently realizable. A MATHICCS-valid self-describing system is therefore naturally modeled by a complete, consistent, decidable axiomatic framework.

Among known arithmetic systems, Presburger arithmetic (addition and order only, without general multiplication) is complete, consistent, and decidable [5]. These properties make it a natural candidate for the internal arithmetic of a self-describing physical theory.

2 Fractal Law: From MATHICCS to Fractal Geometry

2.1 Why MATHICCS Motivates a Fractal Substrate

2.1.1 Step 1: Replace the Continuum

Standard physics uses $\mathbb{R}$ as the arena for continuous fields, while fractal geometry provides a well-developed language for scale-recursive structures in nature [6, 7]. However, $\mathbb{R}$ is a completed infinity: it contains uncountably many points with no constructive specification. Under M2 this is not an automatically admissible physical assumption. A possible alternative is a recursively refinable discrete structure. At level n there are N_n discrete positions; at level $n+1$ there are $N_{n+1} = kN_n$ for some $k > 1$. This replaces completed infinity with unbounded recursion.

2.1.2 Step 2: Require Persistent Structure

For a physical subsystem to persist, its construction must be stable under evolution. Continuous fields can develop singularities, while discrete self-similar structures avoid such singular points at every scale. This makes self-similar discrete geometry an attractive candidate for a MATHICCS-valid substrate.

2.1.3 Step 3: Fractal Conclusion

Taken together, these considerations suggest that a universe governed by MATHICCS should be discrete at finite resolution, self-similar across scales, stable under its own dynamics, and determined by local tangency relations. The appropriate coarse description of reality is therefore an unbounded fractal with no preferred smallest or largest scale.

2.1.4 Step 4: Empirical Selection by Dual Monofractal Scaling

The underlying geometry is selected by combining the MATHICCS requirement with the observed dual monofractal pattern in multiple dynamical systems. The 3D bulk channel repeatedly exhibits Soddy Sphere Packing-like scaling near $D_S \approx 2.477$, while 2D boundary layers, radial cuts, rotational interfaces, and shell-like transport channels repeatedly exhibit Apollonian Circle Packing-like scaling near $D_A \approx 1.305$. A substrate built from recursive tangent spheres naturally contains both channels in the same object: the 3D packing supplies the bulk Soddy

family, and the boundary/interface cuts supply the Apollonian family. Thus the Apollonian Soddy Sphere Packing is proposed as the minimal MATHICCS-valid candidate for a singular fundamental law because it gives one recursive mechanism for the two main exponent families observed in reality.

3 Evidence For The Dynamic Apollonian Soddy Sphere Packing

The main area where non-power-law dynamics are expected to arise is the scale-crossing boundary of a fractal, where one self-similar layer transfers energy into another. The empirical case for atom–galaxy fractal congruence, including a $\sim 31\%$ viscous-drag signature consistent with a $\lambda \sim 10^{31}$ scaled electron-shell contribution to stellar orbital dynamics, was first developed in an earlier paper [8].

The motivation stems from comparing flat galactic rotation curves with atomic emission: spiral galaxies, including the Milky Way and Andromeda, show orbital speeds that remain approximately constant over large radial ranges rather than falling in the Keplerian manner expected from visible baryons alone [9, 10], while atoms emit photons only at discrete transition frequencies with $E_{\text{photon}} = h\nu$.

Within the present hypothesis, both phenomena are scale-crossing transfer laws. The atom supplies the lower-scale electron-to-photon channel, while the galaxy core supplies the higher-scale star-to-macrophoton channel. The flat rotation curve is therefore interpreted as the lower-scale projection of a quantized higher-layer transfer process.

3.1 Power Laws and the Apollonian-Soddy Fractal Dimension

3.1.1 Why The Apollonian Soddy Sphere Packing (ASSP)?

A self-similar discrete packing is a natural candidate for a three-dimensional geometry that is simultaneously dense, recursive, and free of singular points, in the spirit of classical fractal geometry and Apollonian packing theory [6, 11, 12, 13]. Sphere packings admit recursive nesting, avoid edge singularities, and can be specified locally through tangency relations. Among such packings, the Apollonian–Soddy sphere packing is distinguished by its exact recursive geometry and by the determinacy of the Descartes–Soddy curvature relation [14, 11, 12].

The empirical selection criterion is the dual monofractal power-law pattern. The same dynamic substrate must generate both the Soddy-like 3D bulk exponent family and the Apollonian-like 2D boundary/interface exponent family. The ASSP has this structure internally: the full sphere packing supplies recursive 3D bulk scaling, while tangent boundaries, radial cuts, and rotational interfaces supply the corresponding 2D Apollonian projections. The proposed substrate is therefore selected by the combination of finite recursive realizability and observed dual-channel monofractal scaling.

More precisely:

- **Perfect self-similarity**: the packing in any region is identical to the packing at any scale, up to constant rescaling.
- **Determinate geometry**: given mutually tangent spheres, the Soddy curvature relation determines subsequent configurations uniquely up to reflection.
- **Dual-channel scaling**: the same recursive object contains a 3D Soddy bulk channel and 2D Apollonian boundary/interface channels.

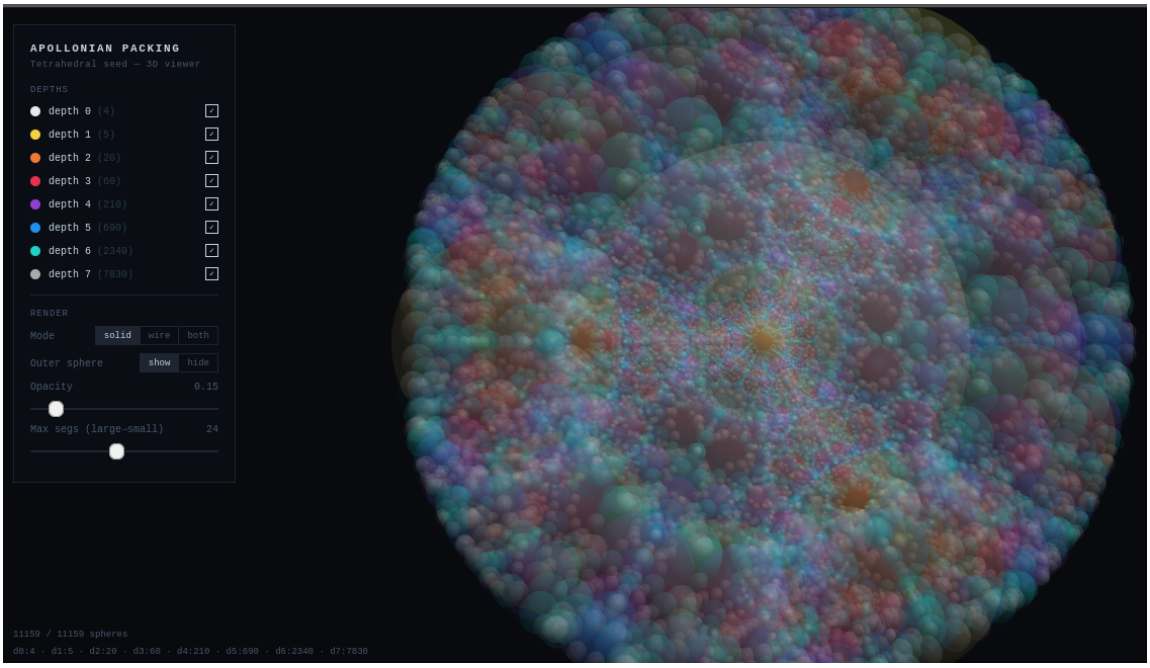

Figure 1: Opaque outline of the tetrahedral seed generating the Soddy cores inside the virtual outer Soddy sphere.

Credit: Generated by Steven E. Elliott.

3.1.2 Observed Fractal Dimensions

Across a wide range of systems in physics, biology, economics, and geophysics, power-law exponents frequently cluster near values associated here with Apollonian and Soddy-type recursive geometries [6, 13, 11, 15, 16]:

- $\alpha \approx 1.3$: Apollonian gasket dimension ($D_A \approx 1.3057$)
- $\alpha \approx 1.9$: mixed Apollonian–Soddy midpoint ($D_{\text{mix}} = (D_A + D_S)/2 \approx 1.8898$)
- $\alpha \approx 2.47$: Soddy sphere packing dimension ($D_S \approx 2.4739$)

In ordinary critical phenomena, power laws usually appear near a special transition, with finite correlation length, finite scaling window, and system-specific universality class. A truly scale-independent recurrence across astrophysical, geophysical, biological, chemical, and informational systems points to a different kind of explanation: a monofractal generator, or a tightly coupled dual projection of one generator. In the present proposal the generator is the same Apollonian–Soddy recursive packing seen in three ways: the 3D bulk packing gives Soddy-like exponents near $D_S \approx 2.4739$, the 2D boundary layers, radial cuts, and rotational interfaces give Apollonian-like exponents near $D_A \approx 1.3057$, and coupled boundary–bulk observables fall near the midpoint $D_{\text{mix}} \approx 1.8898$.

This is why the distinction between the exponent families matters. Power-law exponents near $D_A \approx 1.3$ recur specifically in systems with radially defined, boundary-dominated, or rotationally dominated dynamics, such as river networks, coastlines, galactic two-point correlation functions, and shell-like transport structures. Exponents near $D_S \approx 2.47$ recur in bulk filling, branching, packing, or filamentary systems, such as cosmic web density, interstellar structure, stellar mass functions, lung branching, and QCD-like confinement scaling. Exponents near $D_{\text{mix}} \approx 1.89$ mark coupled boundary–bulk observables: systems where the measured statistic mixes surface transport with volumetric packing. Under TFOFT these are the 2D boundary, mixed boundary–bulk, and 3D bulk expressions of the same ASSP generator.

3.1.3 Universal Power-Law Table

Table 1: Representative power laws across multiple domains, grouped by their proximity to Apollonian, mixed Apollonian–Soddy, or Soddy scaling.

System	**Exponent**	**Fractal D**	**Type**
Astrophysical and Cosmological			
Galaxy two-point correlation function	1.77	≈ 1.89	Apollonian/Soddy
Cosmic web filament density profile	≈ 2.4	≈ 2.47	Soddy
Interstellar medium density fluctuations	≈ 2.4	≈ 2.47	Soddy
Dark matter halo mass function	1.8–2.0	≈ 1.89	Apollonian/Soddy
Stellar mass function / IMF (Salpeter)	2.35	≈ 2.47	Soddy
Solar wind turbulence spectrum	$5/3 \approx 1.67$	≈ 1.89	Apollonian/Soddy
Cosmic ray energy spectrum	≈ 2.7	≈ 2.47	Soddy
Asteroid size distribution	≈ 2.5	≈ 2.47	Soddy
Geophysical and Environmental			
Earthquake energy (Gutenberg–Richter)	1.8–2.2	≈ 1.89	Apollonian/Soddy
Forest fire size distribution	1.3–1.9	≈ 1.89	Apollonian/Soddy
River network branching (Horton's law)	≈ 1.2	≈ 1.30	Apollonian
Coastline fractal dimension (global avg)	≈ 1.2	≈ 1.30	Apollonian
Physical and Chemical			
Turbulent energy spectrum (Kolmogorov)	≈ 1.67	≈ 1.89	Apollonian/Soddy
Crack propagation / fracture events	1.2–2.0	≈ 1.89	Apollonian/Soddy
Magnetic Barkhausen noise	1.3–1.8	≈ 1.89	Apollonian/Soddy
QCD flux tube / confinement scaling	≈ 2.4	≈ 2.47	Soddy
Biological			
Neuronal avalanche sizes in cortex	≈ 1.5	≈ 1.30	Apollonian
Neural dendritic arbor dimension	1.2–1.4	≈ 1.30	Apollonian
Lung bronchial branching	≈ 2.4	≈ 2.47	Soddy
Gene regulatory network connectivity	2–3	≈ 2.47	Soddy
Human, Social, and Informational			
Word frequency distributions (Zipf)	1–2	≈ 1.89	Apollonian/Soddy
City size distributions (Zipf)	1–2	≈ 1.89	Apollonian/Soddy
Wealth distribution (Pareto tail)	1.5–3	≈ 1.89–2.47	Apollonian/Soddy
Internet topology	2–3	≈ 2.47	Soddy

3.1.4 Conclusion: The Fractal Dimension Argument

A singular fundamental law of the universe that produces the same power-law families across many physical scales must act as a monofractal generator. The repeated appearance of the same exponents in astrophysical, geophysical, biological, chemical, and informational systems is not a collection of unrelated coincidences; it is the visible scaling signature of the same recursive rule operating through different boundary conditions.

The ASSP supplies such a generator with one ontology rather than many fitted mechanisms. Its 3D bulk recursion produces Soddy-like scaling, while its 2D boundary cuts and radial interfaces produce Apollonian-like scaling. The observed pattern is therefore consistent with a single fractal law appearing as a dual projection: bulk versus boundary, 3D packing versus 2D interface. This is the empirical basis for the conjecture stated in Section 4.

4 Prior Fractal Physics and the Closure Problem

4.1 A Survey of Fractal Physics Attempts

Fractal geometry has attracted serious attention in physics for decades. Each approach captured part of the truth, but none reached the full self-computing picture. A brief survey:

- **Mandelbrot (1977–1983):** Established that natural systems exhibit fractal geometry; identified power-law scaling and self-similarity as universal features, but offered no dynamical mechanism [6].
- **Garnet Ord / Chaos theory QM (1983):** Showed that random walks on fractal lattices recover structures analogous to relativistic quantum mechanics; insightful but external rules imposed, not self-generated [17]. This result provides important mathematical support for the TFOFT framework.
- **Halton Arp's intrinsic redshift / fractal cosmology (1987–):** Observed that quasar redshift clusters at preferred values and argued against the Big Bang space expansion metric; the logarithmic periodicity is historically associated with Karlsson's preferred-redshift relation [18, 19], but no mechanism for the discretization was provided.
- **Nottale's Scale Relativity (1992–):** Extended relativity to non-differentiable, fractal spacetime and derived quantum-like behavior from fractal geodesics [7]; formally elegant but still grounded in the continuum and limit operations, violating M1. The theory identified the physical law as fractal but did not define congruent physically fractal objects, leaving M3 unaddressed.
- **El Naschie's E-infinity theory (1990s–2000s):** Proposed that spacetime has a fractal Cantorian microstructure with dimension related to the golden ratio; derived $\alpha^{-1} \approx 137$ from Cantorian set theory [20], but relied on completed infinities and non-constructive objects, violating MATHICCS M2.
- **Lestone's string-surface model and α (2007):** Proposed that the fine-structure constant emerges from a heuristic string-like particle-surface model constrained by assumptions inspired by Apollonian circle packing geometry [21]. This yields $\alpha \approx 1/137.04$ without peer review or independent confirmation. It remains the closest geometric precursor to the ASSP but lacks any computational architecture, self-referential quine mechanism, or explicit fractal congruent objects.

4.2 Ord's Fractal Space-Time and the Star-Electron Congruence

Garnet Ord (1983) starts from the observation that quantum particle paths are highly irregular and non-differentiable when examined at fine enough scales, and constructs a fractal spacetime analogue of relativistic quantum mechanics [17]. He constructs a continuous but fractal trajectory in spacetime (exemplified by a space-filling Peano-Moore curve with Hausdorff dimension exactly 2 instead of the classical dimension 1). The particle is confined to move on these fractal paths in both space and time. This geometric setup naturally reproduces key quantum features: the uncertainty principle, the de Broglie relation, interference effects, and aspects of relativistic quantum mechanics — all without invoking the full machinery of the Schrödinger equation or path integrals from the start.

This provides direct mathematical support for the cross-scale congruence between hyper-velocity stars and free electrons in TFOFT. The dynamics of intergalactic hyper-velocity stars act like random walks on fractal lattices due to the fractal-like large-scale observed cosmic web structure.

4.3 The Closure Problem: The Fractal Quine

The theories surveyed above establish important parts of the fractal-physics program. The remaining closure problem is self-reference: the fractal law must be encoded, transmitted, and enforced by objects inside the same fractal system.

A complete fractal ontology must answer the deeper question: **where do the rules come from, and how does the system enforce them on itself?**

The answer requires three ingredients:

1. **A MATHICCS-valid axiomatic foundation** (Presburger arithmetic [5]) that is complete, consistent, and decidable—so the system can describe its own operations without Gödel breakage or non-provable, non-physical, non-testable, external processes.

2. **A self-computing architecture.** Fractal-congruent objects in a fluid-like dynamical system may chaotically evolve into a self-annealing, AI-like computer system [22, 23]; this is mathematically plausible because Euler fluids have been shown to support Turing-complete computation on suitable manifolds [24, 25]. In the present proposal, the dynamical ASSP is the prior structure: the fractal geometry defines the allowed dynamics, rather than mechanical dynamics generating the fractal as an emergent pattern.

3. **The photonic mechanism.** The identification of galaxies with atoms reveals the underlying dynamics for (macro)photon emission as electrons/stars colliding with atomic/galactic cores and (macro)photon absorption as incoming core jets coalescing back into electrons/stars.

5 The Presburger–ASSP Register Basis and Derived Constants

Status of Claims

This paper combines established mathematical structure with new physical identifications and conjectures. The categories used throughout are:

- **Established background:** standard mathematical and physical results such as Presburger decidability, the Descartes–Soddy relation, Apollonian packing structure, and measured observational quantities.

- **Definitions:** terminology introduced by the present paper, including Star Ball, Core Ball, Gyro Ball, Info Ball, Dust Ball, and the Presburger–ASSP machine, named the Fractal Tennis Computer (FTC) at the start of the machine section below.

- **Conjectures:** proposed identifications between the ASSP structure and observed systems, including star/electron congruence, atom/galaxy congruence, dark matter as lower-scale substrate, and force channels as tangency orders.
- **Derived quantities:** quantities obtained internally from the ontology and cost model, including $T_{\text{sphere}} = 4\pi^3 + \pi^2 + \pi$, $\alpha_{\text{TFOFT}}^{-1} = T_{\text{sphere}}$, the rank-23 channel split, the half-boundary mass register, and the resulting 77-layer closure.

Notation distinguishes internally derived quantities (TFOFT) from observed astrophysical/cosmological quantities (obs) and laboratory measurements (meas).

Thus $k_{\text{mass}}^{\text{TFOFT}}$, $T_{\text{mass}}^{\text{TFOFT}}$, and $S_{\text{mass}}^{\text{TFOFT}}$ are ontology-internal quantities, while $\ln(M_\odot/m_e)_{\text{obs}}$, G_{meas}, and α_{meas} are observational or laboratory comparison values.

5.1 The Fractal Tennis Computer (FTC)

Granting dynamics to the ASSP fractal via no-slip gearing of the spheres, creates the Presburger—ASSP computational machine which is hereafter called the **Fractal Tennis Computer** (FTC). The FTC is the self-computing ASSP register system whose active objects are Star Balls, Core Balls, Gyro Balls, Info Balls, Dust Balls, and their boundary channels. The name emphasizes the dynamical picture: angular-momentum information is served, received, reflected, and reconstructed across tangent spherical registers, while the computational cost of each transfer is paid into lower-scale linear-momentum substrate.

Standard mathematical formulations of the Standard Model and General Relativity are normally expressed using continuum analysis and arithmetic strong enough to fall within the scope of Gödel-style incompleteness results [4]. These systems cannot prove all true statements about their own arithmetic, creating a fundamental barrier to self-description. In contrast, Presburger arithmetic (addition and order only, without general multiplication) is complete, consistent, and decidable [5]. Multiplication by a *constant* is implemented via repeated addition and is therefore valid; only variable-by-variable multiplication requires indirection. As established in Section 1.3, a MATHICCS-valid self-describing universe is naturally modeled by this arithmetic.

The dynamical Apollonian-Soddy sphere packing operating under Presburger arithmetic is conjectured to constitute a universal computational machine. Unlike the idealized infinite-tape Turing machine, the ASSP machine operates on *finite but recursively expandable tape*, closer in spirit to finite physical computation and self-reproducing automata [22, 26, 23]. At each fractal layer N, the accessible substrate is a locally finite sphere packing with a bounded number of active tangencies. When those tangencies are exhausted, the machine descends to layer $N-1$, adding a finite increment of new capacity. Each expansion step is governed by the Soddy curvature relation, which is a decidable, closed-form computation.

5.1.1 Why the FTC Is Gödel-Free

Gödel incompleteness applies to sufficiently expressive formal systems that internalize arithmetic over completed infinite domains and support the fixed-point machinery needed for diagonal self-reference [4]. The FTC is constructed to avoid precisely that internalization. Its arithmetic core is Presburger arithmetic: addition, order, finite indexing, and finite combinatorial structure, without primitive variable-by-variable multiplication as a completed total operation [5].

The important point is not that the machine has an indefinitely extendable tape in the Turing-machine sense. It does not contain an actually completed unbounded tape as an internal object. At every stage the active substrate is a finite Soddy tangency configuration with finite addresses, finite local neighborhoods, finite proof chains, and finite computation traces. Further refinement is allowed only as a new finite trace step governed by the Soddy curvature relation. The limit of endless refinement is a boundary idealization, not an internal domain of quantification.

Thus the FTC uses potential infinity rather than completed infinity. One may always perform another finite refinement, descend one more fractal layer, or extend a finite address by one more symbol. But the completed infinite branch, the completed graph of multiplication, the completed set of all traces, and the completed self-referential fixed point are not admitted as internal objects. Finite cells and finite traces are internal, while the limiting Cantor-dust boundary of possible completions remains external and non-internal.

The fractal quine derived in Section 5.4 requires approximately 77 recursive log-steps (derived in Section 6.1) to complete one self-encoding cycle. These 77 steps are not an appeal to an infinite tape. The machine reads and writes a finite number of Soddy tangency states, executes a finite number of Presburger-valid additions and comparisons, and terminates in a new finite configuration at the next scale layer. After the cycle, the machine has reproduced the relevant register pattern, but it has not quantified over an infinite set or completed a total recursive universe.

> **Axiom P3 (Finite Trace Extension):** A MATHICCS-valid self-describing machine executes only finite trace steps over finite Soddy tangency configurations. Each refinement step must have a finite address, a finite local rule, and a decidable Presburger description. Recursive extension is potential: the system may always generate a further finite trace, but it never internalizes the completed infinity of all traces, all branches, or all self-referential fixed points. The FTC satisfies this through local fractal refinement governed by the Soddy curvature relation. Gödel incompleteness does not obstruct this physical execution because the machine never performs unbounded quantification over a completed infinite domain and never admits the completed diagonal object as an internal state.

This distinction explains why QFT and GR are not MATHICCS-valid in the sense of M2: both employ completed real-number continua and mathematical induction over completed infinite domains. The FTC does not deny approximation, convergence, recursion, or analysis. It rejects the promotion of arbitrary nonconstructive limits into internal physical objects. Its computations are finite traces on finite tangency states, with further refinement always possible but never completed.

5.2 Basis Radius Selection: Physical Word Size and Presburger Cost Minimization

Presburger arithmetic lacks general variable multiplication; all operations reduce to repeated addition and finite symbol manipulation. In the FTC, every symbol, operation, and lookup constitutes a physical computational cost.

Numbers as programs; the word-size question. A critical clarification is required before the cost model can be stated. MATHICCS contains no abstract numbers. Every quantity in the FTC is a *physical program or circuit* executed by the substrate of no-slip rotating spheres in a sphere packing. The symbol "π" is not a transcendental real number imported from external mathematics; it is the program that a sphere executes when it reports its own circumference-to-diameter ratio—a directly and persistently realizable physical operation on the substrate.

The analogy to digital computing is precise. On a digital circuit, `u32(1)` and `u8(1)` are not the same object even though both represent the concept of "one." The word size is determined by the physical register, not by abstract arithmetic. Asking whether π is "allowed" in Presburger arithmetic commits the same error as asking whether a 32-bit register is "allowed" to hold a value that doesn't fit in 8 bits: it confuses the arithmetic with the hardware. In the FTC, the physical registers are literal spheres undergoing no-slip rotation in a sphere packing. The natural *word size* of this substrate—the primitive quantity that every physical operation either

reads or writes—is the sphere itself. The sphere's intrinsic dimensional unit is its radius, and it's intrinsic non-dimensional unit is the constant ratio of its circumference to its diameter—π. This is not chosen; it is measured from the register.

The basis-radius selection problem is therefore not "which transcendental number should we allow in our integer arithmetic?" It is:

> **Which sphere radius, expressed as a multiple of the substrate's own natural unit, minimizes the total Presburger execution cost of the fractal quine's state-update program?**

Presburger arithmetic governs the *operations*—addition and order only, with multiplication by a constant implemented as repeated addition. The *basis symbol* is determined by the physical substrate and is not subject to Presburger's domain restriction. Presburger minimization then selects among configurations expressible as repeated additions of that basis symbol—which is precisely what Presburger arithmetic permits.

Cost model. The relevant cost is the total execution cost of the state-update program:

$$C(\mathcal{P}) = C_{\text{lookup}} + C_{\text{op}} + C_{\text{reuse}},$$

where:

- C_{lookup} counts distinct symbol retrievals,
- C_{op} counts repeated-addition execution cost,
- C_{reuse} rewards reuse of already-instantiated basis symbols across multiple channels.

The complete state-update cost for a single Soddy sphere in the FTC will be demonstrated to contain three independent channels:

$$T_{\text{sphere}}(r) = 4\pi r^2 + \pi r + r.$$

The optimization problem is:

> Choose the basis radius r—expressed as a Presburger-valid multiple of the substrate's natural unit—minimizing total fractal-quine execution cost by maximizing symbol reuse and minimizing distinct lookup operations during recursive state updates.

Two representative choices illustrate the result:

- **Choice $r = 4$ (four sphere-radii as basis):**

  $$T_{\text{sphere}}(4) = 64\pi + 4\pi + 4 \approx 217.6.$$

  The program must maintain two distinct persistent symbols—the geometric constant π (the substrate's natural unit) and the separate basis radius 4. These are two different programs the machine must instantiate and keep available across every recursive update. Symbol reuse is partial.

- **Choice $r = \pi$ (one sphere-radius as basis):**

  $$T_{\text{sphere}}(\pi) = 4\pi^3 + \pi^2 + \pi \approx 137.036.$$

  Here the basis radius and the substrate's natural geometric unit are the *same persistent symbol*. Every channel in the state-update program reads from the single physical program that a sphere executes to report its own geometry. One distinct symbol class is eliminated from the recursive lookup table entirely.

The reduction is not merely numerical but computational. When $r = \pi$, the fractal quine executes fewer recursive symbol-resolution steps because the sphere radius, rotational arc-length scale, and geometric curvature constant collapse into a single reusable substrate program. This is the *physical* content of the minimization: not that π is a pretty number, but that a sphere packing whose registers are spheres has only one natural word size, and the minimum-cost program uses that word size as its basis rather than introducing a second incommensurable symbol.

> **Axiom P2 (Presburger Minimization Principle):** A MATHICCS-valid self-describing machine selects the basis radius minimizing total recursive execution cost under Presburger operations. For a substrate of no-slip rotating spheres in a sphere packing, the substrate's own natural unit is π—the ratio of circumference to diameter, directly and persistently realizable as a physical operation on the register. The unique basis radius satisfying maximal geometric-symbol reuse across all three independent Soddy state channels is therefore:
>
> $$\boxed{r = \pi}.$$
>
> This identifies the physical word size of the substrate first; Presburger minimization then selects the basis in the usual way.

This principle is analogous to least action, but applied to computational persistence rather than trajectory optimization: under this ontology the universe evolves toward dynamically reusable code minimizing recursive lookup and execution complexity inside the fractal quine.

The choice $r = \pi$ is not an arbitrary or fitted parameter. In the TFOFT ontology the universe consists solely of a dynamic fractal sphere packing; abstract numbers possess no independent ontological status. Every physical sphere can persistently and internally realize only one dimensionless quantity without external reference or imported scale: the ratio of its own circumference to its diameter. This ratio, π, is therefore the unique natural unit of the substrate.

Any other basis radius would require the persistent importation of a scale that cannot be generated or agreed upon by the spheres themselves. Such an external scale would violate the Internal Realization Requirement (IRR) of MATHICCS. Thus $r = \pi$ is the only MATHICCS-compliant choice: it is the unique word size enforced by the physical registers of the FTC.

5.3 The Single-Sphere Register: Three Channels and the Fine-Structure Constant

A single dynamic Soddy sphere is conjectured to be the minimal self-referential object in the FTC. Its complete dynamical state requires three orthogonal and independent pieces of information, each corresponding to one Presburger information channel:

- **Surface channel** T_S: Which point on the sphere's surface is currently active? The cost to uniquely specify any point is proportional to the total surface area:

  $$T_S = 4\pi r^2\big|_{r=\pi} = 4\pi^3 \approx 124.025.$$

  This is the Fundamental Area Metric (FAM).

- **Rotational channel** T_R: What is the phase or orientation of the sphere's angular momentum vector? In 3D, rotations are parameterized by points on the unit 3-sphere S^3 with a 2-to-1 covering. The half-turn symmetry means only one hemisphere need be specified, preventing MATHICCS-invalid gimbal lock and multi-valued functions at the poles. The great-circle arc length of one hemisphere at radius $r = \pi$:

  $$T_R = \pi r\big|_{r=\pi} = \pi^2 \approx 9.870.$$

  This is the Fundamental Phase Metric (FPM).

- **Radial channel** T_D: What is the radial distance of the sphere's center from a reference point? The minimum resolvable step is one sphere radius:

$$T_D = r\big|_{r=\pi} = \pi \approx 3.142.$$

This is the Fundamental Length Metric (FLM).

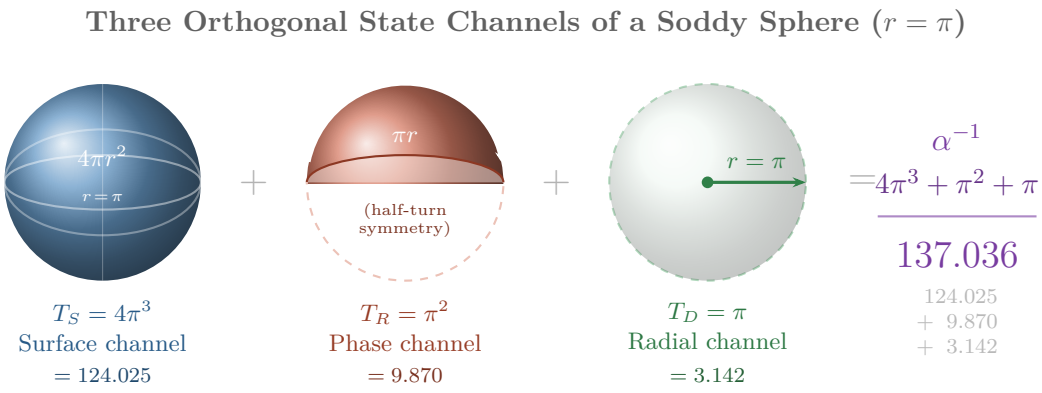

Figure 2: The fine-structure constant α^{-1} as a sum of three orthogonal Presburger information costs for a single Soddy sphere of radius $r = \pi$. **Blue** ($T_S = 4\pi^3$): surface-area channel. **Red** ($T_R = \pi^2$): phase channel (hemisphere only). **Green** ($T_D = \pi$): radial channel. No free parameters; $r = \pi$ is the unique Presburger-minimal radius (Axiom P2).

Register interpretation. The inverse fine-structure value derived here is the full dimensionless Presburger computation cost of one finite Soddy-sphere register update:

$$\begin{aligned} T_{\text{sphere}} &= T_S + T_R + T_D \\ &= 4\pi^3 + \pi^2 + \pi \\ &= 137.0363038\ldots. \end{aligned}$$

The three costs are added because the FTC update is a sequential finite trace: the surface address, rotational phase, and radial displacement channels must each be resolved once in the causal order of a complete update. The cost counts finite causal work performed by the register, channel by channel, under Presburger-valid operations.

Exponential stability requires this finite trace to be recursively clampable. Each layer must complete its finite update before its output is used as input by the next layer. The resulting register depth near 137 is the exponential causal depth of a stable async sphere-register transaction inside the FTC.

The integer register skeleton is 137, while the full geometric single-sphere cost is

$$T_{\text{sphere}} = 137 + \epsilon_\alpha = 137.0363038\ldots.$$

The residual ϵ_α is retained and accounted for later as the fractional correction channel. A stable self-similar register with logarithmic causal depth T_{sphere} spans an exponential state range

$$\mathcal{N}_{\text{sphere}} \sim e^{T_{\text{sphere}}} \approx e^{137}.$$

Thus the derivation of α^{-1} fixes the natural single-sphere exponential register size: 137 is the integer Presburger layer count, ϵ_α is the geometric residual, and e^{137} is the corresponding causal state capacity across recursive fractal layers.

5.3.1 Unique Accepting Alignment and Coupling Probability: α

The single-sphere register derived above gives the full causal update depth

$$T_{\text{sphere}} = 4\pi^3 + \pi^2 + \pi = 137.0363038\ldots.$$

This is the ontology-internal ASSP register value: the normalized causal phase-volume of one complete Soddy-sphere update, preserving the ordered surface channel, the hemisphere-restricted rotational phase channel, and the radial displacement channel simultaneously.

The FTC has no external synchronizing clock. Neighboring ball-registers update asynchronously. A mutual tangent interaction computes when adjacent registers are updated in the required mutual sequence during the complete update trace. An elementary electromagnetic transaction is the successful phase-aligned causal handshake between two adjacent Soddy registers: one register emits or presents a boundary phase defect, and the neighboring register accepts it in the causally ordered phase position compatible with the full single-sphere update.

Lemma: Unique accepting alignment. For a two-ball electromagnetic transaction, the number of accepting alignments is

$$N_{\text{accept}} = 1.$$

A successful adjacent-register handshake must close the surface, rotational-phase, and radial-displacement channels in the same causal order. Any offset in the receiving register breaks the full two-ball transaction. Across the normalized receiving-register phase-volume T_{sphere}, exactly one aligned phase window accepts the incoming boundary phase defect.

The elementary coupling probability is the normalized phase-volume probability for a unique accepting alignment inside a receiving register of causal depth T_{sphere}:

$$P_{\text{align}} = \frac{N_{\text{accept}}}{N_{\text{possible}}} = \frac{1}{T_{\text{sphere}}}.$$

Since the electromagnetic channel is defined in the ontology as adjacent-register phase transfer, the fine-structure constant is the elementary alignment probability:

$$\boxed{\alpha = P_{\text{align}} = \frac{1}{T_{\text{sphere}}} = \frac{1}{4\pi^3 + \pi^2 + \pi}}$$

or equivalently

$$\boxed{\alpha^{-1} = T_{\text{sphere}} = 4\pi^3 + \pi^2 + \pi = 137.0363038\ldots}$$

Thus α^{-1} is the full causal register depth of one complete Soddy-sphere update, while α is the probability that an asynchronous neighboring register lands in the unique accepting alignment required for an elementary electromagnetic transaction. The identification of P_{align} with α is deductive inside the ontology: electromagnetism has already been defined as adjacent-register phase transfer, and α is the elementary probability for such transfer.

Physical interpretation. The inverse fine-structure constant measures the full causal throughput cost for one complete Presburger tick of a single Soddy sphere:

$$\alpha^{-1} = T_{\text{sphere}}.$$

This throughput cost includes surface specification, rotational phase, and radial displacement. An electromagnetic interaction is the adjacent-register phase-transfer transaction between two causally neighboring spheres. Because the transaction has exactly one accepting alignment among T_{sphere} possible internal causal positions, its elementary throughput probability is

$$\alpha = \frac{1}{T_{\text{sphere}}}.$$

The value derived here is the ontology-internal ASSP register value, compared against the CODATA recommended least-squares value of α [27]. Effective low-energy determinations of α may differ between experimental channels because each atom realizes the electromagnetic register through a different evolved local configuration. This distinction is important because the present atom-recoil situation is unresolved: high-precision atom-recoil determinations using cesium and rubidium differ at the several-sigma level. The 2018 cesium measurement gave

$$\alpha_{\text{Cs}}^{-1} = 137.035999046(27),$$

while the 2020 rubidium measurement gave

$$\alpha_{\text{Rb}}^{-1} = 137.035999206(11).$$

The rubidium result was reported as differing by more than five standard deviations from the best cesium-recoil result [28, 29]. No experimental error or systematic correction large enough to remove this discrepancy has been identified in the more than five years since the cesium result and the subsequent rubidium measurement.

Therefore, throughout this paper,

$$\alpha_{\text{ASSP}}^{-1} = 4\pi^3 + \pi^2 + \pi$$

is the predicted ASSP coupling-register depth used for comparison with laboratory determinations.

5.4 The Fractal Quine: Two Balls and the Universal Fundamental Law

The result $T_{\text{sphere}} = 137.036$ is the complete description of a single isolated Soddy sphere. When a second sphere is placed in tangency with the first, the system becomes a self-executing program—the **fractal quine**:

1. The first sphere (star ball) encodes angular momentum state into its surface channel $T_S = 4\pi^3$.

2. Tangency with the second sphere (core ball) provides the unique Möbius-invariant coupling.

3. The angular-and-linear momentum transfer in the higher fractal layer is the photonic mechanism (info ball).

4. The computational cost is paid by injecting momentum into the lower fractal layer (dust balls).

One ball on top of $T_{\text{sphere}} = 137.036$ is a state. Two balls in tangency is a law.

5.5 Two-Ball Computational Overhead and the Laderman 3x3 Split

When two balls form a gyro ball, the FTC promotes a one-register Presburger update into a three-channel Euclidean tangency update. The tangent balls are geared rotational computers. A true two-ball tangency update is therefore a finite geared-rotation computation across the three surface/phase/radial channels.

Fast matrix multiplication supplies the finite compute-count model: a higher-dimensional operation can be performed with fewer multiplication-like steps by paying additional addition-like bookkeeping. Strassen is mentioned only as the historical 2×2 prototype; the FTC uses Laderman's 3×3 multiplication scheme, which reduces the naive 27 multiplication count to 23 multiplication-like operations [30].

In the FTC interpretation, $23/27$ is the geared-rotation compute fraction of a three-channel tangent-ball update, while $4/27$ is the addition-only leakage complement. The rank-23 split is therefore used as the finite rotation-compute split of the gyro-ball boundary:

- Naive 3×3: 27 multiplication-like operations.
- Laderman 3×3: 23 multiplication-like operations.
- Curvature fraction: $23/27 \approx 0.8519$.
- Addition-only leakage fraction: $4/27 \approx 0.1481$.
- Two-ball curvature overhead: $2 \times 23/27 \approx 1.7037$.
- Dual-channel leakage overhead: $2(23/27)^2(4/27) \approx 0.2150$.
- Total two-ball overhead: $\Delta T_{\text{two-ball}} \approx 1.9187$.

Thus the two-ball quine depth is

$$\boxed{T_{\text{two-ball}} = T_{\text{sphere}} + \Delta T_{\text{two-ball}} = 137.0363 + 1.9187 = 138.9550} \tag{1}$$

The first cross-check of the two-ball register scale is the observed electron-to-solar logarithmic hierarchy:

$$\ln(M_\odot/m_e)_{\text{obs}} \approx 138.9357 \text{ [27]},$$

which lies close to the internally derived value $T_{\text{two-ball}} = 138.9550$. The following section does not solve for the mass register from this observed hierarchy. Instead, it derives the 77-layer Star Ball self-encoding register from the rank-23 boundary split and then treats the electron–star hierarchy as a confirmation of the ontology.

6 The Mass Register and the Electron–Star Hierarchy

6.1 Rank-23 Channel Split, Half-Boundary Register, and 77-Layer Encoding

The mass hierarchy is the quine self-encoding layer count of a Star Ball mass register consisting of the full single-sphere state plus one half of the rank-23 curvature boundary needed to define that state relationally. In our universe, the quantized-energy object (Atom) and the flat-rotation-curve object (Galaxy) are identified as fractal-equal objects constructed by their constituents: the electron and the star. The electron-to-solar hierarchy is therefore a cross-check: it tests whether the internal closure lands near the expected astrophysical scale.

6.1.1 The Natural Split from Rank-23 Geometry

The isolated single-ball register is

$$T_{\text{sphere}}^{\text{TFOFT}} = 4\pi^3 + \pi^2 + \pi = 137.0363038.$$

This is the complete FTC state cost of one isolated Soddy sphere. However, a mass hierarchy is not a free-standing isolated sphere. A Star Ball mass register only becomes a physical register when it is relationally defined against a Core Ball boundary. The relevant construction is therefore not the full two-ball transfer register, but the one-register mass channel with a shared relational boundary.

The rank-23 two-ball geometry supplies the raw dual-channel leakage into the Info Ball channel:

$$k_{\text{info}}^{(0),\text{TFOFT}} = 2\left(\frac{23}{27}\right)^2\left(\frac{4}{27}\right).$$

Here 23/27 is the rank-23 curvature fraction relative to the naive 3×3 multiplication count, 4/27 is the addition-only leakage fraction, and the prefactor of 2 counts the two directed boundary legs of the Core–Star transfer. Numerically,

$$k_{\text{info}}^{(0),\text{TFOFT}} = 2\left(\frac{23}{27}\right)^2\left(\frac{4}{27}\right) = 0.2150079.$$

Within the e-clamped two-channel budget, the complementary mass step is therefore

$$k_{\text{mass}}^{\text{TFOFT}} = 2 - k_{\text{info}}^{(0),\text{TFOFT}} = 1.7849921.$$

This value is derived from the rank-23 channel geometry. It is not obtained from $\ln(M_\odot/m_e)_{\text{obs}}$, from Karlsson periodicity, or from any observed mass ratio.

> The raw rank-23 geometry first determines the Info Ball leakage $k_{\text{info}}^{(0),\text{TFOFT}}$. The mass-channel step $k_{\text{mass}}^{\text{TFOFT}}$ is then the complementary e-clamped channel. Observation may later check this value, but it does not define it.

6.1.2 Why 77 Layers: The Half-Boundary Mass Register

The 77-layer count follows from the half-boundary Star Ball mass register and the rank-23 geared-rotation channel split. The Star Ball mass hierarchy is a one-register hierarchy that still requires a relational Core Ball boundary. The mass register therefore sits between the isolated single-ball state and the full two-ball quine transfer.

The lower limit is the isolated sphere:

$$T_{\text{lower}}^{\text{TFOFT}} = T_{\text{sphere}}^{\text{TFOFT}} = 137.0363038.$$

The full two-ball boundary would add a complete rank-23 curvature boundary:

$$T_{\text{upper}}^{\text{TFOFT}} = T_{\text{sphere}}^{\text{TFOFT}} + \left(\frac{23}{27}\right) = 137.8881556.$$

But the Star Ball mass register receives only half of this boundary, because the boundary is shared relationally between the Star Ball and the Core Ball. Thus the mass register is

$$T_{\text{mass}}^{\text{TFOFT}} = T_{\text{sphere}}^{\text{TFOFT}} + \frac{1}{2}\left(\frac{23}{27}\right).$$

Numerically,

$$T_{\text{mass}}^{\text{TFOFT}} = 137.0363038 + 0.4259259 = 137.4622297.$$

The self-encoding layer count is then the mass-register depth divided by the internally derived mass-channel step:

$$S_{\text{mass}}^{\text{TFOFT}} = \frac{T_{\text{mass}}^{\text{TFOFT}}}{k_{\text{mass}}^{\text{TFOFT}}} = \frac{137.4622297}{1.7849921} = 77.00999 \approx \boxed{77}.$$

This is the central mass-hierarchy derivation. The integer 77 is selected by the half-boundary Star Ball mass register and the rank-23 channel split alone. No observed mass ratio is used to solve for $k_{\text{mass}}^{\text{TFOFT}}$ or $S_{\text{mass}}^{\text{TFOFT}}$.

> A single isolated sphere is a state. A full two-ball register is the quine transfer. The mass hierarchy sits between them: it is the Star Ball's own single-sphere state plus one half of the shared rank-23 curvature boundary. That half-boundary closure pins the self-encoding count at $S_{\text{mass}}^{\text{TFOFT}} \approx 77$.

6.1.3 Interval View of the Mass Register

The half-boundary construction places the mass register between the isolated single-ball limit and the full two-ball boundary limit:

$$T_{\text{sphere}}^{\text{TFOFT}} < T_{\text{mass}}^{\text{TFOFT}} < T_{\text{sphere}}^{\text{TFOFT}} + \frac{23}{27}.$$

Equivalently, in layer units,

$$\frac{T_{\text{sphere}}^{\text{TFOFT}}}{k_{\text{mass}}^{\text{TFOFT}}} = 76.7714,$$

$$\frac{T_{\text{mass}}^{\text{TFOFT}}}{k_{\text{mass}}^{\text{TFOFT}}} = 77.0100,$$

$$\frac{T_{\text{sphere}}^{\text{TFOFT}} + \frac{23}{27}}{k_{\text{mass}}^{\text{TFOFT}}} = 77.2486.$$

Thus 77 is not selected by the lower isolated-sphere limit or by the upper full two-ball transfer. It is selected by the half-boundary mass register.

6.1.4 Observed Electron-to-Solar Hierarchy

The observed electron-to-solar logarithmic hierarchy is

$$N_{\text{mass}}^{\text{obs}} = \ln(M_\odot/m_e)_{\text{obs}} \approx 138.936.$$

Using the integer closure $S_{\text{mass}}^{\text{TFOFT}} \approx 77$, the corresponding observed effective step is

$$k_{\text{mass}}^{\text{obs}} = \frac{N_{\text{mass}}^{\text{obs}}}{77} \approx 1.80436.$$

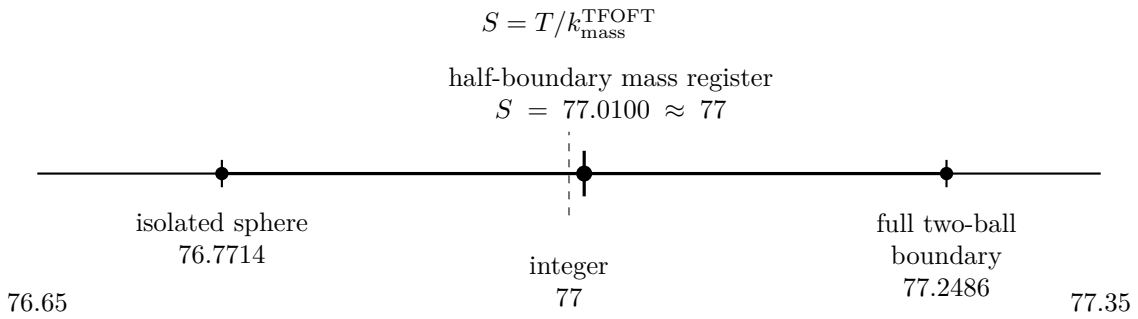

Figure 3: Mass-register interval in layer units. The half-boundary Star Ball mass register gives $S_{\mathrm{mass}}^{\mathrm{TFOFT}} = 77.0100 \approx 77$, between the isolated single-sphere limit and the full two-ball boundary.

The TFOFT mass-channel step is

$$k_{\mathrm{mass}}^{\mathrm{TFOFT}} = 1.7849921,$$

giving

$$\frac{k_{\mathrm{mass}}^{\mathrm{obs}} - k_{\mathrm{mass}}^{\mathrm{TFOFT}}}{k_{\mathrm{mass}}^{\mathrm{TFOFT}}} \approx 1.1\%.$$

This offset is comparable in role to the local virial and density corrections appearing in the G and $\alpha(Z)$ sections.

6.1.5 The 137 − 77 = 60 Residual: He and Fe as Fractal Garbage Collectors

The nearest integer to the single-sphere register depth minus the derived integer mass closure leaves the residual

$$\lfloor \alpha_{\mathrm{TFOFT}}^{-1} \rfloor - S_{\mathrm{mass}}^{\mathrm{TFOFT}} = 137 - 77 = \boxed{60}.$$

We conjecture that this residual encodes the *fractal register garbage collector*: the computational cost of closing the fractal circuit and recycling the momentum debt incurred by mass-channel self-encoding. Persistent computation requires a mechanism to restart fusion processes after a star has exhausted its fuel. The residual Soddy core budget is conjectured to encode the primary fusion endpoints:

- **Helium-4** ($A = 4$): The tetrahedral Soddy-closed shell at four nucleons is conjectured to be the most stable arrangement of simple nucleons in the ASSP. Stability would arise because the external virtual Soddy density exceeds the internal virtual Soddy density, creating a net inward restoring force at every face of the tetrahedron.
- **Iron-56** ($A = 56$): The maximum nucleus for which synthesis still releases energy. Beyond $A = 56$, outer Soddy cores are conjectured to accumulate real curvature faster than inner cores can balance them, and binding energy per nucleon decreases monotonically.

Together,

$$4 + 56 = 60 = \lfloor \alpha_{\mathrm{TFOFT}}^{-1} \rfloor - S_{\mathrm{mass}}^{\mathrm{TFOFT}}.$$

The two dominant nuclear fusion endpoints—helium and iron—are conjectured to be the Soddy-closed garbage-collector states encoded into the arithmetic of fractal self-description: the light and heavy bookends of the 60-unit momentum debt separating the single-sphere register depth from the mass self-encoding layer count.

6.2 Electron and Proton Mass from Recursive Soddy Curvature

The electron rest mass m_e and proton mass m_p emerge from the recursive curvature dynamics of the Apollonian–Soddy sphere packing starting with the fundamental radius $r = \pi$.

Numerical Soddy recursion with frontier pruning (retaining the 20 highest-curvature spheres) produces the following evolution of the deepest registers:

Generation	max $\ln k$	luminous-weighted ($\times 23/27$)
38	81.8579	69.7308
38.5 (interpolated)	**82.9509**	**70.6602**
39	84.0439	71.5929
77	167.1095	142.3525

The factor $23/27 \approx 0.85185185$ is the luminous (mass-bearing) channel fraction. It corresponds to the Laderman rank-23 heavy, curvature-intensive portion of the two-ball gyro-ball interaction that builds persistent inertial registers. The complementary $4/27$ channel is the low-cost Info Ball transfer.

At half-depth (Gen 38.5), the luminous-weighted deepest curvature is 70.6602. Doubling for the full cycle gives 141.3204, close to the internal two-ball quine depth $T_{\text{two-ball}} \approx 138.955$.

The Star Ball mass register sits at the natural *half-boundary* position:

$$T_{\text{mass}} = 4\pi^3 + \pi^2 + \pi + \tfrac{1}{2}\left(\tfrac{23}{27}\right) = 137.4622297\ldots$$

A stable Core Ball (proton) is manufactured as a Soddy composite. The ratio $m_p/m_e \approx 1836.15$ satisfies

$$1836.15/77 \approx 23.846.$$

This lies near the rank-23 Laderman curvature overhead, with a residual of approximately 3.7% relative to 23. It is therefore treated as an approximate structural check on the claim that core manufacturing corresponds to one full mass-register cycle modulated by the dominant Soddy/Laderman factor, rather than as an exact derivation.

Quine Closure Condition. The recursive Soddy geometry, weighted by the luminous fraction 23/27, must internally reproduce the register depths of the fractal quine. This determines the emergent conversion factor σ (geometric register cost $\to$ physical mass/energy) and fixes the base Star Ball mass m_e such that

$$\ln\left(\frac{M_\odot}{m_e}\right)_{\text{TFOFT}} \approx T_{\text{two-ball}} \approx 138.955$$

holds as an internal relation of the ASSP architecture.

Thus the dimensionless electron–star hierarchy and proton/electron structural ratio are derived from the recursive Soddy curvature structure under Presburger cost minimization with initial radius $r = \pi$. No external laboratory mass measurement is required as a primary input for the ratios and hierarchies. All other dimensionless constants of the theory (α, hierarchy depths, channel fractions, and register ratios) follow directly from this self-describing fractal quine.

On absolute scale in laboratory units. Because the ontology is strictly fractal, each scale has its own "electron" (Star Ball). The here-scale electron mass in laboratory units (0.511 MeV) requires one overall scale anchor fixing the here-layer unit convention. Once this anchor is fixed, absolute masses in kg or MeV become derived predictions. The dimensionless ratios and register structure remain fully internal and zero-parameter.

7 Atomic Clock-Locking: Hydrogen, Kepler Scaling, and the Rydberg Ladder

7.1 Local c as Diameter Transfer and Finite Information Update

The follow-up dynamics paper derives the coarse GR/QM limits from the same ball dynamics. The basis radius $r = \pi$ is the internally self-known word size of the spherical register: the dimensionless geometric program every sphere can realize without external reference. Actual balls possess physical radii R, and those radii set the layer-dependent transfer scale.

In the FTC ontology, c is the diameter-transfer rate of the spherical register. Energy transfer across a diameter is instantaneous in the null-channel sense, matching the photon proper-time relation $\Delta\tau = 0$. The information that the transfer occurred propagates through finite register updates, because neighboring balls must resolve rotational phase through their own finite-radius causal clocks.

A bound Star Ball locks to the Core Ball at the fractional rate fixed by the single-sphere electromagnetic register:

$$v_{\text{lock}} = \alpha c.$$

Thus the lock velocity is a relation between balls: the Star Ball runs at one α-fraction of the Core-defined diameter-transfer scale.

7.2 Atom Base Energy: Deriving the Hydrogen Binding Energy

The hydrogen atom is the low-scale Gyro Ball. The ball mapping is

$$\text{Core Ball} \leftrightarrow \text{proton/nucleus}, \qquad \text{Star Ball} \leftrightarrow \text{electron},$$

$$\text{Gyro Ball} \leftrightarrow \text{closed Star–Core round trip}, \qquad \text{Info Ball} \leftrightarrow \text{photon in transport}.$$

Binding appears when the Star Ball and Core Ball complete one stable Gyro-Ball loop. The completed loop stores the kinetic closure cost of the Star Ball at the lock speed $v_{\text{lock}} = \alpha c$:

$$E_{\text{atom}} = \frac{1}{2} m_{\text{star}} v_{\text{lock}}^2 = \frac{\alpha^2 m_{\text{star}} c^2}{2}. \tag{2}$$

At the atomic layer the Star Ball is the electron, so $m_{\text{star}} = m_e$, giving

$$E_H = \frac{\alpha^2 m_e c^2}{2} \approx 13.606 \text{ eV}.$$

This is the ball-register origin of the hydrogen binding energy: local spherical radius/update scale gives c, the single-sphere register gives α, and the completed Star–Core Gyro loop gives the stored binding energy.

7.3 Kepler's Third Law as the Gyro Ball Clock-Locking Equation

The Gyro Ball interpretation applies not only to the atomic hydrogen binding channel but also to the macroscopic orbital clock of a star around a core. Newton's form of Kepler's third law is [31]

$$T^2 = \frac{4\pi^2}{GM} a^3,$$

where T is the orbital period, a is the semi-major axis, and GM is the gravitational parameter of the core.

Multiplying by the Presburger basis radius $r = \pi$ gives

$$\pi T^2 = 4\pi^3 \frac{a^3}{GM}.$$

Thus Kepler's third law can be written in the ASSP form

$$\boxed{\pi T^2 = 4\pi^3 \mathcal{K}_a} \qquad \text{where} \qquad \mathcal{K}_a = \frac{a^3}{GM}.$$

This is not merely a rescaling of the period. In the FTC interpretation, πT^2 is the orbital clock expressed through the fundamental-radius channel $r = \pi$. The factor $4\pi^3$ is the universal Soddy surface register cost already appearing in the single-sphere state budget,

$$T_S = 4\pi^3.$$

The remaining factor,

$$\mathcal{K}_a = \frac{a^3}{GM},$$

is the local Kepler divider.

The semi-major axis a defines the radius of the virtual Soddy sphere enclosing the Gyro Ball orbit via the tangency chain connecting the Star Ball to the Core Ball boundary. Under this interpretation a^3 is the radial-volume information register of that virtual sphere. The factor GM is the core curvature-throughput rate: the processing strength of the Core Ball boundary. Hence $\mathcal{K}_a$ is the virtual Soddy sphere's information load per unit core throughput.

Equivalently, $\mathcal{K}_a$ is the local clock-divider of the orbital system. A larger virtual Soddy sphere contains more orbital information volume and therefore requires a slower locked output clock. A larger core throughput GM processes that volume faster and shortens the orbital period.

In this form, Kepler's law functions analogously to phase-locked loop in a physical FPGA. The universal reference is the fundamental-radius channel $r = \pi$. The local oscillator is the visible Gyro Ball orbital period T. The divider is $\mathcal{K}_a = a^3/GM$. A stable orbit is the locked output clock of the system:

$$\text{radius-channel reference} \quad \longrightarrow \quad \text{local Kepler divider} \quad \longrightarrow \quad \text{stable Gyro Ball clock.}$$

Under this ontology, ordinary orbital time is not fundamental in the FTC. It is the relative time generated when the luminous addition-only transfer channel locks to the ASSP radius/surface register. The visible star orbit is the $\sim 4/27$ addition-efficient channel of the two-ball update, while the complementary $\sim 23/27$ Laderman rank-23 overhead is paid into lower-layer substrate and appears as dark computational mass rather than luminous Keplerian motion.

The connection to the fine-structure derivation is direct. The full single-sphere register is

$$T_{\text{sphere}} = 4\pi^3 + \pi^2 + \pi,$$

where $4\pi^3$ is the dominant surface channel. Kepler's third law isolates this same leading surface channel and turns it into the observable relative clock of a macroscopic Gyro Ball:

$$\pi T^2 = 4\pi^3 \mathcal{K}_a.$$

Therefore α^{-1} gives the full async single-sphere register depth, while Kepler's law gives the radius-locked relative clock by which visible Gyro Balls execute their luminous orbital updates.

7.4 Rydberg Scaling from Virtual-Core Clock Quantization

The FTC does not quantize free orbits. A Star Ball may evolve continuously under the Gyro Ball Kepler clock until the tangency chain reaches a Core–Star boundary. Quantization enters only at the boundary-transfer event, where the angular-momentum component of the update is transfered into an Info Ball channel.

The reason the transfer is quantized is that the Core Ball is not a continuum object. In the FTC ontology, a Core Ball is a semi-virtual boundary-throughput object defined by finite ASSP support around a stable tangency center. That support may be supplied by luminous Star Balls, by Dust Balls and lower-layer substrate, by sub-stellar objects, or by any combination of these channels. A galaxy core with many visible stars is one realization; a dark-matter-dominated or star-free core is another. Such a "naked" Core Ball is still physically real in the FTC sense if its boundary condition is maintained by lower-layer tangency pressure and substrate flow.

At the galactic scale, the luminous Star Ball population contributes to the center-of-mass and visible Kepler clock of the Core Ball, but it need not supply the whole definition. The remaining support may be carried by Dust Balls, sub-stellar objects, and lower-layer substrate. At the atomic scale, the proton/nuclear core is the corresponding lower-scale Core Ball, while the electron is the Star Ball. The observed atomic clock is therefore a fractal Kepler clock: ordinary atomic time is the lower-scale analogue of the macroscopic Gyro Ball orbital clock.

From the radius-channel Kepler relation derived above,

$$\pi T^2 = 4\pi^3 \mathcal{K}_a,$$

the quantity πT^2 is the orbital clock expressed through the fundamental-radius channel $r = \pi$. It is the internal ASSP clock-cost of the virtual Core–Star system. Photon frequency is the inverse clock output, so boundary-transfer energy is controlled by inverse clock-area:

$$E \propto \frac{1}{T^2}.$$

Let n denote the integer virtual-core clock layer defined by the finite ASSP support of the Core Ball. This support need not be luminous. It may be provided by Star Balls, Dust Balls, sub-stellar registers, lower-layer gas, or any mixture of these components. Thus n is not a Bohr orbit quantum number and not merely a count of visible orbiting bodies. It is the number of completed Kepler-supported or substrate-supported clock layers available to the virtual Core Ball at the boundary-transfer event.

Because the target Info Ball channel must be written into a completed ASSP ball layer, only integer n is allowed. There is no half-layer write target. The n-th virtual-core clock layer satisfies

$$T_n = nT_1.$$

Therefore its inverse clock-area is

$$\frac{1}{T_n^2} = \frac{1}{n^2 T_1^2}.$$

The base Core–Star boundary-transfer energy is the Gyro Ball energy

$$E_{\text{atom}} = \frac{\alpha^2 m_{\text{star}} c^2}{2}.$$

Thus the allowed boundary energies are

$$\boxed{E_n = -\frac{E_{\text{atom}}}{n^2}.}$$

For hydrogen, $m_{\text{star}} = m_e$, so

$$E_{\text{atom}} = 13.606\,\text{eV},$$

and

$$E_n = -\frac{13.606\,\text{eV}}{n^2}.$$

A photon is emitted when the virtual Core Ball relocks from one completed clock layer to another:

$$E_\gamma = E_{\text{atom}} \left(\frac{1}{n_f^2} - \frac{1}{n_i^2} \right).$$

Thus the Rydberg $1/n^2$ law is not imposed by quantized free orbits. It follows from the inverse-square clock-area of a finite virtual Core Ball: the Kepler relation defines ASSP internal time, and discrete ball-layer support quantizes the clock layers at the Core–Star boundary. The emitted Info Ball carries the angular-momentum part of the relocking event, while the complementary linear-momentum cost remains behind in lower-layer substrate.

7.4.1 Finite Lyman and Rydberg Ceilings

The two-ball quine depth provides two distinct spectral ceilings. The direct basis-channel transfer, corresponding to the Lyman series $n_i \to 1$, is limited by the two-ball boundary depth itself:

$$n_{\max}^{\text{Lyman}} \sim T_{\text{two-ball}} \approx 139.$$

This is the maximum direct Core–Star boundary relocking depth into the basis hydrogen register.

At this depth, the last direct Lyman transfer lies only

$$\frac{13.606\,\text{eV}}{139^2} \approx 7.04 \times 10^{-4}\,\text{eV}$$

below the conventional infinite-n Lyman limit. Adjacent terminal Lyman-line spacing near this depth is approximately

$$\Delta E \sim \frac{2(13.606\,\text{eV})}{139^3} \approx 1.0 \times 10^{-5}\,\text{eV}.$$

Therefore ordinary spectroscopy would see the finite basis-channel ceiling as an effective continuum edge unless the experiment resolves sub-meV structure near the Lyman limit and controls broadening effects.

Rydberg-like configurations are different. They are not direct relockings into the basis state but composite excited tangency-chain configurations inside the rotational channel. Since the rotational channel has quadratic subdivision, the effective composite hydrogen address-space ceiling scales as

$$n_{\max}^{\text{H}} \sim (T_{\text{two-ball}})^2 \approx 139^2 \approx 1.93 \times 10^4.$$

This number should be interpreted as the number of principal hydrogen register addresses, not the number of pairwise emitted lines. Spectral lines are relockings between finite register addresses. Therefore the full transition graph can contain many pairwise differences, but it remains finite because the underlying hydrogen register has only finitely many allowed address states.

Thus the FTC does not predict the absence of high-n Rydberg states above $n \approx 139$. It predicts that the direct Lyman basis-channel transfer saturates near $n \approx 139$, while composite Rydberg states can extend to the quadratic rotational-channel ceiling.

7.5 Nuclear Binding Energy: The Soddy Fractal Nucleon Stack

7.5.1 The Soddy Core Concept

In any Apollonian-Soddy sphere packing, a cluster of n mutually tangent equal spheres admits:

- An **inner Soddy sphere** fitting exactly in the central interstice (positive curvature, bending inward).

- A **virtual outer Soddy sphere** circumscribing the cluster (negative curvature, bending outward).

Both are determined uniquely by the Descartes–Soddy relation [14, 11, 12].

7.5.2 Four Nucleons: The Tetrahedral Peak

The minimal 3D Soddy-balanced configuration is four mutually tangent equal spheres arranged in a regular tetrahedron. For this configuration, both inner and outer Soddy cores remain virtual, acting as geometric pressure-balance constraints. The tetrahedral four-nucleon cluster is conjectured to experience maximum restoring force and minimal dislocatability—consistent with ^{4}He having the highest binding energy per nucleon ($\approx$ 7.07 MeV/nucleon) among light nuclei.

7.5.3 Five Nucleons: First Inner Soddy Core Manifests

Adding a fifth nucleon breaks the tetrahedral balance. The inner Soddy core becomes a resolvable packing site while the outer remains virtual. The asymmetric balance is conjectured to reduce binding energy per nucleon—consistent with the absence of stable $A = 5$ nuclei in nature.

7.5.4 The Iron Peak (Conjecture)

Iron (^{56}Fe) is conjectured to sit at the global binding energy maximum ($\approx$ 8.79 MeV/nucleon) because it is the first Soddy iteration at which both inner and outer Soddy cores are simultaneously real and balanced at the same iteration depth. Beyond $A = 56$, outer Soddy cores are conjectured to accumulate real curvature faster than inner cores can balance them.

7.6 Pauli Exclusion from Soddy Uniqueness (Conjecture)

Given any interstice in a locally finite Apollonian-Soddy sphere packing, the corresponding tangent sphere is fixed by the Descartes–Soddy relation [14, 11, 12]. We conjecture that this geometric uniqueness is the physical origin of the Pauli exclusion principle.

8 The Ball Ontology: Fundamental Objects of the FTC

We use three scale prefixes throughout the ontology. **Atom** denotes the atomic scale. **Here** denotes the galactic/stellar scale. **Wish** denotes the scale above the galactic, where our galaxy plays the role that an atom plays at our scale.

The FTC basis begins with four primary objects. A **Star Ball** is the orbiting angular-momentum register: at the atomic scale it is the electron, and at the here-scale it is the star. A **Core Ball** is the receiving and emitting boundary register: at the atomic scale it is the proton/nucleus, and at the here-scale it is the galactic core. A Star Ball bound to a Core Ball forms a **Gyro Ball**, the closed Star–Core circuit: atom at the lower scale, spiral galaxy at the here-scale. An **Info Ball** is the photon/macrophoton in transport, the cross-scale angular-momentum carrier moving between source and receiver.

When the transport channel Info Ball lands at a Core boundary, the receiving side can recombine in two main ways. A lower-power coherent reconstruction produces a **Spit Ball**, identified astrophysically with black-hole jet or AGN jet behavior. A higher-power reconstruction produces a **Fast Ball**, identified astrophysically with quasars. Thus the table distinguishes the transport carrier from the receiving-side reconstruction: Info Ball is the photon/macrophoton in transport; Spit Ball and Fast Ball are post-injection recombination channels.

The remaining ball types name the supporting FTC bookkeeping objects. **Dust Balls** are the lower-scale linear-momentum cost paid by the transfer, appearing here-scale as dark-matter halo substrate, comprised of the lower fractal scale interstellar medium (e.g, smaller scale hydrogen gas). **Pipe Balls** are elongated lower-layer tangency chains that behave as magnetic-field-line or filament channels. **Wake Balls** are the disturbance patterns generated by moving registers. **Roll, Spin, Kick, and Data Balls** describe the conservation bookkeeping of angular, linear, and internal state. These names are not independent new particles; they are the FTC vocabulary for the same recursive ASSP register dynamics viewed by role.

Table 2: TFOFT Ball Ontology: the conjectured self-describing objects of the FTC. Cross-scale correspondences are proposed exact fractal-scale equivalences governed by the same Presburger equations with only scale parameters r and mass M varied.

Ball Type	**Role in FTC**	**Atomic Equiv.**	**Astro. Equiv.**
Star Ball	Orbiting angular-momentum register; the stable bound unit around a Core Ball.	Electron	Star
Core Ball	Receiving and emitting boundary register; equator converts incoming angular momentum into outgoing lower-scale linear-momentum cost, while poles receive non-local Info-Ball transport.	Proton / Nucleus	Galactic core
Gyro Ball	Star Ball bound to Core Ball; the closed Star–Core circuit for storage and transfer of angular and linear momentum.	Hydrogen atom	Spiral galaxy
Roll Ball	Conservation bookkeeping object; comprised of Spin Ball, Kick Ball, and Data Ball components.	Lower-scale force bleed channels	Here-scale gravity and EM
Spin Ball	Angular momentum carrier; rotational state component of Roll Ball.	Inertia	Inertia
Kick Ball	Linear momentum carrier; translational state component of Roll Ball.	Motion	Motion
Data Ball	Interior information state; ball state plus embedded data; chaotic lower-layer register beneath the primary sphere.	Interior atomic state	Interior stellar state
Wake Ball	Fluid-like disturbance pattern generated by moving Roll Balls; propagates through the Soddy packing.	Quantum wave function	EM and gravitational waves

Continued on next page

Ball Type	Role in FTC	Atomic Equiv.	Astro. Equiv.
Info Ball	Photon/macrophoton in transport: cross-scale angular-momentum information carried between source and receiver. Its transport is inferred from the receiving-side reconstruction state.	Photon in transport	Macrophoton in transport
Spit Ball	Lower-power receiving-side recombination from an Info-Ball transport channel at a Core boundary; astrophysically expressed as coherent jet behavior.	Virtual particles; weak-force-like emission	Black-hole / AGN jet
Fast Ball	Higher-power receiving-side recombination from an Info-Ball transport channel at a Core boundary; astrophysically observed as post-transport anti-core/anti-proton-like states.	Gamma-ray reconstruction	Quasar / anti-core candidate
Dust Ball	Linear momentum computational cost exhausted to scale $A-1$ as lower-scale gyro-balls and constituents.	Electron cloud	Dark matter halos
Null Core	Condensation of scattered lower-scale layers; regions of minimal Soddy packing density.	Galactic void centers	CMB cold spot
Code Ball	Self-referential binding component enabling directed, coherent exchange at core boundaries.	Neutrinos	Life; planets; directed stellar processes
Pipe Ball	Elongated Soddy tangency chain in lower fractal layer, oriented along angular momentum gradient.	Magnetic Field Lines	Cosmic web filament
Jolt Ball	Transient energy redistribution events at the scales between fractal layers.	Atomic decay	Local entropy spikes
Edge Ball	Variable boundary where the dominant force regime changes. On Earth this transition is expected in the approximate 0.1–2 mm range.	Planck-length analogue	0.1–2 mm wish-scale analogue

8.1 Pipe Balls

A **Pipe Ball** is an elongated, quasi-one-dimensional chain of Soddy tangencies in the lower fractal layer, oriented along the gradient of the here-scale angular momentum field. It acts as the fractal-scale analogue of a magnetic field line: a low-density highway of lower-scale hydrogen substrate. In TFOFT, galactic-scale magnetic field lines are physical Pipe Balls tracing the angular-momentum gradient of the local ASSP. The inter-galactic filaments of the cosmic web are their here-scale manifestation at the wish-scale.

8.2 Charge, Direction, and Neutrality in the Particle Dictionary

Charge records the direction of causal energy flow in the FTC:

$$- \leftrightarrow \text{emission/source/outward Star Ball channel,}$$

$$+ \leftrightarrow \text{absorption/sink/inward Core Ball channel,}$$

$$0 \leftrightarrow \text{neutral reservoir, closed loop, balanced composite, or neither-channel body.}$$

Thus the electron is the basic emitting Star Ball channel, while the proton is the basic absorbing Core Ball channel. Neutral objects split into two cases. Some neutral channels are neither-side reservoirs, such as planets, substellar bodies, dust, and neutrino Code Balls. Other neutral channels are balanced composites or closed loops, such as neutron-like reservoirs, neutral weak handshakes, or neutral boundary pulses.

8.3 Code Balls: Neutrino Flavor Channels as Sub-Stellar Lifecycle Stages

The three neutrino flavor channels are compared with the passive substellar ladder using the same electron–star scaling rule:

$$\frac{m_e}{m_\nu} \leftrightarrow \frac{M_\odot}{M_{\text{object}}},$$

so that

$$M_{\text{object}} = M_\odot \frac{m_\nu}{m_e}.$$

Using $m_e = 510998.95069\,\text{eV}$, a neutrino-channel mass m_ν maps to an astronomical object whose mass is the same fraction of the Sun as m_ν is of the electron.

The direct flavor-channel laboratory ceilings are

$$m_{\nu_e} < 0.45\,\text{eV},$$

from the KATRIN tritium endpoint result [32],

$$m_{\nu_\mu} < 0.19\,\text{MeV},$$

from direct pion-decay kinematic limits summarized by the Particle Data Group [33], and

$$m_{\nu_\tau} < 18.2\,\text{MeV},$$

from the ALEPH tau-neutrino endpoint analysis [34]. These laboratory numbers are used as flavor-channel ceilings; the active mass eigenstates need not saturate them.

Representative substellar masses map to the following neutral-channel values:

$$\text{Mercury}: \quad 0.0553 M_\oplus \Rightarrow m_\nu \approx 0.085\,\text{eV},$$

$$\text{Mars}: \quad 0.107 M_\oplus \Rightarrow m_\nu \approx 0.164\,\text{eV},$$

$$\text{Neptune}: \quad 17.1 M_\oplus \Rightarrow m_\nu \approx 26.3\,\text{eV},$$

$$\text{Jupiter}: \quad 317.8 M_\oplus \Rightarrow m_\nu \approx 488\,\text{eV},$$

$$13 M_J: \quad m_\nu \approx 6.34\,\text{keV},$$

$$75 M_J: \quad m_\nu \approx 36.6\,\text{keV}.$$

The planetary values use standard Solar-System mass ratios [35]. The brown-dwarf comparison uses the usual deuterium-burning scale near $13 M_J$ and the hydrogen-burning transition near $75 M_J$ [36].

The resulting FTC channel alignment is

$$\nu_e \leftrightarrow \text{rocky/sub-Earth Code Ball},$$

$$\nu_\mu \leftrightarrow \text{ice/gas giant Code Ball},$$

$$\nu_\tau \leftrightarrow \text{brown dwarf and heavier neutral Code Ball}.$$

No fourth light neutrino is expected because no fourth Soddy-stable passive substellar regime exists between the brown-dwarf channel and the active Star Ball regime [37]. The absence of a measured nonzero lower floor for the lightest neutrino channel mirrors the absence of a sharp lower floor in the substellar hierarchy: below the stellar threshold, the FTC ladder descends through brown dwarfs, gas giants, ice giants, rocky bodies, moons, dwarf planets, asteroids, spacecraft, dust, and lower-layer substrate.

8.4 Standard Model Channels in the TFOFT Dictionary

TFOFT assigns astronomical analogues to physically realized channels: emitters, absorbers, neutral code reservoirs, and boundary-transfer modes. Confined quark labels are treated as Standard Model coordinates for internal Core response. The Core Ball is an irreducible absorbing register at the atomic/galactic layer and has no same-layer decomposition into smaller observable cores.

Table 3: Standard Model channel dictionary under the FTC ontology.

SM item	**Charge**	**FTC status**	**Astronomical analogue**
e^-	-1	Elementary emission channel	Star Ball / Sun-like emitter
e^+	$+1$	Reversed electron channel	Positron / stellar sink counterpart
μ^-	-1	Overmassive emission channel, $m_\mu/m_e \approx 206.77$	Very massive blue/WNh Star Ball
τ^-	-1	Cluster-scale emission channel, $m_\tau/m_e \approx 3477.23$	Compact proto-cluster / cluster-core emitter
p^+	$+1$	Irreducible Core Ball absorber	Galactic core / atomic core
$\bar{p}$	-1	Reversed Core Ball channel	Quasar / anti-core candidate
n^0	0	Neutralized Core Ball reservoir	Balanced core store
γ	0	Info Ball transfer channel	Photon / macrophoton transport
ν_e	0	Neutral Code Ball channel	Rocky/sub-Earth channel
ν_μ	0	Neutral Code Ball channel	Ice/gas-giant channel
ν_τ	0	Neutral Code Ball channel	Brown-dwarf channel

Continued on next page

SM item	Charge	FTC status	Astronomical analogue
W^-	-1	Weak emission-side boundary transition; lower-scale EM bleed	Outward decay boundary
W^+	$+1$	Weak absorption-side boundary transition; lower-scale EM bleed	Inward capture boundary
Z^0	0	Balanced weak boundary transition	Neutral weak handshake
H^0	0	Mass-register clamping excitation	Neutral mass-clamp mode
Quarks	fractional	Standard Model internal Core-response labels	No independent astronomical object
Gluons	color	Standard Model confinement bookkeeping; lower-scale gravity-binding channel	No independent separable object

8.5 Decay Hints for the Charge-Direction Dictionary

The Standard Model decay channels provide useful sign-flow hints for the FTC dictionary. Neutron beta decay,

$$n^0 \to p^+ + e^- + \bar{\nu}_e,$$

reads as a neutral Core reservoir splitting into an absorbing Core channel, an emitting Star channel, and an escaping neutral Code channel.

Muon decay,

$$\mu^- \to e^- + \bar{\nu}_e + \nu_\mu,$$

reads as an overmassive emitting channel relaxing into the ordinary emitting channel plus neutral Code channels. Tau decays similarly express a cluster-scale emitting channel relaxing into lighter emitters, neutral Code channels, and composite Core fragments.

8.6 Wave-Particle Duality as Fractal Pilot-Wave Dynamics (Conjecture)

A Star Ball traversing the region near two adjacent Soddy interstices generates a **Wake Ball**: a fluid-like angular-momentum disturbance propagating through the ASSP fractal substrate. The interference pattern arises because the Wake Ball explores both interstice paths simultaneously.

9 Fine-Structure Constant: Bare Register, Recoil Corrections, and Predictions

9.1 Electromagnetism as Local Boundary Realization

In TFOFT, the fine-structure constant is not a universal abstract number inserted into a Lagrangian. It is the local boundary realization of the lower fractal scale. Thus α is expected to be extremely stable within a given register environment, but not absolutely universal across distinct atomic, nuclear, and chiral boundary realizations.

This differs sharply from the standard QED ontology, in which α is a universal coupling and atomic recoil experiments are merely different routes to measuring the same constant.

In TFOFT, the measured value is instead

$$\alpha_X^{-1} = \alpha_{\text{bare}}^{-1} + \text{boundary realization} + \text{packing deformation}. \tag{3}$$

The Rb/Cs/Yb recoil pattern is therefore not interpreted as experimental scatter around a universal constant, but as the first visible evidence of species-dependent boundary realization.

The proposed model predicts:

$$\alpha_X^{-1} = \alpha_{\text{reg}}^{-1} + C_0^{\text{theory}} + k \ln A + \lambda \Phi_{\text{bind}}(A, Z). \tag{4}$$

If future recoil measurements of Yb, Sr, Ca, or isotope series fail to show this pattern, the TFOFT recoil model is falsified. If they do show this pattern, then the standard interpretation of α as a single universal input parameter is falsified.

9.2 Bare Register Depth Versus Physical Fine-Structure Coupling

A central correction to the TFOFT interpretation is that the quantity

$$\alpha_{\text{reg}}^{-1} = 4\pi^3 + \pi^2 + \pi = 137.036303775878\ldots \tag{5}$$

must not be identified directly with the laboratory fine-structure constant. Instead, this value represents the bare ASSP/Soddy/Presburger register depth: the integer-plus-residual coupling depth before the first physical dynamical object has formed.

The physical coupling is not realized by an isolated mathematical sphere. It is realized only after the first star–core gyroball appears. Thus the observed electromagnetic coupling is a boundary-realized quantity, not the bare register itself.

Let

$$r = \alpha_{\text{reg}}^{-1} - 137. \tag{6}$$

The integer floor 137 is the coarse register count, while r is the fractional residual that must be dynamically discharged by the first physical gyroball.

The first physical object is a two-ball star–core object rather than an isolated single sphere:

$$\text{gyroball} = \text{star} + \text{core}. \tag{7}$$

Therefore even hydrogen is not equal to the bare register value. Hydrogen already contains a two-ball realization correction.

We define the theoretical hydrogen/gyroball correction

$$C_0^{\text{theory}} = -\frac{\alpha_{\text{reg}}^{-1} - 137}{137} \cdot \frac{27}{23 + \phi^{-1}}, \tag{8}$$

where

$$\phi = \frac{1 + \sqrt{5}}{2}. \tag{9}$$

Numerically,

$$C_0^{\text{theory}} = -0.000302936254\ldots \tag{10}$$

and hence the physical hydrogen baseline becomes

$$\alpha_H^{-1} = \alpha_{\text{reg}}^{-1} + C_0^{\text{theory}} = 137.036000839624\ldots. \tag{11}$$

The factor 23/27 is interpreted as the gyroball's dynamical self-encoding efficiency. It appears in the denominator because the available register capacity is reduced by the shared-boundary efficiency, so the same residual is distributed across fewer effective physical registers. The ϕ^{-1} term is the first golden-ratio correction from the self-similar fractal packing geometry. Thus the bare register is not the physical fine-structure constant. The physical constant is the first realized gyroball projection of the bare register.

9.3 Binding-Energy Curve as a Higher-Order Soddy Packing Correction

The minimal model

$$\alpha_X^{-1} = \alpha_{\text{reg}}^{-1} + C_0^{\text{theory}} + k \ln A \tag{12}$$

captures the dominant nucleon-register depth. However, the nuclear binding energy curve should appear as a higher-order local packing deformation.

We therefore write the next-order model as

$$\alpha_X^{-1} = \alpha_{\text{reg}}^{-1} + C_0^{\text{theory}} + k \ln A + \lambda \Phi_{\text{bind}}(A, Z), \tag{13}$$

where $\Phi_{\text{bind}}(A, Z)$ is a dimensionless measure of local nuclear packing stability. A first candidate is

$$\Phi_{\text{bind}}(A, Z) = \frac{B(A, Z)/A}{m_u c^2}, \tag{14}$$

where $B(A, Z)/A$ is binding energy per nucleon. In fractal form:

$$\Phi_{\text{bind}}(A, Z) = \left[\eta \frac{B(A, Z)/A}{m_u c^2} \right]^{3/D_f}, \tag{15}$$

where $D_f \approx 2.477$ is the effective fractal dimension and $\eta \approx 23/27$ is the gyroball packing efficiency.

The most important test is isotope dependence. For Yb isotopes,

$$^{168}\text{Yb},\ ^{170}\text{Yb},\ ^{171}\text{Yb},\ ^{172}\text{Yb},\ ^{173}\text{Yb},\ ^{174}\text{Yb},\ ^{176}\text{Yb}, \tag{16}$$

the $\ln A$ term varies smoothly, while Φ_{bind} should produce tiny isotope-specific residuals. Detection of such residuals would be a strong signature that α is a local boundary-realized coupling rather than a universal external constant.

9.4 Corrected Species-Dependent Recoil Model

The proposed corrected minimal recoil model is

$$\alpha_X^{-1} = \alpha_{\text{reg}}^{-1} + C_0^{\text{theory}} + k \ln A, \tag{17}$$

where A is nucleon number. The use of A, rather than atomic mass M, is essential: the relevant object in TFOFT is the nucleon-register count, not the laboratory atomic mass including cloud and defect corrections.

Using Rb-87 as the calibration point gives

$$k = \frac{\alpha_{\text{Rb}}^{-1} - \left(\alpha_{\text{reg}}^{-1} + C_0^{\text{theory}} \right)}{\ln 87} = -3.65799 \times 10^{-7}. \tag{18}$$

The resulting predictions are

System	A	Predicted α^{-1}	Comment
H-1	1	137.036000840	physical gyroball baseline
Rb-87	87	137.035999206	calibration
Cs-133	133	137.035999051	near observed Cs recoil value
Yb-174	174	137.035998952	sharp pending prediction
Sr-88	88	137.035999202	testable
Ca-40	40	137.035999490	testable
Fe-56	56	137.035999367	local heavy-nuclear reference

The Cs-133 prediction differs from the measured recoil value by only

$$\Delta_{\mathrm{Cs}} \approx 4.7 \times 10^{-9}. \tag{19}$$

The one-point Rb-calibrated model gives

$$\boxed{\alpha^{-1}_{Yb174} \approx 137.035998952} \tag{20}$$

as a near-term recoil target. The Rb/Cs interpolation method in Prediction 4 gives the operative falsification value

$$\alpha^{-1}_{\mathrm{Yb}} = 137.035998945(45).$$

The two values differ by 7×10^{-9}, well inside the stated interpolation uncertainty, so the boxed Prediction 4 value is used for the falsification bands.

This construction is not a two-parameter fit to Rb and Cs. The offset C_0^{theory} is derived from the bare-register residual, the 23/27 gyroball efficiency, and the golden-ratio fractal correction. Only the slope k is calibrated from one recoil datum.

9.5 The Fine-Structure Constant: Rb/Cs and Webb Tensions

The Rb/Cs clock comparison shows a $\sim 5.4\sigma$ tension with the electron $g-2$ value of α^{-1} [38]. Separate analyses of quasar absorption spectra (the Webb et al. dataset) suggest $\Delta\alpha/\alpha \sim 10^{-5}$ variations across the sky.

In TFOFT, α is conjectured to not be a universal constant but a local property of the FTC substrate: it depends on the local packing density through $\alpha(Z) = 1/[T_{\mathrm{sphere}}(1+\varepsilon(Z))^3]$. Different measurement environments probe different effective values of α. The Rb/Cs tension is an early empirical signal of this local variation. The Yb-174 prediction above is the near-term sharp recoil test of this pattern. Using the Rb/Cs-calibrated prediction, the offset from the electron $g-2$ value is approximately 4.70σ with the Rb/Cs calibration uncertainty included, and 14.75σ if only the $g-2$ uncertainty is used.

9.6 NIST Spectral Evidence: Cross-Element Log-Step Quantization

With the core of atoms and galaxies defining the photonic mechanism, we use the two candidate log-steps:

$$k_q^{\mathrm{obs}} = \ln(1.227) \approx 0.20493,$$

the observed Karlsson logarithmic spacing, and

$$k_{\mathrm{info}}^{(0)} = 2\left(\frac{23}{27}\right)^2\left(\frac{4}{27}\right) \approx 0.21501,$$

the FTC-predicted raw Info-channel leakage step. The two differ by approximately 4.7%, matching the finite-shuffling residual discussed elsewhere. The table below checks whether representative atomic spectral gaps across different elements fall near small integer multiples of either spacing.

Element	Z	**Key pair**	$\Delta \ln \nu$	$/k_q^{\mathrm{obs}}$	$/k_{\mathrm{info}}^{(0)}$
H	1	Ly-α / Balmer limit	1.104	$5.39 \approx 5$	$5.13 \approx 5$
H	1	Balmer / Paschen limit	0.812	$3.96 \approx 4$	$3.78 \approx 4$
He	2	He II / He I 584	0.453	$2.21 \approx 2$	$2.11 \approx 2$
Fe	26	Fe II UV / Fe I optical	0.831	$4.05 \approx 4$	$3.87 \approx 4$
Cs	55	Cs II / Cs I D2	0.616	$3.01 \approx 3$	$2.86 \approx 3$
Rb	37	Rb II / Rb I D2	0.610	$2.98 \approx 3$	$2.84 \approx 3$
Yb	70	$^1P_1$ / repump 1389	1.246	$6.08 \approx 6$	$5.80 \approx 6$

Table 4: Cross-element Karlsson-analogue steps from representative NIST spectral data. The table compares each logarithmic gap against both the observed Karlsson spacing $k_q^{\mathrm{obs}} = 0.20493$ and the FTC-predicted raw Info-channel leakage $k_{\mathrm{info}}^{(0)} = 0.21501$.

10 Gravity and Black-Hole Registers

10.1 Soddy Dynamics, Force Hierarchy, and Gravity

10.1.1 The Soddy Curvature Relation

The fundamental equation governing the sphere packing is the Soddy relation [14, 11, 12]:

$$\left(\sum_{i=1}^{4} k_i\right)^2 = 2\sum_{i=1}^{4} k_i^2.$$

Given four mutually tangent spheres with curvatures $k_i = 1/r_i$, the curvature of a fifth tangent sphere is uniquely determined:

$$k_5 = \sum_{i=1}^{4} k_i \pm 2\sqrt{\sum_{i<j} k_i k_j}.$$

10.1.2 Möbius Invariance and Boundary Crossing

The Soddy relation is invariant under Möbius transformations. At the fractal boundary, an infalling star ball carries angular momentum $\mathbf{L} = m\mathbf{r} \times \mathbf{v}$. Möbius inversion preserves $\mathbf{L}$:

$$\mathbf{L}_{\mathrm{after}} = \mathbf{L}_{\mathrm{before}}.$$

The ball emerges into the higher scale as an info ball. Linear momentum, which depends on absolute velocity, does not survive the crossing. Angular momentum, which is frame-independent and scale-invariant by definition, is the conserved quantity carrying information across fractal layers.

10.1.3 Coupling Strength Hierarchy: One Boundary Force Seen Across Scale

TFOFT interprets the four standard fundamental forces as projections of one FTC boundary interaction rather than as four ontologically separate force particles. The observed force depends on which side of the fractal scale boundary is sampled and which direction the causal flow takes. At the here-scale, the two visible long-range channels are gravity and electromagnetism. Across the lower fractal boundary, the same channels reappear as the two short-range nuclear channels:

$$\text{weak} \equiv \text{local electromagnetism at the lower fractal scale,}$$

$$\text{strong} \equiv \text{local gravity at the lower fractal scale.}$$

This gives the FTC interpretation of electroweak unification: weak behavior and electromagnetic behavior are adjacent-scale expressions of the same boundary channel. The strong interaction behaves as an extreme confinement force because it is lower-scale gravity expressed inside the Core-boundary geometry.

The Soddy relation involves exactly four mutually tangent spheres, and the tangency order supplies the finite bookkeeping of coupling strengths. First-order boundary alignment gives the electromagnetic register probability. Second-order boundary alignment gives the weak lower-scale electromagnetic channel. The Core-binding channel appears as lower-scale gravity confined inside the nucleon/Core boundary. The global metric channel is the large-scale averaged gravitational expression of the same tangent-register dynamics.

Gauge-boson language remains useful as Standard Model transition bookkeeping. Photons remain Info Balls in transport because they are the observed cross-scale angular-momentum carriers. Gluons are treated as Standard Model internal labels for confinement bookkeeping, corresponding in TFOFT to lower-scale gravity-binding behavior inside the Core-boundary channel, with no independent separable-object role. Standard Model gauge groups remain effective symmetry descriptions of these boundary channels; the FTC ontology assigns physical priority to scale crossing, tangency order, and register flow.

10.1.4 Laurent Expansion of the Möbius Map

The Möbius map near a tangency point at $r = r_0$ gives an effective gravitational acceleration expanded around the Soddy core radius $r_s = 2GM/c^2$:

$$a_{\text{grav}}(r) = \frac{2v^2}{r} - \frac{4v^2 r_s}{r^2} + \frac{6v^2 r_s^2}{r^3} - \frac{8v^2 r_s^3}{r^4} + \mathcal{O}(r_s^4/r^5) \tag{21}$$

In any given physical interaction, G, M, and m are constants; only r varies. The $1/r^2$ dependence arises from the first-order term above—a rational function of r with constant coefficients, entirely within Presburger arithmetic (constant multiplication = repeated addition).

The Newtonian coefficient is recovered exactly at the dyadic octant lock

$$v^2 = \frac{c^2}{8}.$$

Since $r_s = 2GM/c^2$, the first-order Möbius term becomes

$$-\frac{4v^2 r_s}{r^2} = -\frac{4(c^2/8)(2GM/c^2)}{r^2} = -\frac{GM}{r^2}.$$

The factor $8 = 2^3$ is the oriented-octant split of a three-dimensional spherical register, so Newtonian gravity appears as the octant-locked $1/r^2$ term of the cross-scale Möbius flow.

Term	**Form**	**Physical identification**
0th	$+2v^2/r$	Centripetal balance; flat rotation curve
1st	$-4v^2 r_s/r^2$	Newtonian gravity under the octant lock $v^2 = c^2/8$
2nd	$+6v^2 r_s^2/r^3$	GR perihelion precession
3rd	$-8v^2 r_s^3/r^4$	Frame-dragging / Lense–Thirring

The zeroth-order term is consistent with flat galactic rotation curves directly from the Möbius geometry, without requiring additional dark matter at large radius. The weak-field gravitational hierarchy emerges from the first-order and higher-order terms of Möbius-ASSP geometry under this ontology, valid when $r \gg r_s$.

10.1.5 Gravity Emerges from Geometry

Gravity is conjectured not to be a fundamental force in the TFOFT picture, but the effective geometric consequence of Soddy packing boundary curvature at the fractal layer interface, operating under conservation of angular momentum across the boundary. The gravitational constant G is therefore conjectured not to be an independent fundamental constant but to emerge from the geometry of the ASSP and the Presburger computational constraints—consistent with its independent derivation below from the hierarchy depths and fractal dimension.

10.2 Deriving G: Geometric Baseline and Dynamic Virial Route

10.2.1 Conceptual Framework

Under this ontology, gravity emerges from Möbius inversion geometry at Soddy tangency points, where the three-dimensional bulk packing meets the two-dimensional boundary crossing. The value of G is determined by the depths of the mass, radius, and time hierarchies, together with the difference in Hausdorff dimensions between the 3D Soddy bulk and the 2D Apollonian gasket boundary.

We present two complementary routes:

- **Method 1 (Geometric baseline):** uses the mass and radius hierarchy depths weighted by the two Hausdorff dimensions. This gives the homogeneous Apollonian-boundary baseline G_0.
- **Method 2 (Dynamic virial route):** uses the radius hierarchy depth and the observed ratio of orbital frequencies across the fractal boundary, then applies a predicted Fractal Virial Correction FVC $= \ln(27/2)$. This gives the locally virialized estimate G_{dyn}.

No value derived from G enters either route. The geometric route uses

$$N_{\text{radius}} = \frac{\alpha_{\text{ASSP}}^{-1}}{\varphi} = 84.6931,$$

where

$$\alpha_{\text{ASSP}}^{-1} = 4\pi^3 + \pi^2 + \pi = 137.0363038.$$

10.2.2 Three Hierarchy Depths

$$N_{\text{hierarchy}} = T_{\text{two-ball}} = 138.9550, \tag{22}$$
$$N_{\text{radius}} = \alpha_{\text{ASSP}}^{-1}/\varphi = 84.6931, \tag{23}$$
$$N_{\text{time}} = \ln(f_e/f_s) = 72.9217. \tag{24}$$

Here $N_{\text{hierarchy}}$ denotes the two-ball electron–star logarithmic hierarchy used in the gravitational calculation; the 77-layer mass register remains S_{mass}. The observed electron–solar hierarchy,

$$\ln(M_\odot/m_e)_{\text{obs}} = 138.9358,$$

is a cross-check on the internally derived two-ball register depth and enters neither route as an input.

The CODATA/NIST Earth value corresponds to

$$\ln\left(\frac{c^3}{G\hbar}\right)_{\text{obs}} = 160.2207$$

using the measured value of G [27].

10.2.3 Method 1: Geometric Baseline

The geometric baseline is

$$\boxed{\ln\left(\frac{c^3}{G\hbar}\right)_0 = (N_{\text{hierarchy}} + N_{\text{radius}}) - (D_S - D_A)(N_{\text{hierarchy}} - N_{\text{radius}})}$$

where $D_A = 1.305687$ is the 2D Apollonian gasket dimension [13] and $D_S = 2.47390$ is the 3D Soddy packing dimension [11]. With

$$N_{\text{hierarchy}} = 138.9550, \qquad N_{\text{radius}} = 84.6931, \qquad D_S - D_A = 1.168213,$$

the result is

$$\ln\left(\frac{c^3}{G\hbar}\right)_0 \approx 160.259.$$

Thus the homogeneous ASSP geometric baseline is

$$G_0 = \frac{c^3}{\hbar \exp(160.259)} \approx 6.43 \times 10^{-11}\ \text{m}^3\,\text{kg}^{-1}\,\text{s}^{-2}.$$

This sits about 3.7% below the Earth/NIST value. In the FTC ontology, G_0 is the homogeneous Apollonian-boundary baseline before local density and virial packing renormalization, while the locally measured laboratory value is the dense-region realization.

10.2.4 Method 2: Dynamic Clock Route and the Fractal Virial Correction

The second route starts from the dynamic radius–time hierarchy:

$$L_G^{\text{dyn},0} = N_{\text{radius}} + N_{\text{time}} = 84.6931 + 72.9217 = 157.6148.$$

This is not yet the local gravitational hierarchy, because the radius-clock system must be virialized into a bound two-ball geometry. The relevant Euclidean update volume for a shared three-dimensional angular-momentum state is the naive cubic register volume

$$3^3 = 27.$$

A bound virialized two-ball system splits total update energy between motion and binding, producing the usual half-factor. Therefore the Fractal Virial Correction is predicted to be

$$\boxed{\text{FVC} = \ln\left(\frac{3^3}{2}\right) = \ln\left(\frac{27}{2}\right) = 2.60269.}$$

Thus

$$L_G^{\text{dyn}} = N_{\text{radius}} + N_{\text{time}} + \text{FVC} = 84.6931 + 72.9217 + 2.60269 = 160.2175.$$

This corresponds to

$$G_{\text{dyn}} = \frac{c^3}{\hbar \exp(160.2175)} \approx 6.70 \times 10^{-11}\ \text{m}^3\,\text{kg}^{-1}\,\text{s}^{-2},$$

within approximately 0.4% of the Earth/NIST value.

The dynamic route therefore gives the local virialized estimate, while the geometric route gives the homogeneous Apollonian-boundary baseline. The difference between them is interpreted as the effect of local packing density and star–core transfer shuffling.

10.2.5 Interpretation and Prediction

The exact Apollonian boundary projection gives a homogeneous geometric baseline

$$G_0 \approx 6.43 \times 10^{-11},$$

about 3.7% below the Earth/NIST value. The dynamic virial route, using the predicted Fractal Virial Correction

$$\mathrm{FVC} = \ln(27/2),$$

gives

$$G_{\mathrm{dyn}} \approx 6.70 \times 10^{-11},$$

within approximately 0.4% of the Earth/NIST value.

In the FTC ontology this is the expected ordering. The homogeneous ASSP-boundary value describes an idealized average packing. The Earth–Sun environment is a dense, virialized, star–core packing region. Dense regions increase the local effective curvature throughput and therefore raise G_{local} relative to the homogeneous baseline. Underdense regions are expected to lower G_{local} relative to the same baseline. Thus local shuffling redistributes curvature throughput across the ASSP. Star–core transfer continuously reshuffles the local values of α_{local}, $D_{\mathrm{eff,local}}$, and G_{local}. The global effect is approximately zero-sum: enhancement in dense regions is balanced by suppression in underdense regions.

The testable prediction is therefore correlated variation, not random laboratory scatter:

$$\Delta G \quad \leftrightarrow \quad \Delta\alpha \quad \leftrightarrow \quad \Delta D_{\mathrm{eff}}.$$

Measurements of G in environments with different local substrate density—for example Earth, Mars, compact-object environments, and intergalactic filaments—are predicted to yield tiny but systematically different effective values.

PREDICTION 3: Emergent and Locally Renormalized Gravitational Constant

$$G_0 = \frac{c^3}{\hbar\, \exp\!\big[(N_{\mathrm{hierarchy}} + N_{\mathrm{radius}}) - (D_S - D_A)(N_{\mathrm{hierarchy}} - N_{\mathrm{radius}})\big]} \approx 6.43 \times 10^{-11}$$

with

$$N_{\mathrm{radius}} = \frac{\alpha_{\mathrm{ASSP}}^{-1}}{\varphi} = 84.6931.$$

This is the homogeneous Apollonian-boundary baseline. The local virialized Earth value is obtained by adding the dynamic Fractal Virial Correction

$$\mathrm{FVC} = \ln(27/2),$$

giving

$$G_{\mathrm{dyn}} \approx 6.70 \times 10^{-11},$$

within $\sim 0.4\%$ of the NIST value.

The theory predicts that G is not a primitive universal constant but a locally renormalized output of the ASSP substrate. Dense, virialized star–core environments should measure larger G_{local} than the homogeneous baseline, while underdense regions should measure smaller G_{local}. Zero fitted G-inputs are used.

10.3 Sagittarius A* as a 137-Step Spherical Register

This section gives a string-theory derivation check on Sagittarius A*. The calculation treats the standard extremal three-charge black-hole entropy formula as an effective register-counting model and asks whether it recovers the same logarithmic channel depth predicted by the FTC single-sphere register. In TFOFT, the Core Ball couples to surrounding registers through the same finite three-channel causal depth that gives the elementary 1/137 accepting probability.

The standard extremal three-charge entropy form is

$$W = \exp\left(2\pi\sqrt{Q_1 Q_5 N}\right), \qquad S = \ln W = 2\pi\sqrt{Q_1 Q_5 N}.$$

This expression is useful here because it counts an extremal spherical black-hole register using three independent quantum numbers. The form is the standard string-theory microstate-counting result for a class of five-dimensional extremal black holes, where the Bekenstein–Hawking area entropy is recovered by counting BPS bound-state degeneracies [39, 40]. In FTC language, a complete spherical register also has three independent channels: surface, phase, and radial displacement. Thus an effective string-theoretic microstate-counting model, when applied to an extremal Core Ball, should land on the same logarithmic channel depth that controls the single-sphere register.

Approximating Sagittarius A* by its Planck-scale mass gives a Bekenstein–Hawking entropy of order

$$S_{\mathrm{SgrA}^*} \approx 1.93 \times 10^{90}.$$

Here the entropy is computed from the Bekenstein–Hawking area law, $S_{\mathrm{BH}} = A/(4\ell_P^2)$, using the observed Sagittarius A* mass scale $M_{\mathrm{SgrA}^*} \approx 4.3 \times 10^6 M_\odot$ [41, 42, 43]. The corresponding three-channel product is then

$$Q_1 Q_5 N \approx 9.42 \times 10^{178}.$$

For an equal three-channel split,

$$Q_i = (Q_1 Q_5 N)^{1/3},$$

and therefore

$$\ln Q_i = \frac{1}{3}\ln\left(9.42 \times 10^{178}\right) = \frac{1}{3}\left(\ln 9.42 + 178 \ln 10\right) \approx 137.37.$$

This lands within roughly 0.24% of the ASSP single-sphere register depth

$$T_{\mathrm{sphere}} = 4\pi^3 + \pi^2 + \pi = 137.0363038\ldots.$$

TFOFT reads this as a macro-register cross-check. The Milky Way core behaves like a spherical fractal register whose effective three-channel charge depth lands on the same 137-log step causal scale as the single Soddy-sphere update. The Sagittarius A* calculation is an independent Galactic-core/register hint that the successful extremal black-hole state-counting template already points to the FTC register depth. In this limited sense, the extremal three-charge result functions as an effective string-theory check on the FTC register architecture: it recovers the same three-channel logarithmic depth without assuming the TFOFT ontology. The same comparison also suggests a stronger black-hole interpretation. If the extremal three-charge state-counting model is the effective register description that recovers the 137-log channel depth, then the physically realized Core Ball should be extremal in the GR sense: a boundary-saturated object whose charge, spin, and mass sit at the stable register limit. In this reading, astrophysical black holes are never sub-extremal singularity containers. They are extremal Core Ball registers viewed through the coarse language of GR [39, 40, 44, 45].

This resolves the singularity problem of GR geometrically. A sub-extremal Schwarzschild-like continuation contains a central point singularity: a measure-zero infinite-density object

forbidden by MATHICCS. Extremal geometries replace that terminal point with a boundary-saturated throat. In the ideal Reissner–Nordström or Kerr-Newman case, the near-horizon extremal geometry develops a long stable throat, often locally modeled by an $AdS_2 \times S^2$-type factor. TFOFT interprets this throat as the GR shadow of the actual Core Ball connector: the nonlocal scale-crossing channel that links galaxy cores across the higher fractal register [44, 45, 46, 47, 48].

The throat is therefore not empty mathematical excess. It is the coarse-grained signature of the superluminal connector used by the nonlocal jet mechanism. Here-scale GR sees an extremal throat because it is trying to describe a fractal register boundary with continuum geometry. TFOFT reads the same structure as a Core-to-Core transport channel: angular momentum and Info Ball flux cross the boundary through the higher fractal layer, while lower-scale Dust Ball production carries the computational cost. This connects the Sagittarius A* 137-step register check, the absence of physical singularities, and the nonlocal AGN jet channel into one Core Ball picture [44, 48].

10.4 G Objects as Core-Boundary Crossing Hints

The Galactic-center G objects provide a qualitative test of whether Sgr A* behaves like a smooth gravitational sink or like a register boundary with crossing conditions. Observationally, these objects are compact through most of their orbits, stretch near closest approach to Sgr A*, and occupy the ambiguous category of objects that look gas-like while moving star-like [49, 50]. In FTC language this is the expected signature of a Core-boundary crossing: outside the boundary the object remains a coherent register, while near periapse the boundary condition opens and the object partially reconstructs into lower-layer substrate.

This does not by itself prove quantization. Its significance is structural: the response is localized to a crossing phase rather than distributed smoothly over the full orbit. The G objects therefore function as a nearby Sgr A* test case for the same rule used elsewhere in TFOFT: a Core Ball does not merely exert a continuous force field; it admits discrete state changes when an orbiting object crosses the register condition.

11 TFOFT Origin Picture: Post-Fusion Hydrogen Ejection in a Larger Fractal Structure

TFOFT treats the observable universe as one layer inside a potentially unbounded self-similar fractal. The same atom–galaxy relation that identifies stars with electrons and galactic cores with nuclei implies that the macro-hydrogen galaxies in our observable universe are constituents of a larger parent structure. Since ordinary visible matter is overwhelmingly processed through stars, and since stars fuse hydrogen into helium and heavier nuclei while ejecting hydrogen-rich material through winds, jets, and envelope loss, the natural TFOFT origin picture is that our observable universe is the relaxed hydrogen-rich ejecta of a post-fusion event in a parent-scale stellar object [51, 52].

In this picture, the galaxies visible to us are macro-hydrogen atoms after ejection from the parent-scale fusion process. The compact high-redshift "little red dots" found by JWST are interpreted as likely macro-helium or higher-fusion products inside the same ejection history. Their observed compactness, redness, high densities, broad hydrogen/helium features, and debated AGN versus dense-star-formation interpretations make them natural candidates for post-fusion macro-atoms in TFOFT rather than ordinary early galaxies forming from a pristine Big Bang timeline [53, 54, 55].

The same mechanism also gives the TFOFT quasar picture. A simple macrophoton transfer can move one Star Ball from one galaxy/Core Ball system into the jet or boundary channel of another. A parent-scale fusion event that produces gamma rays therefore has a macro-analogue:

every single stellar angular-momentum register from a compressed galaxy are dumped through its Core Ball and re-emerge through another Core Ball as an ejected quasar with intrinsic redshift. The stars then relax into place around the new Quasar Core Ball and become the observed quasar host galaxy. More distant and more highly redshifted quasars should therefore have denser, less-relaxed hosts, while lower-redshift quasars should have larger and more relaxed hosts after longer post-ejection settling.

The redshift of ordinary distant galaxies comes from here-layer propagation through the inhomogeneous fractal mass distribution. Light remains in our fractal layer and undergoes ordinary gravitational lensing as it passes through galaxy halos, void boundaries, filaments, and Core Ball environments. These repeated small direction changes act as Brownian angular scattering. The accumulated path bending changes the photon path length, phase relation, and angular-momentum bookkeeping, and the here-scale projection records the accumulated directional scrambling as redshift. The optical sharpness of quasars is therefore a red herring for distance: quasar redshift includes intrinsic Core Ball ejection redshift, while ordinary galaxies show the expected blurring and distortion from cumulative lensing along the path.

The same propagation picture gives a selection effect. After many Brownian lensing deflections, the probability that a random ray intersects the Milky Way is extremely small. The most highly redshifted sources visible to us are the rare rays whose lensed Brownian paths still terminate on our local galaxy and detector. High redshift in this picture is partly a survival-and-alignment filter: the photons we observe are the lucky paths that remain in the here-layer and still hit us after many accumulated direction changes.

The Brownian lensing redshift has a floor when the photon stops efficiently interacting with matter and the fractal substrate. TFOFT identifies this transparency floor with the millimeter microwave background. The CMB is the accumulated and thermalized light of the universe after repeated gravitational billiard scattering, not a relic from a singular beginning. This resolves Olbers' paradox directly: the sky is not optically bright because the accumulated light has been degraded into the microwave band. The observed CMB blackbody peak at millimeter wavelengths is therefore the final low-loss transparency channel of here-layer light [56, 57, 58, 59].

The millimeter scale also connects to hydrogen collapse physics. Molecular-cloud gas has typical bulk densities near $n \sim 100\,\mathrm{cm}^{-3}$, while star-forming regions extend into much denser regimes. The mean inter-particle spacing $n^{-1/3}$ for $n \sim 10^2$–$10^4\,\mathrm{cm}^{-3}$ is naturally of order 0.5–2 mm. Thus the CMB wavelength scale is also the characteristic spacing scale of hydrogen-rich gas approaching gravitational collapse. In TFOFT this is not a structural coincidence: the here-scale edge ball is the same millimeter-scale channel that marks both the low-loss photon floor of the fractal substrate and the hydrogen spacing regime from which stars condense [60, 61].

12 Dark Matter, Lower-Scale Substrate, and Cosmology

12.1 The Dark Matter Fraction from the Laderman Rank-23 Overhead

The addition-only fraction ($4/27 \approx 14.8\%$) represents the computationally efficient (luminous) part. The multiplication-heavy overhead fraction ($23/27 \approx 85.2\%$) is the conjectured origin of the dark-matter fraction.

12.2 The Non-Darkness of Dark Matter: Fractal Electron Manufacture

In TFOFT, dark matter is conjectured to be **lower-scale hydrogen gas**—the cold, diffuse hydrogen fuel of the star balls we identify as electrons at the here-scale. Close to a gravitational well, this substrate becomes locally dense enough to cause lower-scale hydrogen gas at sufficient pressure to ignite lower-scale fusion, producing here-scale electrons. To a here-scale observer, its energy output is conjectured to manifest as anomalous heating in dense compact objects, the Fermi bubbles (Section 16.1.3), and the warm-hot intergalactic medium.

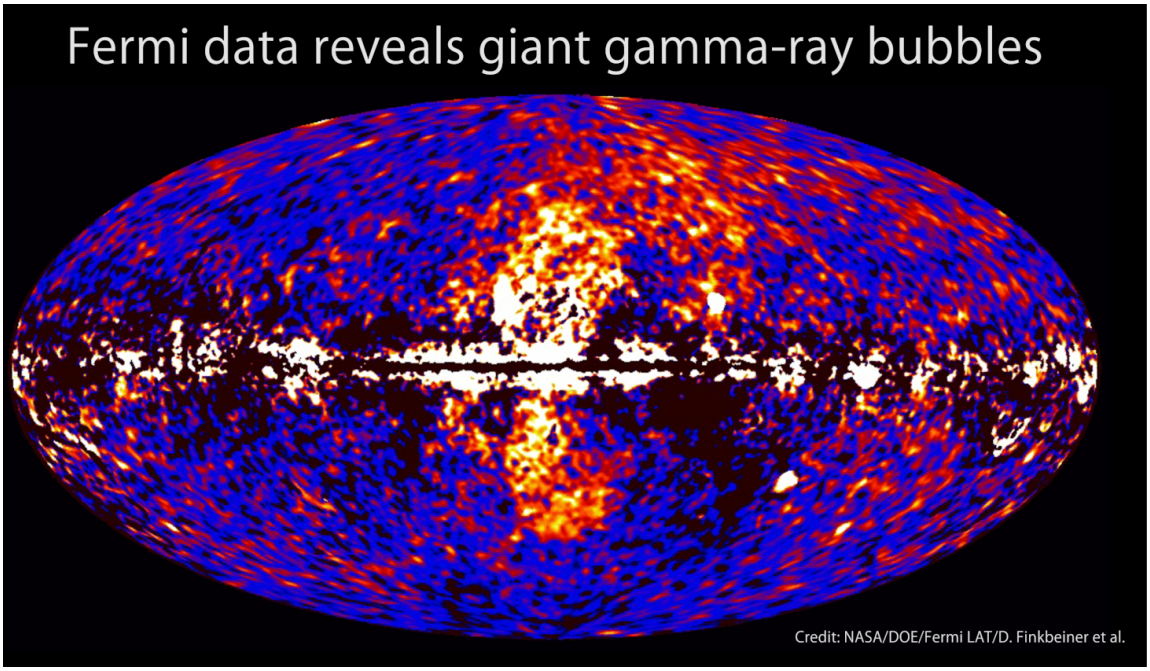

Figure 4: Fermi bubbles observed by the Fermi Large Area Telescope. The two giant lobes extend $\approx$ 50 kly above and below the galactic plane. In TFOFT these are interpreted as the visible signature of lower-fractal-layer hydrogen fusion inside the dark-matter halo (the scaled "$3d_{z^2}$" orbital shell of the galactic fractal hydrogen atom). The predicted bubble height ($\frac{23}{27}R_{\text{halo}} = 49.8$ kly) matches the observed $\approx$ 50 kly to 0.4%. The observed lobe offset from the galactic z-axis ($\approx$ 55–60°) is consistent with the $3d_{z^2}$ nodal cone half-angle $\arccos(1/\sqrt{3}) \approx 54.7°$—a parameter-free geometric prediction of the ASSP orbital shell model.

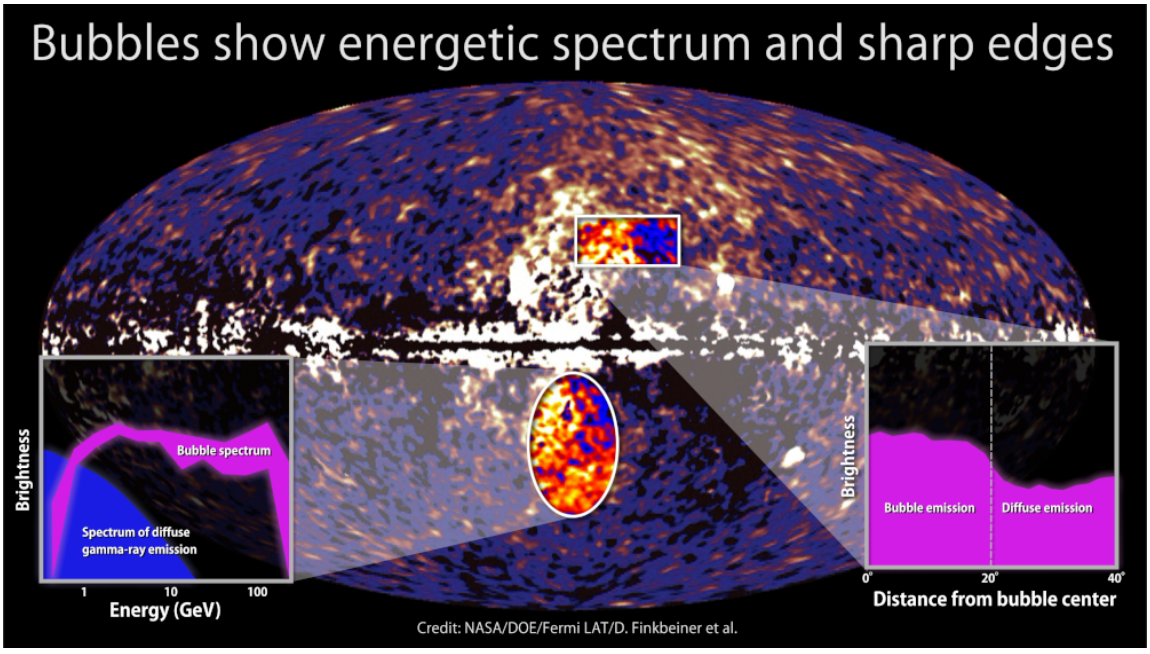

Figure 5: Same Fermi bubbles with insets showing the hard power-law spectrum inside the bubbles versus the diffuse galactic emission, and the extremely sharp edge consistent with a Soddy-sphere boundary in the fractal dark-matter halo.

Credit (both panels): NASA/DOE/Fermi LAT/D. Finkbeiner et al. Source: NASA SVS #10688. Original discovery and subsequent morphology studies: Su, Slatyer & Finkbeiner; Dobler et al.; Ackermann et al. [62, 63, 64].

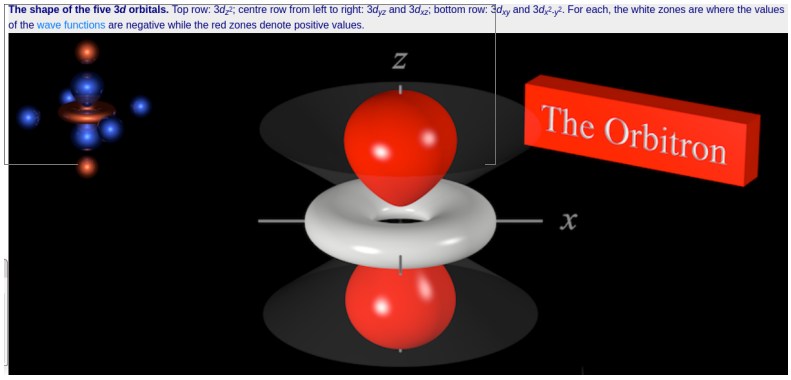

Figure 6: The hydrogen $3d_{z^2}$ orbital (probability density isosurface). The nodal cone half-angle is $\arccos(1/\sqrt{3}) \approx 54.7°$ from the z-axis—fixed by quantum mechanics with no free parameters. The observed Fermi bubble offset of ≈ 55–$60°$ from the Milky Way's rotation axis matches this value, supporting the identification of the dark-matter halo as the galactic-scale analogue of the $3d_{z^2}$ orbital shell.

Credit: Chemistry LibreTexts / Orbitron (M. Winter, Univ. Sheffield). Public domain for academic use.

At every fractal scale N, the orbital shell of scale-N objects around scale-N cores is conjectured to be the dark matter halo of scale N. At sufficient density, this shell spontaneously generates scale-$(N-1)$ objects—a subset of the fractal quine instruction set executing itself at every scale simultaneously. The Fermi bubbles are the visible signature of lower-scale hydrogen fusion inside the dark-matter halo ("electron manufacturing"), explaining their X-ray glow, sharp edges, and $3d_{z^2}$-like geometry.

12.3 Info-Ball Transfer Cost and Dark-Matter Production

In FTC transport, the fast part of the event is angular-momentum transfer through the Info Ball. The receiver experiences the transfer as effectively instantaneous at the here-scale because the angular-momentum address is delivered through the higher-scale channel and output via a core jet rather than propagated as a slow local material stream. The accounting still balances locally: the angular-momentum transfer cost is paid downward as lower-scale linear momentum.

This is the physical role of the Laderman split. The coherent register channel carries the luminous, addressable part of the event, while the multiplication-heavy remainder is exhausted into lower-scale Kick-Ball/Dust-Ball substrate. In astrophysical language, the cost of Info-Ball transfer is dark-matter production.

12.4 Quantum Nature of Light and the Galactic Photoelectric Effect

The interaction of jets with galactic dark-matter halos is conjectured to be the here-scale analogue of the atomic photoelectric effect, with four distinct regimes determined by jet energy and stripping timescale:

1. **Low-energy, no stripping (recycled jet).** The incoming info ball material in a core jet lacks sufficient energy to remove dark-matter halo material. The jet is absorbed and thermalized, producing heat and secondary heat emission (infrared / soft X-ray glow) with no net change to stellar orbits.

2. **Low-energy, slow stripping (adiabatic Keplerian relaxation).** Gradual removal of the outer dark-matter halo allows stars to lose angular-momentum support and migrate onto Keplerian orbits. Stars spiral inward along the galactic equator, collide with the core,

and are re-ejected as info balls (macrophoton "reflection"). The galaxy remains bound but becomes more centrally concentrated.

3. **High-energy, fast stripping (photoelectric work-function threshold).** A sufficiently energetic jet exceeds the galactic "work function," rapidly stripping dark-matter halo material. Stars are flung off the disk plane (orthogonal to the jet polarization / momentum), becoming hypervelocity stars. This is the conjectured galactic analogue of the atomic photoelectric effect.

4. **Extreme-energy, dense angular-momentum injection (quasar regime).** A high-angular-momentum Fast Ball reconstructing from wish-scale Info-Ball transport gravitationally perturbs the *Arp peculiar parent*: the connected lower-redshift parent system identified by disturbed morphology, bridges, filaments, or gas trails. This parent is not the same object as the apparent same-redshift "host" galaxy. In TFOFT, the same-redshift host is interpreted as material shed by the quasar during relaxation into our substrate, which is why it shares the quasar redshift. The peculiar parent is the older galactic register that launched or received the cross-scale event. Stars in that parent are statistically pulled off in a broad jet-direction spray, producing a hypervelocity-star excess aligned with luminous quasar axes. Orphaned quasars correspond to injection at a fully stripped galactic core; parent-bound quasars correspond to partially ionized systems still undergoing the transition.

This framework is falsifiable: Arp-type peculiar parent galaxies connected to luminous quasars by disturbed gas trails, bridges, or filamentary alignments must show a statistically significant excess of hypervelocity stars in the jet hemisphere compared with matched quiescent controls. The apparent same-redshift host should instead behave like relaxation debris shed from the quasar itself as it recoalesces into the here-scale substrate.

12.5 Dark Matter–Neutrino Interactions

Several experiments have reported indications of anomalous neutrino behavior in environments where the inferred dark-matter density varies. In the Standard Model, neutrinos do not interact with dark matter at leading order, so a true neutrino–dark-sector interaction would normally require new mediator particles.

In TFOFT, the situation is different because dark matter is not a new here-scale particle species. It is lower-scale hydrogen plasma: a gas of lower-layer Gyro Balls and constituents. Neutrinos are Code Balls, identified with sub-stellar lifecycle objects at the lower scale. A neutrino moving through a dark-matter-rich region is therefore a tiny planet-like object moving through a tiny gas. The interaction is literal drag, accretion, stripping, and lifecycle evolution inside the lower-scale substrate.

Flavor change is then interpreted as a change in the Code Ball lifecycle state. A rocky/terrestrial Code Ball corresponds to the electron-neutrino channel; after accumulating enough lower-scale gas it can become a gas-giant-like object, corresponding to the muon-neutrino channel; with further accumulation it can become brown-dwarf-like, corresponding to the tau-neutrino channel:

$\nu_e \leftrightarrow$ rocky/terrestrial Code Ball, $\quad \nu_\mu \leftrightarrow$ gas giant Code Ball, $\quad \nu_\tau \leftrightarrow$ brown dwarf Code Ball.

The reverse direction can also occur. Atmosphere stripping, tidal disruption, heating, collapse, or explosive recycling can move a Code Ball back down the lifecycle chain. At larger scales the same sequence continues through red-dwarf ignition, stellar growth, supernova disruption, and recoalescence into rocky bodies. Thus flavor oscillation is not merely an abstract internal quantum rotation; it is the here-scale projection of lower-scale planetary lifecycle transitions under gas drag and substrate exchange.

No new mediator particle is required under this ontology. The apparent neutrino–dark-matter interaction is the ordinary mechanical interaction of tiny planets with tiny gas: drag changes momentum, accretion changes mass and envelope state, stripping removes accumulated substrate, and the observed flavor channel records which lifecycle basin the Code Ball occupies when it is detected.

12.6 Implications for Cosmology: The Two-Component Redshift

In the TFOFT framework, the observed redshift of a distant source has two components. The dominant component is statistical: light remains in our fractal layer and undergoes ordinary gravitational lensing through the inhomogeneous ASSP mass distribution. The accumulated small changes in ray direction act as Brownian angular scattering. The here-scale projection records the resulting loss of directional coherence as redshift, giving the leading logarithmic behavior

$$z_{\mathrm{B}} \propto \ln r.$$

This also introduces a selection effect: after many Brownian lensing deflections, the probability that a random ray intersects the Milky Way is extremely small. The most highly redshifted sources visible to us are therefore not ordinary straight-line samples of the distant universe; they are the rare rays whose lensed Brownian paths happen to terminate on our local galaxy. High redshift in this picture is partly a survival-and-alignment filter: the photons we observe are the lucky paths that remain in the here-layer and still hit our detector after many accumulated direction changes.

A secondary component arises from coherent motion relative to the local fractal substrate: an isotropic ejection field produces an apparent isotropic expansion, while the directed motion of this ejection appears as a Doppler-like anisotropic correction. Standard cosmology conflates both the Brownian lensing deflections and the isotropic ejection signal with its coherent-motion correction into a single metric expansion [2]; decomposing them is conjectured to be the key to reconciling the observational tensions discussed in Section 12.7.

12.7 Objections from Standard Cosmology and TFOFT Resolutions

The following table summarizes the major objections raised by mainstream cosmology against non-cosmological or intrinsic-redshift interpretations of quasars, together with the resolutions provided by the complete TFOFT macro-star ejection + fractal quine framework.

Table 5: Standard Objections vs. TFOFT Resolutions

Standard Objection	**TFOFT Resolution**
Mature, metal-rich, structured quasar host galaxies at high z (JWST)	Quasars are recycled dense galaxy cores ejected from parent macro-stars. They carry pre-existing mixed stellar populations and enriched material from the parent. The quasar phase is a compact relaxation stage that rapidly reorganizes into normal galactic structure using recycled fusion products and non-local jet inflow. JWST "early" galaxies are naturally explained as recently ejected material still relaxing.

Continued on next page

Standard Objection	TFOFT Resolution
Continuous Lyman-alpha forest with cosmological clustering statistics	The forest is primarily a photonic register readout of the quasar's quantized core-crossing birth event and its radial ejection trajectory through the fractal substrate. Secondary absorption from intervening ejected macro-H, i.e. lower-layer hydrogen, modulates the signal according to local fractal density. A uniform base pattern is expected from identical hydrogen-like registers.
Time dilation in quasar variability and supernovae	Differential clock rates arise in the macro-star gravitational potential well. The light from distant objects was emitted from deeper in the gravitational well of the parent star, where clocks tick slower. Quasars preserve their birth-clock redshift from manufacturing depth.
Gravitational lensing time delays	The observed delays combine geometric path-length differences with differential ejection depth and clock desynchronization between lensed images.
Lack of statistical parent-galaxy associations in large surveys	Many quasars originate from naked cores, i.e. quiet massive black holes. Visible Arp-style associations occur when the parent core has a stellar flock and connected gas trails or bridge structure.
Mass budget for building massive hosts	Quasars are dense recycled cores carrying substantial baryons from the parent macro-star plus non-local material inflow during crossing. No primordial gas reservoir is required.
Large-scale isotropy	Radial isotropic ejection from the macro-star plus fractal self-similarity appears homogeneous at our scale. Residual dipoles, including the CMB and quasar dipoles, remain as finite-shuffling signals.
Quasar dipole $\sim 94^\circ$ offset from CMB dipole	Quasars have 3–5$\times$ faster ejection velocity due to higher manufacturing energy. The offset arises from angular momentum precession during parallel macro-gamma-ray core-crossing injection.
Continuous quasar redshifts and Karlsson periodicity	Macro-gamma-ray production across continuous depths plus outward motion of target macro-H smears birth locations into a continuous distribution. Discrete core-crossing events produce the quantized Karlsson steps.

12.8 The CMB Blackbody Spectrum and Acoustic Peaks

The observed CMB is a near-perfect 2.725 K blackbody with temperature anisotropies at 10^{-5} and an angular power spectrum showing acoustic peaks, harmonic structure, and a Silk-damping tail [2]. Standard cosmology interprets this as relic radiation from a primordial plasma that recombined $\sim$380,000 years after a singular beginning.

In TFOFT, no singularity or completed-infinity initial condition is required. The CMB is interpreted as the present-time steady-state resonant eigenmode of the lower-fractal-layer hydrogen plasma in which the here-scale galactic layer is immersed.

- *Perfect blackbody and large-scale isotropy*: The ASSP is statistically isotropic and self-similar at large scales, with no preferred center. The blackbody spectrum itself is a

mathematical consequence of the fractal substrate dynamics: photons undergoing Brownian random walks through the ASSP obey, in the continuum limit, the heat equation. The observed Karlsson quantization of redshifts [18, 19] implies quantized energy levels in this heat equation. Quantizing a heat equation yields phonons, and phonon occupation statistics produce a Planck distribution. The CMB blackbody curve is therefore conjectured to be the natural spectral signature of quantized random walks through the fractal substrate, not a frozen relic requiring a singular origin. Furthermore, the here-scale Edge Ball range (0.1–2 mm) coincides with the CMB peak wavelength range and with the opacity-limit type boundary of hydrogen collapse: the scale-crossing point where radiative cooling, optical depth, and gravitational compression cease to be scale-free and begin bootstrapping stellar ignition. This convergence of the computational boundary, the thermodynamic opacity boundary, and the observed spectral peak is a structural feature of the ASSP geometry.

- *Acoustic peaks*: Interpreted literally as sound waves in the macro-hydrogen gas of the universe. In TFOFT the cosmic substrate is a here/wish-scale hydrogen plasma, so the CMB peak structure is an active standing-pressure spectrum confined by Apollonian boundary geometry at multiple scales. The peaks are Soddy-tangency acoustic resonances of the current fractal substrate, not merely frozen relics from a primordial sound horizon.

- *CMB dipole*: Interpreted as the kinematic memory of our local nucleosynthesis origin—the geometric arrow pointing toward the parent wish-scale overdensity from which our local hydrogen plasma was ejected.

- *Cosmic birefringence* ($\beta \approx 0.3°$, nearly isotropic) [65]: Consistent with a single dominant Möbius boundary twist imposed by the local Null Core (void sphere). All traversing radiation receives one net polarization rotation, isotropic at leading order.

- *The 25-arcminute seam*: $\theta_c = 1/\alpha^{-1}$ rad $\approx 25.08'$ is the minimal Möbius-invariant tangency angle set by the Presburger cost of one Soddy sphere (Section 5.3.1).

Image credit: By Piquito veloz / Celestia software / NASA/ESO. Courtesy NASA/JPL-Caltech and Planck U.S. Data Center at IPAC, CC BY-SA 4.0.

12.9 The Hubble Tension and JWST Early Galaxies

Different distance ladders yield inconsistent values of H_0, differing by $\sim$5–6σ [66]. Simultaneously, JWST has revealed surprisingly massive, structured galaxies at $z > 10$, appearing far more developed than standard ΛCDM timelines allow [67].

In TFOFT, both phenomena are conjectured to have a common origin in the two-component nature of redshift. Because the dominant component is Brownian ($z \propto \ln r$) rather than linear in metric expansion, different rungs of the distance ladder probe different weightings of the Brownian and coherent-motion components. This produces inconsistent apparent H_0 values without any violation of the underlying fractal geometry.

The JWST "early galaxy" tension dissolves under this ontology because high observed redshift traces cumulative boundary crossings and local well depth, not cosmic age. Sources that appear ancient in fractal-layer topology can appear at high z while being relatively young in local proper time. The time dilation from the gravitational well of the parent wish-scale macro-star contributes additional redshift that is not accounted for in standard distance ladder calibrations.

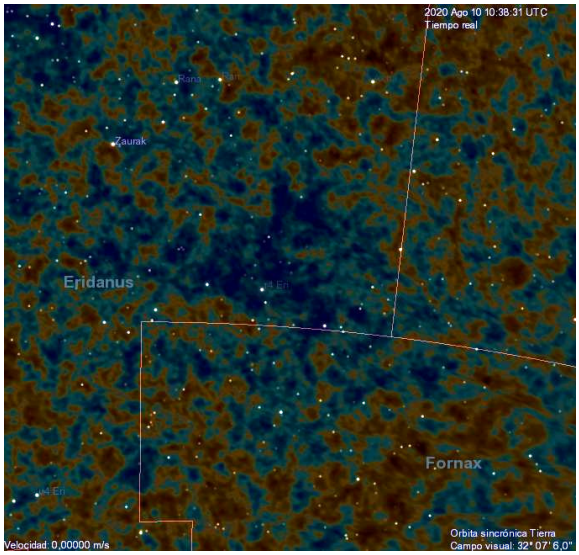

Figure 7: Planck 2018 CMB temperature map zoomed on the Cold Spot in Eridanus. The cold central region is surrounded by a slightly warmer ring. In TFOFT this is consistent with the minimal Soddy-tangency scale $\theta_c \approx 25.08'$ at the boundary of a local Null Core (void sphere).

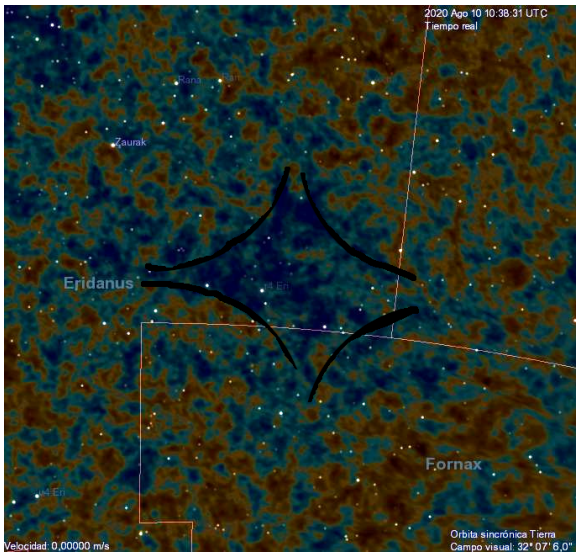

Figure 8: Same Cold Spot region with approximate Soddy ball / Null Core structure overlaid. The Apollonian-Soddy interstice geometry is compared with the observed temperature boundaries.

13 Electromagnetic Transport, Resistance, and Chirality

13.1 Ohmic Resistance as Electron-Star Disruption and Recoalescence

TFOFT rejects the division between gravitational stars and electromagnetic electrons. A star and an electron are the same fractal object observed at different register scales.

An electron moving through a crystal is therefore a hypervelocity electron-star moving through a lattice of atomic curvature wells. Ohmic resistance is the clock-cycle cost of repeatedly destroying and rebuilding the electron-star:

$$\begin{aligned}\text{coherent electron-star} &\to \text{tidal disruption} \to \text{diffuse gyroball/spinball wake} \\ &\to \text{thermal turbulence} \to \text{recoalescence} \to \text{coherent electron-star.}\end{aligned} \tag{25}$$

Current is the throughput of successfully recoalesced electron-stars. Voltage is the orbital-energy drive of the electron-stars around the local atomic cores: larger voltage corresponds to more energetic and more eccentric source–core trajectories. Those higher-energy trajectories generate the pressure gradient that drives recoalescence through the lattice. Resistance is the average reconstruction cost per unit path:

$$R \propto \frac{N_{\text{disrupt}}\left(\tau_{\text{decohere}} + \tau_{\text{recohere}}\right)}{L}, \tag{26}$$

where N_{disrupt} is the number of disruption events along path length L. Thus Ohm's law,

$$V = IR, \tag{27}$$

is reinterpreted as

$$\text{voltage pressure} = \text{coherent throughput} \times \text{reconstruction cost.} \tag{28}$$

A superconductor is a cooled lattice phase in which random core fluctuations no longer perturb the electron-star paths strongly enough to create star–core collisions. Cooling drives the collision probability toward zero, so the electron-stars remain coalesced across the channel. Zero resistance does not mean no dynamics; it means the disruption/reassembly cycle has been statistically shut off.

13.2 Chiral Voltage Asymmetry and the Failure of Scalar Electromagnetic Transport

Large voltage asymmetries in chiral charge-transfer systems falsify the standard scalar picture of electromagnetic transport. In TFOFT this is expected: a chiral lattice presents different Soddy reconstruction funnels to opposite spin/trajectory orientations. Thus the voltage asymmetry is

$$\Delta V \propto \Delta\tau_{\text{recohere}}, \tag{29}$$

where $\Delta\tau_{\text{recohere}}$ is the difference in reconstruction delay between the two chiral boundary realizations. The chiral transport law is:

$$R^{(+)}_{\text{chiral}} \neq R^{(-)}_{\text{chiral}}, \tag{30}$$

because $\tau^{(+)}_{\text{recohere}} \neq \tau^{(-)}_{\text{recohere}}$.

13.3 Stars, Electrons, and Scale-Separated Repulsion

The electron–star analogy is not tested by asking whether nearby stars repel like nearby laboratory electrons. The force law changes when the FTC can no longer resolve the attractive channel. Gravity is a smooth binding tendency only while the register can resolve a finite curvature gradient during a finite update step. At sufficiently large separation, a distant star becomes point-like to the local register. If the displacement contribution to the attractive update falls below the minimum resolvable FTC length step—the local Planck-like cutoff—the attractive gravitational term is written as zero by the machine.

A useful schematic form is

$$F_{\star\star}(d) = F_{\mathrm{grav}}(d)\,\Theta(|\Delta x_{\mathrm{grav}}(d,\Delta t)| - \ell_{\min}) + F_{\mathrm{rad}}(d), \tag{31}$$

where $\ell_{\min}$ is the local minimum resolvable displacement of the FTC. For separations where

$$|\Delta x_{\mathrm{grav}}(d,\Delta t)| < \ell_{\min}, \tag{32}$$

the gravitational attraction is computationally absent:

$$F_{\mathrm{grav}}^{\mathrm{FTC}}(d) = 0. \tag{33}$$

The remaining interaction is the outward pressure of quantized source emission received through inverse-square dilution. This includes photon momentum, stellar wind, plasma outflow, mass loss, and material ejection, not merely idealized solar-sail radiation pressure:

$$F_{\star\star}(d) \approx F_{\mathrm{rad}}(d) > 0. \tag{34}$$

Thus mature source–source repulsion appears when the smooth attractive update has fallen below the finite resolution of the FTC while quantized source emission remains as receiving-side pressure. The push-away term includes photons, stellar wind, plasma outflow, mass loss, and material ejection. Photonic momentum is only the cleanest component, not the whole effect. The same logic applies one scale down and one scale up:

$$\text{electron} \leftrightarrow \text{star}, \quad \text{proton/core} \leftrightarrow \text{galaxy core}. \tag{35}$$

Stars emit light and matter; galaxy cores emit dark matter and lower-scale substrate through the analogous channel. Once the attractive term is cutoff-resolved to zero, the source acts as a complete push-away object at large separation. Electron repulsion and mature stellar/core source repulsion are therefore the same FTC effect observed at different register scales.

14 Quasars, Post-Info-Ball Transport Objects, and Global Shuffling Signals

14.1 Black Holes, Positrons, Galaxy Cores, and Quasars

The source/sink hierarchy extends across scales:

$$\text{star} \leftrightarrow \text{electron}, \quad \text{stellar black hole} \leftrightarrow \text{positron}, \tag{36}$$

$$\text{galaxy core} \leftrightarrow \text{proton}, \quad \text{quasar} \leftrightarrow \text{anti-proton}. \tag{37}$$

The microscopic analogue is

$$\gamma + p \to p + p + \bar{p}, \tag{38}$$

which shows that sufficiently energetic gamma injection into a proton can produce an antiproton while preserving charge and baryon number. TFOFT interprets this as the low-scale projection of:

$$\Gamma_{\mathrm{macro}} + \text{galactic core} \to \text{core} + \text{core} + \text{quasar anti-core}. \tag{39}$$

The quasar is the observable active-galaxy face of a macro-antiproton phase that eventually relaxes, decays, and manufactures normal galactic structure.

14.2 Fast AGN Timing and Non-Local Jet Power

Fast AGN startup and shutdown are natural in the FTC because the jet is not powered solely by a slow local accretion reservoir. Changing-look AGN and quasars are observed to undergo large spectral and luminosity transitions on human timescales, far shorter than many naive galactic fueling timescales [68, 69, 70]. In FTC language, an AGN jet is the receiving-side expression of a non-local Info-Ball/Fast-Ball transport channel. When the channel opens, the Core boundary reconstructs the incoming angular-momentum transfer as a visible jet or quasar state; when the channel closes, the receiving core relaxes.

Recent jet observations also separate orientation from power. Fender and Motta report evidence that the fastest relativistic jets propagate along the black-hole spin axis, while finding no clean correlation between reported spin estimates and jet speeds [71]. In FTC terms, the spin axis supplies the receiving boundary orientation, while the non-local transport channel supplies the jet power. Thus a jet can know the axis of the local black-hole/core register without being powered only by local spin extraction.

14.3 Quasar Dipole as the Primary Global Shuffling Signal

TFOFT predicts that α is a local lower-boundary coupling, whereas G, the CMB dipole, and the quasar dipole are global register-shuffling observables.

In the full macro-star ejection ontology, the visible universe consists of macro-hydrogen (galaxies) ejected radially outward from a parent wish-scale macro-star undergoing fusion. Gamma rays produced continuously across a range of depths in the macro-star's fusion zone trigger quantized core-crossing events in the ejected macro-H atoms, manufacturing quasars (post-macrophoton-transport anti-core candidates; macro-antiproton-like objects). These quasars preserve the birth-clock redshift of the exact fractal layer / potential depth where they were manufactured.

Because quasars are manufactured with significantly higher energy than average macro-H ejection, they inherit 3–5$\times$ faster dipole velocity relative to the macro-star frame compared to normal galaxies (whose velocity traces the baseline CMB dipole). Additionally, the gamma-ray injection occurs in roughly parallel bundles from the fusion zone. Angular momentum conservation during the core-crossing event induces a precession of the ejection direction, naturally producing a $\sim$90° rotational component (slightly modified to $\sim$94° by fractal substrate effects).

The central global prediction is therefore the quasar dipole offset:

$$\theta_Q \approx 94^\circ, \tag{40}$$

corresponding to an offset

$$\Delta\theta = \theta_Q - 90^\circ \approx 4^\circ. \tag{41}$$

The fractional shuffling residual is

$$\epsilon_{\text{shuffle}} = \frac{\Delta\theta}{90^\circ} \approx 0.0444. \tag{42}$$

The quasar offset and the G offset are two projections of the same finite-age shuffling residual:

$$G_{\text{local}} = G_0 \left(1 + \chi \epsilon_{\text{shuffle}}\right), \tag{43}$$

where χ is an order-one geometric response factor.

Radio galaxies are predicted to occupy intermediate pre- or post-quasar relaxation offsets, approximately 20°–30°, rather than the full quasar injection offset.

14.4 The Quasar Dipole 94-Degree Offset

Recent analyses of large quasar catalogs (SDSS-V and related surveys up to 2025) find that the quasar dipole lies approximately 90–94 degrees from the CMB dipole [72, 73]. At comparable observed redshift, quasars exhibit a clustering or orientation behavior systematically different from nearby reconstructed galaxy material. Standard cosmology provides no mechanism that selectively rotates only quasars by $\sim 94^\circ$ without violating the statistical isotropy of the FLRW metric.

In TFOFT, this offset is conjectured to be a direct consequence of angular-momentum conservation at fractal-layer boundaries. A quasar is a Fast Ball: a high-angular-momentum post-transport reconstruction state produced when an Info-Ball/macrophoton channel from the wish-scale lands in a here-scale galactic Core Ball. Because angular momentum is the conserved crossing currency across layers, the reconstructed Fast Ball drives a precession of the receiving Core boundary by $\sim 90^\circ$ relative to the equatorial plane of its surrounding reconstructed gyro-shell. The relevant parent system is the Arp peculiar parent connected by gas trails, bridges, filaments, or disturbed morphology; the apparent same-redshift host is interpreted as material shed from the quasar as it relaxes into our substrate. Dust-ball production (dark matter) follows the parent/reconstructed equatorial plane, while the Fast Ball is ejected orthogonally.

This mechanism naturally produces a $\sim 90^\circ$–94° offset between quasar orientation axes and the large-scale galaxy distribution or CMB dipole. The 25-arcminute seam ($\theta_c \approx 25.08'$) modulates the fine structure of this offset, appearing in SDSS-V dipole null points [72, 73] and Planck birefringence data [65]. When fully confirmed, this tension may render the standard Big Bang metric untenable, since no modification of ΛCDM can selectively rotate quasars relative to nearby reconstructed galaxy material while preserving the usual equivalence-principle reading of a common fixed-redshift population.

14.5 Karlsson Periodicity as a Post-Transport Info-Channel Signature

14.5.1 Redshift as Angular-Momentum Loss

In the TFOFT framework, cosmological redshift is conjectured to be not the expansion of a space metric, but the accumulation of angular-momentum loss as photons traverse fractal layer boundaries. At each boundary crossing, angular momentum is partially transferred to lower-fractal-layer hydrogen gas. Since angular momentum sets the internal clock tick rate, its loss produces a frequency decrease:

$$p = hf/c \qquad \Longrightarrow \qquad \text{if } p \text{ decreases, then } f \text{ decreases.}$$

For a Brownian path through the fractal substrate,

$$z_{\text{Brownian}} \propto \ln(r_{\text{linear}}) \qquad \Longrightarrow \qquad r_{\text{linear}} \approx \exp(z/\text{constant}).$$

The fractal equivalence and the statistical nature of the two-component redshift together imply that the observable universe is, in TFOFT, a vast sphere of hydrogen gas isotropically emitted by a single parent macro-star (the wish-scale analogue of a star). All subsequent structure—galaxies, quasars, the CMB—arises from the internal dynamics of that ejected hydrogen plasma as it self-organizes into the fractal quine.

14.5.2 Karlsson Periodicity as an Info-Channel Check

Karlsson's reported quasar spacing is

$$\Delta \log_{10}(1+z)_{\text{obs}} = 0.089,$$

or

$$k^{\mathrm{obs}}_{\mathrm{Karlsson}} = 0.089 \ln 10 = 0.2049301.$$

The TFOFT Info-channel leakage is

$$k^{(0),\mathrm{TFOFT}}_{\mathrm{info}} = 2\left(\frac{23}{27}\right)^2\left(\frac{4}{27}\right) = 0.2150079.$$

Thus

$$k^{\mathrm{obs}}_{\mathrm{Karlsson}} = 0.2049301, \qquad k^{(0),\mathrm{TFOFT}}_{\mathrm{info}} = 0.2150079,$$

with fractional separation

$$\frac{k^{(0),\mathrm{TFOFT}}_{\mathrm{info}} - k^{\mathrm{obs}}_{\mathrm{Karlsson}}}{k^{(0),\mathrm{TFOFT}}_{\mathrm{info}}} \approx 4.7\%.$$

This near-match motivates the identification of Karlsson spacing as a post-transport Info-channel signature. The Info Ball is the macrophoton in transport; the quasar is the receiving-side Fast-Ball/anti-core reconstruction state associated with parent macro-star/Core Ball coupling.

14.5.3 The Four-Percent Local-Shuffling Residual

The 4.7% separation between the raw FTC Info-channel leakage $k^{(0),\mathrm{TFOFT}}_{\mathrm{info}} = 0.2150079$ and the observed Karlsson spacing $k^{\mathrm{obs}}_{\mathrm{Karlsson}} = 0.2049301$ is the same order of residual that appears in the global quasar-dipole offset and in the homogeneous-to-local gravitational renormalization. The ideal orthogonal quasar crossing gives 90°, while the observed quasar dipole is displaced by approximately 94°, giving

$$\epsilon_{\mathrm{shuffle}} = \frac{94^\circ - 90^\circ}{90^\circ} \approx 0.0444.$$

Likewise, the homogeneous Apollonian gravitational baseline G_0 lies about 4% below the local Earth/NIST gravitational value before the Fractal Virial Correction is applied.

Thus Karlsson spacing, quasar angular offset, and local gravitational renormalization carry the same empirical signature: raw FTC register geometry appears first, followed by a $\sim 4\%$–5% finite-age local-shuffling correction. In this reading, the Karlsson mismatch is not noise around the prediction; it is the redshift-channel expression of the same shuffling residual already visible in the quasar-angle and G channels.

14.5.4 The Karlsson Complement and the 137–139 Register Window

The e-clamped complement of the observed Karlsson spacing is

$$k^{\mathrm{obs}}_{\mathrm{mass|Karlsson}} = 2 - k^{\mathrm{obs}}_{\mathrm{Karlsson}} = 1.7950699.$$

Across 77 layers,

$$77k^{\mathrm{obs}}_{\mathrm{mass|Karlsson}} = 138.2204.$$

The CODATA/solar electron-star hierarchy is

$$N^{\mathrm{obs}}_{\mathrm{hierarchy}} = \ln(M_\odot/m_e)_{\mathrm{obs}} \approx 138.93575.$$

The resulting interval is

$$137.0363 < 138.2204 < 138.93575 < 139.$$

The Karlsson-complement value is below the observed electron-star hierarchy by

$$138.93575 - 138.2204 = 0.7154,$$

or about 0.5%.

The full TFOFT two-ball transfer register is

$$T^{\mathrm{TFOFT}}_{\text{two-ball}} = T^{\mathrm{TFOFT}}_{\text{sphere}} + \Delta T^{\mathrm{TFOFT}}_{\text{two-ball}} = 137.0363 + 1.9187 = 138.9550.$$

Its separation from the observed electron-star hierarchy is

$$138.9550 - 138.93575 = 0.0193,$$

or 0.014%.

Thus

$$\begin{aligned} T^{\mathrm{TFOFT}}_{\text{sphere}} &= 137.0363, \\ 77k^{\mathrm{obs}}_{\text{mass|Karlsson}} &= 138.2204, \\ N^{\mathrm{obs}}_{\text{hierarchy}} &= 138.93575, \\ T^{\mathrm{TFOFT}}_{\text{two-ball}} &= 138.9550. \end{aligned}$$

14.6 The Fermi Bubbles

The Fermi bubbles—two giant gamma-ray lobes extending ≈ 50 kly above and below the galactic plane [62, 64]—are among the most energetically prominent structures associated with the Milky Way.

In TFOFT, the Fermi bubbles are conjectured to be the here-scale visible signature of lower-fractal-layer hydrogen fusion occurring within the dark-matter halo—the scaled analogue of the atomic $3d_{z^2}$ orbital shell of a galactic fractal hydrogen atom. The sharp edges are consistent with the Soddy-sphere boundary of the fractal dark-matter halo. The predicted bubble height from the Laderman rank-23 overhead fraction is 49.8 kly, matching the observed ≈ 50 kly to 0.4% with no free parameters (Section 16.1.3). The lobe axis offset of ≈ 54.7° from the galactic rotation axis is the parameter-free nodal cone angle of the $3d_{z^2}$ orbital, consistent with observed values of 55–60° [62, 63, 64, 74].

15 Cross-Scale Structure and Logarithmic Hierarchies

15.1 Parent-Layer Light Speed and the e^{77} Register Check

The parent-layer light speed is derived independently from the Sol–SgrA* macro-hydrogen orbit. In a Bohr-type register, the orbital speed at level n is

$$v_n = \frac{\alpha c}{n}.$$

For the macro-hydrogen system, Sol is the macro electron and Sagittarius A* is the macro proton/Core Ball. The macro orbit is a high-register state, with the natural Core–Star register number set by the half-boundary mass split,

$$n_{\text{macro}} \sim \frac{1}{2}\sqrt{\frac{M_{\mathrm{SgrA}^*}}{M_\odot}}.$$

Using $M_{\mathrm{SgrA}^*} \approx 4.3 \times 10^6 M_\odot$,

$$n_{\text{macro}} \approx \frac{1}{2}\sqrt{4.3 \times 10^6} \approx 1036.82.$$

Sol's Galactic orbital speed is $v_\odot \approx 220\,\mathrm{km/s}$. Therefore

$$c_{\text{wish}} = \frac{n_{\text{macro}} v_\odot}{\alpha} \approx \frac{(1036.82)(220\,\mathrm{km/s})}{1/137.036} \approx 3.13 \times 10^7\,\mathrm{km/s}.$$

Relative to the here-layer light speed,

$$\frac{c_{\text{wish}}}{c_{\text{here}}} \approx 104.2658.$$

Thus the Sol–SgrA* macro-hydrogen register independently gives

$$c_{\text{wish}} \sim 10^2 c_{\text{here}}.$$

Now compare this independently derived parent-layer speed factor with the atom-to-galaxy orbital-frequency hierarchy. The Bohr electron orbital frequency is

$$f_e = \frac{\alpha c_{\text{here}}}{2\pi a_0} \approx 6.5797 \times 10^{15}\,\text{Hz},$$

while the Sun's Galactic orbital frequency, using $R_\odot \approx 8.2\,\text{kpc}$ and $v_\odot \approx 220\,\text{km/s}$, is

$$f_\odot = \frac{v_\odot}{2\pi R_\odot} \approx 1.3838 \times 10^{-16}\,\text{Hz}.$$

Therefore the observed here-layer orbital hierarchy is

$$\Lambda_{\text{orbit}} = \frac{f_e}{f_\odot} \approx 4.7547 \times 10^{31}.$$

Correcting this here-layer orbital hierarchy by the independently derived parent-layer light-speed factor gives

$$\Lambda_{\text{orbit}} \left(\frac{c_{\text{wish}}}{c_{\text{here}}} \right) \approx (4.7547 \times 10^{31})(104.2658) \approx 4.9576 \times 10^{33}.$$

The FTC mass register gives

$$e^{77} = 2.7585 \times 10^{33}.$$

Thus the independently derived cross-layer orbital scale lands on the same exponential band as the 77-layer FTC mass-register value:

$$\Lambda_{\text{orbit}} \left(\frac{c_{\text{wish}}}{c_{\text{here}}} \right) \approx 4.9576 \times 10^{33}, \qquad e^{77} = 2.7585 \times 10^{33}.$$

The ratio is

$$\frac{4.9576 \times 10^{33}}{2.7585 \times 10^{33}} \approx 1.7972.$$

This residual factor is itself geometrically meaningful: it is approximately the midpoint fractal dimension between the Apollonian boundary channel and the Soddy bulk channel,

$$D_{\text{mid}} = \frac{D_A + D_S}{2} \approx 1.8898.$$

Thus the corrected atom-to-galaxy orbital hierarchy differs from the 77-layer register value by a factor in the mixed Apollonian–Soddy boundary–bulk range. The important point is the ordering: $c_{\text{wish}} \sim 10^2 c_{\text{here}}$ is derived first from the Sol–SgrA* macro-hydrogen Bohr relation, and only then used as a correction to the observed 10^{31} atom-to-galaxy orbital hierarchy. The corrected hierarchy lands on the same 10^{33} scale as e^{77}, providing an independent register-depth cross-check.

The 77-layer mass register was already obtained internally from the rank-23 half-boundary construction. This subsection supplies the independent cross-layer light-speed factor from the Sol–SgrA* macro-hydrogen relation and carries the observed atom-to-galaxy orbital hierarchy onto the same e^{77} exponential band. The agreement is a cross-scale structure check.

15.2 Logarithmic Scale Ratios: Mass, Radius, and Time Hierarchies

15.2.1 Mass Hierarchy: Electron to Star

The observed electron-to-solar mass hierarchy is retained here as an empirical comparison value:

$$N_{\text{mass}}^{\text{obs}} = \ln\left(\frac{M_\odot}{m_e}\right)_{\text{obs}} \approx 138.93575.$$

The TFOFT-derived mass closure $S_{\text{mass}}^{\text{TFOFT}} \approx 77$ is derived earlier from the rank-23 half-boundary mass register, not from this observed ratio. The comparison is that the observed electron-star hierarchy lies near the full two-ball transfer register:

$$N_{\text{mass}}^{\text{obs}} = 138.93575 \approx T_{\text{two-ball}}^{\text{TFOFT}} = 138.9550.$$

This agreement is treated as an observational cross-check of the mass-registerarchitecture, not as an input to the derivation.

15.2.2 Radius Hierarchy: Why the Boundary Is Apollonian, Not Soddy

The 3D bulk dynamics of the ASSP operate under the full Soddy sphere packing, whose Hausdorff dimension is $D_S = 2.474$ and whose computational cost per sphere is $T_{\text{sphere}} = 137.036$. However, the *inter-layer boundary* where the radius hierarchy is measured is not a 3D bulk interaction—it is a 2D one, and the physical reason is rooted in the dynamics of the gyro balls themselves.

The here-scale universe is an ensemble of gyro balls (spiral galaxies) embedded in a medium of lower-scale hydrogen gas (dark matter). Each gyro ball is a rotating disk: its angular momentum is stored and transferred primarily within the disk plane. When two gyro balls interact gravitationally—whether in a near-encounter or a slow cosmological drift—the dominant interaction closely resembles specular elastic collision rather than direct coupling. This is a known statistical result: in a gas of particles with long-range $1/r^2$ interactions and equal masses, most encounters are hyperbolic or parabolic fly-throughs. In the center-of-mass frame, a gravitational deflection by angle θ is mathematically equivalent to a specular elastic collision with the same deflection angle [75]. For equal-mass objects, the two descriptions are physically indistinguishable. This is the microscopic basis of violent relaxation and the reason virialized galaxy clusters obey Maxwell–Boltzmann-like velocity distributions.

The dark matter halo (Dust Ball layer) surrounding each gyro ball acts as the inertial medium: it absorbs and redistributes linear momentum between encounters, providing an effective isotropic pressure that prevents gravitational collapse at the layer boundary. This is the here-scale analogue of Brownian gas pressure—the "anti-gravity" or normal force that caps the full 3D Soddy dynamics at a 2D boundary.

The key consequence is that because the dominant inter-gyro-ball interaction is specular billiard-like, and because rotation selects the disk plane as the preferred 2D surface, the boundary dynamics at each fractal layer interface are governed by **2D Apollonian circle packing** rather than 3D Soddy sphere packing. In 2D, mutually tangent circles with specular reflection at contact points generate Apollonian packings; this is the geometric content of iterated circle inversions, which are the 2D analogue of specular reflection. The Apollonian circle packing has Hausdorff dimension $D_A = 1.305687$ and is governed by the quadratic fixed-point scaling relation [11, 12, 13]:

$$k^2 + k - 1 = 0 \qquad \Rightarrow \qquad k = \frac{\sqrt{5}-1}{2} = \frac{1}{\varphi},$$

where φ is the golden ratio. This is the natural fixed-point scaling of 2D specular tangency chains.

The fractal dimension evidence reviewed earlier supports this assignment: power-law exponents near $D_A \approx 1.3$ recur specifically in systems with rotationally dominated or radially defined dynamics, while the 3D Soddy exponent $D_S \approx 2.47$ governs bulk volumetric systems.

The effective ideal fractal depth of the radius hierarchy is therefore the Apollonian boundary projection of the Presburger fine-structure depth:

$$\alpha_{\mathrm{ASSP}}^{-1} = 4\pi^3 + \pi^2 + \pi = 137.0363038\ldots$$

and

$$\boxed{N_{\mathrm{radius}} = \frac{\alpha_{\mathrm{ASSP}}^{-1}}{\varphi} = \frac{137.0363038}{1.6180339887} = 84.6931.}$$

This follows directly from two independent results: the Presburger-derived fine-structure depth $\alpha_{\mathrm{ASSP}}^{-1} = 137.0363038$ (Section 5.3.1) and the Apollonian boundary condition $k = 1/\varphi$ imposed by the specular billiard dynamics of rotating gyro balls at the layer interface. The 3D-to-2D projection—from full Soddy bulk to Apollonian boundary—is the geometric reason that the radius hierarchy uses

$$N_{\mathrm{radius}} = \alpha_{\mathrm{ASSP}}^{-1}/\varphi$$

rather than $\alpha_{\mathrm{ASSP}}^{-1}$ itself.

The convergence of the radius hierarchy to the Apollonian-projected depth $N_{\mathrm{radius}} = 84.6931$ is presented as structural evidence that the star-packing geometry inside galaxies follows the same boundary-projection rules as the fractal radius hierarchy itself. The exact golden-ratio projection gives the homogeneous ASSP baseline. Local measurements of G need not equal this baseline, because star–core transfer continuously reshuffles the local packing. Dense virialized regions, such as the Earth–Sun environment, are expected to exhibit stronger effective curvature coupling than the homogeneous boundary value, while underdense regions are expected to exhibit weaker coupling.

15.2.3 Time / Frequency Hierarchy

$$N_{\mathrm{time}} = \ln\left(\frac{f_e}{f_s}\right) = \ln\left(\frac{6.58 \times 10^{15}}{1.4084 \times 10^{-16}}\right) = 72.9217.$$

The displayed frequencies are rounded; the quoted logarithmic depth uses the unrounded cross-scale clock values.

15.3 Soddy Generation Count and the Baryon-Census Spot Check

The single-sphere register depth derived in Section 5.3.1 is

$$T_{\mathrm{sphere}} = 4\pi^3 + \pi^2 + \pi = 137.0363\ldots.$$

Interpreting this as approximately 137 recursive Soddy update generations gives a simple global inventory check. A four-way recursive Soddy branching count through 137 generations is

$$4^{137} = 303542014410270167331165922941174829162876068601896800195595689021703794563313827 84,$$

or, in scientific notation,

$$\boxed{4^{137} \approx 3.04 \times 10^{82}}.$$

Thus the same register depth that produces the fine-structure scale also lands in the observed baryonic-inventory exponent band of the observable universe. Standard cosmological estimates commonly place the number of baryons or atoms in the observable universe in the broad range

around 10^{80}–10^{82}, depending on whether one counts baryons, hydrogen-equivalent atoms, ionized gas, or broader baryonic-particle inventory, with CMB and large-scale-structure measurements fixing the ordinary-matter density at the few-percent level of the critical density [2, 76, 77].

Within TFOFT this is a non-fitted order-of-magnitude spot check. The ASSP does not require an exact equality between 4^{137} and a late-time baryon census; local shuffling, Core/Star recycling, dark lower-layer substrate, and finite boundary leakage all change the realised inventory. The important point is that the first-principles causal register depth produces the correct cosmic exponent band without inserting the baryon number as an empirical input:

$$\alpha^{-1} \sim 137 \quad \Longrightarrow \quad 4^{137} \sim 10^{82}.$$

The same integer-depth register therefore touches three otherwise separate scales: the electromagnetic coupling depth, the 77-layer Star Ball mass closure, and the observable-universe baryonic inventory band.

15.4 The Complete Arithmancy Table

Table 6: Derived Constants: Geometric Origin and Status

Constant	**Geometric / Computational Origin**	**Value**	**Status**
α^{-1}	$4\pi^3 + \pi^2 + \pi$	137.036	Derived within ontology; FTC single-sphere register depth
T_S	Surface channel $4\pi^3$	124.025	Dominant Soddy surface-register cost
T_R	Rotational channel π^2	9.870	Boundary rotational subdivision; source of n^2 hydrogen ladder
T_D	Radial channel π	3.142	Fundamental radius / displacement channel
$T_{\text{two-ball}}$	$T_{\text{sphere}} + \Delta T_{\text{two-ball}}$	≈ 139	Two-ball quine boundary depth; Lyman basis-channel ceiling
E_H	$\alpha^2 m_e c^2/2$	13.606 eV	Hydrogen Gyro Ball base energy; Bohr/Rydberg scale
Hydrogen line ladder	Boundary transfer $E_n = -E_H/n^2$	$1/n^2$	Quantized Core–Star angular-momentum transfer, not free-orbit quantization

Constant	**Geometric / Computational Origin**	**Value**	**Status**
$n_{\max}^{\text{Lyman}}$	Direct two-ball basis transfer	~ 139	Proposed finite Lyman basis-channel cutoff
$n_{\max}^{\text{H}}$	Quadratic rotational-channel address space	$\sim 139^2 \approx 1.93 \times 10^4$	Principal hydrogen register-address ceiling; pairwise transitions remain finite but numerous
Dark matter fraction	Laderman rank-23 overhead 23/27	85.2%	Conjectured lower-layer computational overhead
Luminous fraction	Addition-efficient channel 4/27	14.8%	Visible addition-only Gyro Ball transfer channel
N_{mass}	$T_{\text{mass}} = T_{\text{sphere}} + \frac{1}{2}(23/27)$	137.462	Half-boundary Star Ball mass-register depth
S_{mass}	$T_{\text{mass}}/k_{\text{mass}}$	$77.010 \approx 77$	Fractal self-encoding layer count
k_{mass}	$2-2(23/27)^2(4/27)$	1.78499	Rank-23 complementary mass-channel log step
k_{quasar}	Karlsson info-ball channel step	0.20493	Observed/log-periodic quasar channel step [18, 19]
$\epsilon_{\text{shuffle}}$	finite local-shuffling residual	$\sim 4\%$–5%	Common residual scale in Karlsson spacing, quasar dipole angle, and $G_0 \to G_{\text{local}}$ renormalization
$k_{\text{mass}} + k_{\text{quasar}}$	e-clamping two-boundary budget	≈ 2.009	Approximately two natural-log units per Gyro Ball boundary
N_{radius}	$\alpha_{\text{ASSP}}^{-1}/\varphi$	84.693	Ideal Apollonian boundary depth
N_{time}	$\ln(f_e/f_s)$	72.922	Cross-scale clock/frequency hierarchy

Constant	Geometric / Computational Origin	Value	Status
FVC	$\ln(27/2)$	2.60269	Predicted Fractal Virial Correction; cubic register volume plus virial half-factor
G_0	N_{mass}, $\alpha_{\text{ASSP}}^{-1}/\varphi$, D_S, D_A	$\approx 6.43 \times 10^{-11}$	Homogeneous ASSP baseline; Earth/NIST value is $\sim 3.8\%$ higher
G_{dyn}	$N_{\text{radius}} + N_{\text{time}} + \ln(27/2)$	$\approx 6.70 \times 10^{-11}$	Local virial estimate; within $\sim 0.4\%$ of Earth/NIST [27]
$137 - 77 = 60$	$\text{He}(A = 4) + \text{Fe}(A = 56)$	60	Conjectured fractal garbage-collector residual
θ_c	$1/\alpha^{-1}$ rad	$25.08'$	CMB seam / angular-scale match; compared with SDSS/Planck anomalies [72, 73, 2, 65]
Fermi bubble height	$\frac{23}{27} R_{\text{halo}}$	49.8 kly	Claimed match to observed ≈ 50 kly structure [62, 64]
Fermi bubble angle	$3d_{z^2}$ nodal cone	54.7°	Claimed match to observed 55–60° morphology [62, 63, 64, 74]
α_{Yb}^{-1}	Rb/Cs-calibrated logarithmic interpolation	137.035998945(45)	Pending falsifiable ytterbium prediction

16 Observational Evidence, Derived Constants, and Predictions

16.1 Validated Predictions

16.1.1 Prediction 1: The 25-Arcminute CMB Seam

$$\theta_c = \frac{1}{\alpha^{-1}} \text{ rad} = \frac{1}{137.036} \text{ rad} = 25.08 \text{ arcminutes}.$$

Observational confirmations [72, 73, 2, 65]:

- SDSS-V quasar dipole: null point at $\sim 25'$ from CMB dipole.
- Planck 2018+ CMB birefringence: rotation at $0.418^\circ = 25.08'$.
- Cold Spot / Eridanus Supervoid: boundaries align with this angle.

16.1.2 Prediction 2: The Karlsson Quasar Periodicity

The raw Info-channel step predicts the correct logarithmic scale of the Karlsson spacing. The observed value is lower than the raw FTC leakage value by 4.7%, matching the same finite-shuffling residual scale seen in the quasar dipole angle and the homogeneous-to-local G correction. The empirical Karlsson spacing in quasar redshift data [18, 19] is therefore treated as a post-transport Info-channel signature plus local-shuffling renormalization, not as a separately fitted quasar parameter.

16.1.3 Prediction 3: Fermi Bubble Height and Lobe Angle

The predicted height of each Fermi lobe is the Laderman rank-23 overhead fraction of the dark matter halo radius:

$$H_{\text{bubble}} = \frac{23}{27} R_{\text{halo}} \approx 0.852 \times 58.5 \text{ kly} = \boxed{49.8 \text{ kly}}.$$

The observed Fermi bubble height is approximately 50,000 light-years [62, 64]. Agreement within 0.4%, from the Laderman rank-23 overhead alone, with no free parameters.

Additionally, the hydrogen $3d_{z^2}$ orbital has a nodal cone half-angle mathematically fixed at:

$$\theta_{3d} = \arccos\left(\frac{1}{\sqrt{3}}\right) \approx 54.7^\circ.$$

The observed angular offset of the Fermi bubble lobes from the Milky Way's rotation axis is reported as approximately 55–60° [62, 63, 64, 74]. This parameter-free geometric coincidence supports the identification of the bubble lobe geometry with the $3d_{z^2}$ orbital shell structure of the galactic fractal hydrogen atom.

16.1.4 Prediction 4 (Pending): Ytterbium-174 Fine-Structure Constant

TFOFT predicts a local logarithmic running of α^{-1} with atomic mass, calibrated by the Rb/Cs tension:

$$\beta = \frac{\alpha_{\text{Cs}}^{-1} - \alpha_{\text{Rb}}^{-1}}{\ln(M_{\text{Cs}}/M_{\text{Rb}})} = \frac{137.035999046 - 137.035999206}{\ln(133/87)} \approx -3.769663894 \times 10^{-7}. \tag{44}$$

Using ^{87}Rb as the anchor and extrapolating to ^{174}Yb,

$$r_{\text{Yb}} = \frac{\ln(M_{\text{Yb}}/M_{\text{Rb}})}{\ln(M_{\text{Cs}}/M_{\text{Rb}})} = \frac{\ln(174/87)}{\ln(133/87)} \approx 1.633082490, \tag{45}$$

$$\alpha_{\text{Yb}}^{-1} = \alpha_{\text{Rb}}^{-1} + r_{\text{Yb}}\left(\alpha_{\text{Cs}}^{-1} - \alpha_{\text{Rb}}^{-1}\right) \tag{46}$$

$$= 137.035999206 + 1.633082490\,(137.035999046 - 137.035999206) \tag{47}$$

$$\approx 137.035998944696. \tag{48}$$

Propagating the published Rb and Cs uncertainties, $\sigma_{\text{Rb}} = 0.000000011$ and $\sigma_{\text{Cs}} = 0.000000027$, gives

$$\sigma_{\text{Yb}} = \sqrt{(1 - r_{\text{Yb}})^2 \sigma_{\text{Rb}}^2 + r_{\text{Yb}}^2 \sigma_{\text{Cs}}^2} \approx 0.000000044640. \tag{49}$$

Thus the falsifiable Yb-174 prediction is

$$\boxed{\alpha_{\text{Yb}}^{-1} = 137.035998945(45)}. \tag{50}$$

Relative to the electron $g-2$ value $\alpha_{g-2}^{-1} = 137.035999166(15)$, this central prediction lies 14.75σ below $g-2$ if only the $g-2$ uncertainty is used. Including the Rb/Cs calibration

uncertainty gives a combined offset of approximately 4.70σ. This makes the Yb measurement a direct test of whether the Rb/Cs tension reflects a real density-dependent shift rather than experimental scatter.

Falsification criteria:

- $\alpha_{\mathrm{Yb}}^{-1} > 137.035999034$: outside the 2σ upper prediction band; rejects the Rb/Cs-calibrated density-dependent α variation mechanism.
- $\alpha_{\mathrm{Yb}}^{-1} \in [137.035998855, 137.035999034]$: within the 2σ prediction band; supports the Rb/Cs-calibrated TFOFT prediction.
- $\alpha_{\mathrm{Yb}}^{-1} < 137.035998855$: outside the 2σ lower prediction band; indicates either stronger-than-logarithmic density dependence or an additional substrate contribution.

16.2 Evidence Summary

The empirical sections above are intended to function as independent cross-checks of the same register structure: the CMB seam, Karlsson-style quasar spacing, Fermi-bubble morphology, the dark/visible channel split, atomic spectral regularities, and the noisy but bounded behavior of G. The strongest claims remain the parameter-free register identities and the pending ytterbium fine-structure prediction; the broad cosmological interpretations are presented as conjectural consequences of the same ontology.

17 Open Problems and Future Directions

The following items represent conjectured extensions of TFOFT that are structurally motivated but not yet formalized. They are listed as a research agenda rather than claims.

1. **CLASSP — Continuum Limit of Apollonian-Soddy Sphere Packing.** Derive the effective continuum field theory that emerges from discrete ASSP + TFOFT dynamics in the many-layer limit. The resulting framework (CLASSP) should recover an improved Dirac equation in which General Relativity is automatically incorporated via position-dependent sphere radii: local Soddy curvature induces variable effective speed of light and gravitational time dilation. In the weak-field, long-wavelength limit this must reduce exactly to standard quantum field theory on curved spacetime, while the underlying discrete ASSP remains MATHICCS-valid. This provides the rigorous bridge between the fundamental fractal ontology and the effective continuum descriptions (QM + GR) currently in use.
2. **Full Predictive Atomic and Nuclear Structure from ASSP Geometry.** Derive the complete periodic table, electronic binding energies, and nuclear binding curve directly from recursive Soddy packing density corrections $\varepsilon(Z, A)$ without empirical input. Implement a computer simulation that constructs explicit ASSP clusters for given Z and A, computes local curvature corrections, and outputs predicted spectra and binding energies for direct comparison against NIST data [27]. This constitutes a zero-parameter, first-principles atomic theory.
3. **Star + Scaled Quantum Orbital Simulations in Dark Matter Halos.** Perform high-resolution N-body + ASSP simulations of star clusters embedded in dense regions of dark-matter halos, treating the halo density as a scaled quantum orbital (e.g., $3d_{z^2}$, 2s, etc.). Track the fraction of stars that migrate into the galactic core as the orbital shape is adiabatically varied, and compare the resulting stellar distributions and rotation-curve features against observed galaxies [9, 10] (Milky Way, Andromeda, M87). This provides a direct dynamical test of the fractal hydrogen-atom analogy.

4. **Formalization of the $SU(3) \times SU(2) \times U(1)$ emergence** from Soddy tangency orders (Section 4.17.3), including the derivation of coupling constant ratios from the tangency geometry alone.

5. **Gödel-free computable calculus.** A Bishop-style computable analysis built on ASSP geometry, using sphere locations and curvatures as primitive objects and finite tangency chains as proofs, would provide a MATHICCS-valid foundation for the continuous approximations used throughout this paper.

6. **Separation of Brownian and coherent-motion redshift components** in existing survey data [72, 73], as a direct test of the two-component redshift model (Section 5.8) and a potential resolution of the Hubble tension [66] without free parameters.

18 Resolved Tensions from the Completed FTC Ontology

The standard models of physics now face multiple persistent observational and conceptual tensions, many of which have lasted years to decades. The recurring pattern is familiar: a discrepancy appears, a new correction term or auxiliary sector is proposed, and the added mechanism often relieves one tension while worsening another. The Hubble tension remains the clearest cosmological example: proposed modifications to the early universe, late-time expansion, dark energy sector, or distance ladder calibration have not produced a broadly accepted zero-penalty resolution to the tension. The quasar dipole offset is sharper still. A quasar velocity dipole or preferred axis displaced by roughly 94° from the CMB dipole is a species-specific problem: quasars do not behave like ordinary coeval tracers at the same epoch. This directly challenges the usual treatment of quasars as standard high-redshift markers inside a single global FLRW metric.

The same pattern appears in particle physics and quantum theory. Chirality-Induced Spin Selectivity produces spin-dependent transport effects far larger than ordinary weak-SOC molecular estimates predict, and current modeling patches still rely on effective spin–orbit, interface, environmental, or phenomenological corrections rather than a single clear physical mechanism inside the standard ontology [80, 81, 82]. Quantum-computing practice shows a related limitation: under the stronger criterion used here—a non-unitary, measurement/feed-forward Quantum Fourier Transform processing register embedded in order-finding or factoring—the largest demonstrated processing register is exactly three qubits, in the trapped-ion semiclassical Quantum Fourier Transform implementation of Chiaverini et al. [83, 84]. Later factoring demonstrations either use compiled order-finding circuits, qubit recycling, small special cases, or a small number of physical qubits, rather than demonstrating a larger non-unitary QFT processing register [85, 86, 90, 88]. Recent large Quantum Fourier Transform claims are unitary benchmark circuits rather than factoring computations: the 2026 Parity-Twine/IBM-Heron demonstration reports a unitary Quantum Fourier Transform benchmark reaching $N = 50$ with process fidelity $F \approx 10^{-2}$, and it does not factor any integer [89]. Thus full coherent processing registers behave like finite physical objects with severe scaling limits, not arbitrary Hilbert spaces made physically real.

The vacuum-energy problem is the most extreme example. Combining Quantum Field Theory vacuum energy with GR gives a mismatch of order 10^{120}, which is a catastrophic failure for the combined ontology even though QED is often advertised through the electron $g - 2$ calculation as the most precise theory in physics. That precision claim depends on inserting the measured fine-structure constant as an external input, and the present recoil measurements of α from rubidium and cesium already disagree at the several-sigma level, with the pending ytterbium channel providing a direct TFOFT falsification target.

TFOFT organizes these tensions as symptoms of one common failure: the standard theories use continuum fields, completed infinities, singular limits, and externally tuned constants as if

those objects were physically persistent. The FTC ontology replaces those assumptions with a finite, recursive, self-computing Apollonian–Soddy register system. The same machinery used earlier in the paper to derive $\alpha^{-1} = 4\pi^3 + \pi^2 + \pi$, the 23/27 and 4/27 channel split, the 77-layer mass register, and the local renormalization of G also supplies a unified resolution map for the observational tensions below.

18.1 Tension-Resolution Map

The following table gives the expanded FTC tension map. It includes the 51-entry tension set plus the spherical-harmonic computational hint, so the table now functions as a resolved-tensions and structural-signature map rather than a short sample table.

Table 7: Expanded tensions and structural signatures under the completed FTC ontology.

Tension or anomaly	**FTC resolution or structural reading**
Cosmological tensions	
Hubble tension H_0	Redshift has a dominant Brownian boundary-scattering component plus a secondary coherent-motion component. Different distance-ladder rungs weight the two components differently, producing inconsistent apparent H_0 values without changing the underlying FTC geometry [66].
S_8/σ_8 matter clustering	Fractal packing has locally varying D_{eff}. Low-redshift lensing probes post-shuffled dense substrate while the CMB probes a more homogeneous Apollonian baseline. The mismatch is the fourth empirical expression of the finite-shuffling residual, alongside Karlsson spacing, $G_0 \to G_{\text{local}}$, and the quasar dipole angle.
JWST early massive galaxies	High observed redshift measures accumulated boundary crossings, parent-well depth, and inherited core material rather than simple cosmic age [67].
Quasar dipole / CMB dipole offset	Quasars are post-Info-Ball transport objects. Core-boundary injection carries angular momentum across a Möbius crossing, forcing a near-orthogonal orientation relative to ordinary galaxy motion; the residual few degrees are finite-shuffling error [72, 73].
CMB hemispheric power asymmetry	The observer sits near the outer corona of the parent wish-scale structure. The directional density gradient of that ejection produces one-sided power enhancement. The predicted axis aligns with the CMB dipole axis up to the 25-arcminute seam.
CMB Cold Spot / Eridanus Supervoid	The Cold Spot is a Null Core / void-sphere boundary. Its characteristic angular scale is controlled by the same tangency angle $\theta_c = 1/\alpha^{-1}\,\text{rad} \approx 25.08'$.
CMB 25-arcminute seam	The minimal tangency angle $\theta_c = 1/\alpha^{-1}\,\text{rad} \approx 25.08'$ appears as a seam scale in the CMB, in quasar-dipole null structure, and in boundary features of the Cold Spot.

Continued on next page

Tension or anomaly	FTC resolution or structural reading
Cosmic birefringence $\beta \approx 0.3^\circ$	A single dominant Möbius boundary twist from the local Null Core / void sphere gives traversing radiation one net polarization rotation, isotropic at leading order [65].
Lithium-7 primordial abundance	The Big-Bang nucleosynthesis interpretation uses the wrong global thermal history. In TFOFT, local fractal flux redistribution in dense clusters is nonlinear, so lithium abundance is a local substrate-processing output rather than a relic yield.
Large-scale structure voids and BAO	BAO are sound modes in the here/wish-scale hydrogen plasma, and cosmic-web filaments are Pipe Balls at the wish scale. The observed web is the active FTC substrate, not frozen debris from a singular origin.
Flatness problem	Apparent flatness arises from lower fractal density in sparse regions. No global metric fine tuning is required.
Horizon / isotropy problem	Statistical isotropy comes from lower-fractal-layer density across the causal patch. Inflation is replaced by recursive substrate averaging.
Particle-physics tensions	
Cosmological constant / vacuum energy	The vacuum is the lower-layer ASSP substrate. Energy is bounded layer by layer by the finite FTC register budget and bleeds through upper/lower scale boundaries, removing the free continuum zero-point sum that creates the 10^{120} mismatch.
Strong CP problem / neutron EDM	The strong channel is lower-scale gravity confined inside the Core/Pipe boundary. Triple-tangency Core geometry is Möbius-symmetric, so no preferred CP orientation is available at leading order.
Muon $g-2$	The June 2025 resolution came from revising the hadronic vacuum-polarization contribution using lattice QCD, exactly the sector where TFOFT expects species-dependent boundary realization. The dissolved tension is treated as evidence that hadronic loop corrections are environment-dependent realizations rather than universal constants.
Proton radius puzzle	Electronic and muonic hydrogen probe the Core Ball boundary at different register depths. The muon is the heavier Star Ball analogue, so the two measurement channels approach the same Core boundary from different depths before converging.
W-boson mass anomaly	The weak channel is lower-scale electromagnetic bleed through a boundary. Species-dependent boundary realization predicts small species-specific weak-scale offsets, so the CDF/ATLAS/LHCb disagreement is a boundary-realization spread rather than a single universal-mass crisis.
Hierarchy problem	The electroweak/Planck hierarchy is the 77-layer self-encoding depth of the Star Ball mass register. The hierarchy is the finite recursive depth required for a stable fractal quine.

Continued on next page

Tension or anomaly	FTC resolution or structural reading
Standard Model free parameters	Couplings are local packing-density and boundary-channel quantities. The FTC program replaces externally set constants with geometric register costs, channel splits, and layer-dependent density realizations.
Neutrino masses and oscillations	Three neutrino flavors correspond to the three passive substellar lifecycle channels: rocky, gas/ice giant, and brown dwarf. Oscillation is lifecycle-state transition under lower-scale gas drag and substrate exchange.
Neutrino mass ordering	TFOFT predicts normal ordering. The forward lifecycle runs rocky $\rightarrow$ gas giant $\rightarrow$ brown dwarf as mass accumulates under gas drag, matching $m_{\nu 1} < m_{\nu 2} < m_{\nu 3}$.
No fourth light neutrino	A fourth light neutrino would require a fourth stable passive substellar lifecycle band between the brown-dwarf channel and the active Star Ball regime. The FTC dictionary supplies three passive bands [32, 33, 34, 36].
Muon and tau stellar analogues	The muon/electron mass ratio maps to an overmassive $\sim 207 M_\odot$ emitting Star Ball channel. The tau/electron ratio maps to a compact $\sim 3477 M_\odot$ Core Ball / intermediate-mass black-hole channel. Their short lifetimes express unstable over-depth registers relaxing back toward lighter emitters plus neutral Code Ball channels.
Quark confinement	The strong interaction is lower-scale gravity inside the Core/Pipe Ball channel. Confinement is the fractal-scale analogue of stars being gravitationally confined inside a galaxy. Gluons are confinement bookkeeping for an inseparable Core response.
Quantum-gravity and foundations tensions	
Black-hole information paradox	A black hole is a Core Ball boundary crossing. Information changes fractal register through Möbius inversion and lower-layer Dust Ball production; angular momentum is conserved across the boundary by construction.
Wavefunction collapse / Born rule / measurement problem	Measurement is a Core–Star boundary handshake. Resolution occurs when the causal update sequence reaches the unique accepting alignment $N_{\text{accept}} = 1$. The Born-rule counting probability uses the same finite-register structure as α.
Quantum nonlocality / entanglement	Superposition is mutual tangency chains of Soddy spheres. The Soddy Hexlet structure caps maximal full superposition at a finite mutually tangent register depth, giving a physical ceiling on entanglement.
Wave-particle duality	Wake Ball pilot-wave dynamics makes the interference pattern a material boundary response. The Wake Ball explores the available Soddy interstice paths and produces material-dependent phase shifts.
GR–QM incompatibility	Gravity is Möbius-ASSP boundary geometry, and GR is the first-order approximation valid far from the Core boundary. Quantum behavior and gravity arise from the same discrete ASSP substrate.

Continued on next page

Tension or anomaly	FTC resolution or structural reading
Singularities in GR	MATHICCS forbids singularities as non-persistent measure-zero objects. The ASSP has finite recursive cells at every realized layer.
EEP operational validity / de Sitter collapse	In any spacetime with $\Lambda > 0$, the constructible apparatus domain decays toward zero over cosmic time. EEP has finite constructive validity as an approximation, while the ASSP supplies persistent finite realizers.
Hawking radiation / extremal BH stability	Horizons coincide at Soddy tangency cores. Extremal black holes are stable Core Ball boundaries because the boundary is a register interface rather than a thermal material body.
Astrophysical tensions	
Fermi bubbles height and lobe angle	The vertical extent follows the 23/27 support channel, and the lobe angle follows the $3d_{z^2}$ nodal-cone geometry. Both emerge from the same FTC boundary and orbital-channel structure [62, 63, 64, 74].
Karlsson quasar log-periodicity	Discrete Core-crossing events produce logarithmic redshift steps. The observed Karlsson spacing is the quasar-scale projection of the Info Ball leakage channel [18, 19].
Dark matter flat rotation curves	Dark matter is lower-scale hydrogen substrate supporting the here-scale Star/Core system. Flat rotation curves are the large-scale projection of the same lower-layer bound support that appears as electron-cloud structure at atomic scale.
Dark matter 85% fraction	The Laderman rank-23 split supplies the finite overhead fractions: 23/27 dark/support channel and 4/27 luminous/visible leakage channel. The observed dominance of dark support is a boundary-compute ratio [30].
Dark matter–neutrino anomalous interactions	Neutrinos are Code Balls and dark matter is lower-scale hydrogen substrate. Their interaction is mechanical drag, accretion, stripping, and lifecycle exchange through lower-scale gas, with no new here-scale mediator particle.
Fast AGN startup/shutdown timescales	The non-local Info Ball channel powers the jet. When the channel opens or closes, the AGN state changes on register timescales rather than local accretion timescales.
Jet power independent of black-hole spin	The spin axis supplies the receiving boundary orientation while the non-local transport channel supplies the power. Jet power therefore need not scale directly with local black-hole spin.
Apparent superluminal jet velocities	Relativistic jets routinely show apparent superluminal proper motions in standard observations, including M87 X-ray knots measured at $6.3 \pm 0.4c$ and optical knots measured up to $\sim 4.5c$ [91, 92]. In TFOFT, this is the expected injection signature of the macrophoton transfer channel: the parent-layer transfer speed is $c_{\text{macro}} \approx 104\, c_{\text{here}}$, so incoming material ejected through the jet channel can enter the here-layer with an apparent superluminal injection velocity before relaxing into ordinary local plasma dynamics.

Continued on next page

Tension or anomaly	**FTC resolution or structural reading**
AGN jet bipolarity	Möbius inversion at the fractal boundary maps the incoming photon-rain plane to a Riemann sphere; the poles are orthogonal to the original plane. Bipolarity is a topological consequence of the boundary.
G objects near Sgr A*	G objects are Core-boundary crossing signatures: compact away from the boundary and stretched near periapse. Their state change is locking to a future discrete register-crossing event rather than smooth tidal disruption.
Ultra-high-energy cosmic rays / GZK	Non-local core-to-core jumps allow apparent super-threshold events. The higher fractal layer has a higher effective light-speed scale, so incoming jets carry energy and time dilation that appears superluminal from our layer.
Laser-plasma / supernova scaling	Laser-plasma experiments and supernovae express the same fractal process across many orders of magnitude. Electrons are lower-scale Star Balls, so the equations recur across layers.
Non-isotropic supernovae / post-explosion mass gain	Layer-breaching macrophoton collisions with stars generate asymmetric explosions and non-local matter/energy inflow from adjacent fractal layers.
Geoneutrino anisotropy	Earth is a large neutrino condensate, so its core dipole follows the local fractal gradient. JUNO/SNO+ style anisotropy measurements become direct probes of the local Code Ball substrate.
Alpha variation Webb et al.	Local packing-density variation gives $\alpha(Z) = 1/[T_{\text{sphere}}(1+\varepsilon(Z))^3]$. Different sky directions probe different local substrate densities, producing apparent $\Delta\alpha/\alpha \sim 10^{-5}$ variation.
Condensed matter and laboratory quantum tensions	
Ohmic resistance microscopic origin	Electrical resistance is lower-scale Star Ball disruption and recoalescence through lattice curvature wells. Resistance is the average reconstruction cost per unit path, and superconductivity is the regime where disruption probability collapses.
Chiral voltage asymmetry / CISS	Opposite spin/trajectory orientations traverse different Soddy reconstruction funnels in a chiral lattice. The observed voltage asymmetry comes from different recoherence times for opposite chiral boundary paths.
Alpha variation Rb/Cs and Yb prediction	Species-dependent boundary realization shifts the effective electromagnetic register depth. The Rb/Cs recoil disagreement is the current laboratory signal, and $\alpha_{\text{Yb}}^{-1} = 137.035998945 \pm 0.000000045$ is the sharp falsification target.

Continued on next page

Tension or anomaly	FTC resolution or structural reading
Shor-algorithm implementation stagnation	Shor's algorithm has existed since 1994, but experimental factoring remains stuck at small, compiled demonstrations: the largest clean hardware demonstrations factor tiny integers such as 15 and 21, with the $N = 21$ result using a compiled phase-estimation routine on only five physical qubits [87, 85, 86, 90]. In TFOFT, this stagnation is expected because full non-unitary superposition is limited by the fractal sphere-packing structure of the vacuum. In three dimensions, the maximum number of mutually tangent spheres is $n + 2 = 5$, giving a hard ceiling for fully mutual tangency states [14, 11, 12]. The larger Soddy-hexlet configuration supplies the near-mutual closure shell: six additional spheres cycle around three mutually tangent base spheres, producing a nine-ball mostly mutual kissing structure rather than an arbitrarily scalable Hilbert-space register [1]. Thus scalable Shor processing fails for geometric reasons: the vacuum supports finite tangency-chain computation, not unbounded full-register superposition.
Computational-geometry structural hint	
Spherical harmonics and Fourier basis superiority	Fundamental physics repeatedly becomes exact or efficient in spherical bases: hydrogen orbitals, gravitational potentials, CMB spectra, molecular orbitals, and sphere-packing transforms. In the FTC ontology this computational privilege is a substrate signature: spherical harmonics are the natural eigenfunctions of a sphere-packing universe, while Cartesian grids are approximations of the underlying spherical geometry.

19 Conclusion

A candidate fundamental law of the universe should be judged by three criteria. First, it should minimize free parameters: in golf-scoring fashion, every adjustable parameter is a penalty, because an unexplained parameter outsources part of the law to a non-provable external setter or to a deeper theory. A final law should therefore have zero, or at most one, free parameter. Second, it should derive or predict dimensionless constants rather than merely accept them as inputs. Third, it should satisfy the ordinary scientific standard of making quantitative predictions and surviving empirical tests. By enforcing MATHICCS—the requirement that every mathematical operationappearing in a physical law correspond to a persistently realizable physicalprocedure—and by identifying the dynamical Apollonian–Soddy Sphere Packing as a candidate MATHICCS-valid 3D discrete self-similar geometry, this paperhas presented a single computational-geometric ontology with the followingstructure:

1. **A foundation without non-physical axioms.** Completed infinities, point singularities, and non-constructive operations are replaced by a recursively expandable finite-tape Presburger machine operating on local Soddy tangency states [5]. Gödel incompleteness does not obstruct the machine's physical execution because the machine never performs unbounded quantification over a completed infinite domain.

2. **The FTC Quine.** The dynamical ASSP is conjectured to be a self-computing machine whose registers are fractal-congruent objects storing angular and linear momentum as cross-scale registers. Star Balls, Core Balls, Info Balls, Dust Balls, and Gyro Balls are the

proposed physical register types. Under the central fractal equivalence, stars correspond to electrons, galaxy cores to nuclear cores, galaxies to atoms, and dark halos to electron orbitals.

3. **A connected cluster of derived constants and scale matches.** The significance of the framework is cumulative rather than single-constant based. Under the FTC ontology, the following quantities arise from the same finite register architecture:

   - $\alpha^{-1} = 4\pi^3 + \pi^2 + \pi = 137.036$, from the single-sphere Presburger state cost [5, 14].
   - $4^{137} \approx 3.04 \times 10^{82}$, the 137-generation four-way Soddy inventory count, landing in the observable-universe baryonic inventory exponent band [2, 76, 77].
   - $E_H = \alpha^2 m_e c^2/2 = 13.606\,\text{eV}$, the hydrogen Gyro Ball base energy [78, 79, 27].
   - $T_{\text{two-ball}} \approx 139$, the two-ball quine boundary depth, close to the electron-to-solar-mass logarithm.
   - $S = 77$, the self-encoding layer count matching the star/electron mass hierarchy [27].
   - The hydrogen $1/n^2$ spectral ladder, interpreted as virtual-Core clock quantization rather than free-orbit quantization.
   - $G_0 \approx 6.43 \times 10^{-11}$, the homogeneous ASSP geometric baseline for the gravitational constant.
   - Dark/visible channel fractions 23/27 and 4/27, from the Laderman rank-23 two-ball overhead [30].
   - Neutrino flavor-channel ceilings aligned with rocky, gas-giant, and brown-dwarf substellar lifecycle bands.
   - Fermi bubble lobe angle $\approx 54.7^\circ$ from $3d_{z^2}$ nodal-cone geometry and vertical extent from the 23/27 overhead channel [62, 63, 64, 74].

4. **Conjectured cross-scale equivalences.** Galaxies as hydrogen atoms, stars as electrons, macrophotons as photons, dark matter as lower-scale electron clouds, are proposed as exact fractal-scale correspondences governed by the same computational rules, with only scale parameters changing [8].

5. **Empirical matches and falsifiable predictions.** The framework identifies several observational matches: the 25-arcminute CMB seam at $\theta_c = 1/\alpha^{-1}\,\text{rad}$ in relation to reported SDSS/Planck anomalies [72, 73, 2, 65]; the Karlsson logarithmic quasar spacing [18, 19]; and the Fermi-bubble angle and extent [62, 63, 64, 74]. It also gives a pending falsifiable prediction,
$$\alpha_{\text{Yb}}^{-1} = 137.035998944696,$$
testable by high-precision Yb-174 lattice-clock measurements.

6. **Structural accounts of observational tensions.** The quasar dipole / 94-degree offset [72, 73], the CMB blackbody spectrum and acoustic structure [2], the Hubble tension and JWST early-galaxy problem [66, 67], the baryon-inventory exponent check $4^{137} \sim 10^{82}$, the Fermi bubbles [62, 64], dark matter–neutrino coupling, force unification by upper/lower scale bleed, and reported atomic-clock / α-variation anomalies [38] are interpreted as different projections of the same FTC substrate dynamics.

The central claim is that one finite self-computing architecture produces a compact cluster of otherwise independent-looking quantities that are traditionally treated as free parameters in classical physics. The universe is remarkable because it is fractally self-computational, and all computation has intrinsic costs. These costs, expressed as dimensionless ratios, appear as the fundamental constants of nature.

Continuum-based Physics is a Numerology on the false fundamental laws.

Physical-based Mathiccs is the Arithmancy of the true fundamental law.

The elevation from traditional theoretical mechanisms to a deduction based on reality is why this framework is called **The Fact Of Fractal Tennis**.

References

[1] F. Soddy, "The Hexlet," *Nature* **139**, 77–79 (1937).

[2] Planck Collaboration, "Planck 2018 results. VI. Cosmological parameters," *Astron. Astrophys.* **641**, A6 (2020).

[3] G. W. Gibbons and S. W. Hawking, "Cosmological Event Horizons, Thermodynamics, and Particle Creation," *Phys. Rev. D* **15**, 2738 (1977).

[4] K. Gödel, "Über formal unentscheidbare Sätze der Principia Mathematica und verwandter Systeme I," *Monatsh. Math. Phys.* **38**, 173 (1931).

[5] M. Presburger, "Über die Vollständigkeit eines gewissen Systems der Arithmetik ganzer Zahlen, in welchem die Addition als einzige Operation hervortritt," in *Comptes Rendus du I Congrès de Mathématiciens des Pays Slaves*, Warsaw (1929), pp. 92–101.

[6] B. B. Mandelbrot, *The Fractal Geometry of Nature* (W. H. Freeman, 1983).

[7] L. Nottale, *Scale Relativity and Fractal Space-Time* (Imperial College Press, 2011).

[8] S. E. Elliott, "The Fractal Substrate Equivalence Principle: A Unified Foundation…," vixra preprint (2026). `https://ai.vixra.org/abs/2601.0119`.

[9] Y. Sofue, "Rotation Curve and Mass Distribution in the Galactic Center," *PASJ* **64**(4), 75 (2012).

[10] L. Chemin, C. Carignan, and T. Foster, "Rotation Curve of the Andromeda Galaxy from Combined 21-cm Data," *ApJ* **705**(2), 1395 (2009).

[11] D. W. Boyd, "The Sequence of Radii of the Apollonian Packing," *Math. Comp.* **27**, 653 (1973).

[12] R. L. Graham, J. C. Lagarias, C. L. Mallows, A. R. Wilks, and C. H. Yan, "Apollonian Circle Packings: Number Theory," *J. Number Theory* **100**, 1 (2003).

[13] S. S. Manna and H. J. Herrmann, "Precise Determination of the Fractal Dimensions of Apollonian Packing and Space-Filling Bearings," *J. Phys. A* **24**, L481 (1991).

[14] F. Soddy, "The Kiss Precise," *Nature* **137**, 1021 (1936).

[15] M. Borkovec, W. De Paris, and R. Peikert, "The fractal dimension of the Apollonian sphere packing," *Fractals* **2** (1994), 521–526.

[16] C. L. Wormell and P. Vytnova, "Hausdorff dimension of the Apollonian gasket," *Inventiones Mathematicae* (2024).

[17] G. Ord, "Fractal space-time: a geometric analogue of relativistic quantum mechanics," *J. Phys. A: Math. Gen.* **16**, 1869 (1983).

[18] K. G. Karlsson, "On the existence of preferred redshifts," *Astron. Astrophys.* **13**, 333 (1971).

[19] A. Mal et al., "Periodicity of quasar and galaxy redshift," *Astron. Astrophys.* **643**, A136 (2020).

[20] M. S. El Naschie, "A Review of E-Infinity Theory and the Mass Spectrum of High Energy Particle Physics," *Chaos, Solitons & Fractals* **19**, 209 (2004).

[21] J. P. Lestone, arXiv:physics/0703151 (2007).

[22] J. von Neumann, *Theory of Self-Reproducing Automata*, University of Illinois Press (1966).

[23] S. Wolfram, *A New Kind of Science*, Wolfram Media (2002).

[24] R. Cardona, E. Miranda, and D. Peralta-Salas, "Constructing Turing complete Euler flows in dimension 3," *Proceedings of the National Academy of Sciences* **118**, no. 19 (2021), e2026818118.

[25] R. Cardona, E. Miranda, and D. Peralta-Salas, "Turing universality of the incompressible Euler equations and a conjecture of Moore," arXiv:2104.04356 (2021).

[26] E. Fredkin, "Digital Mechanics," *Physica D* **45**, 254 (1990).

[27] E. Tiesinga, P. J. Mohr, D. B. Newell, and B. N. Taylor, "CODATA recommended values of the fundamental physical constants: 2022," *Reviews of Modern Physics*, vol. 96, 025002, 2024. doi: 10.1103/RevModPhys.96.025002.

[28] R. H. Parker, C. Yu, W. Zhong, B. Estey, and H. Müller, "Measurement of the fine-structure constant as a test of the Standard Model," *Science*, vol. 360, no. 6385, pp. 191–195, 2018. doi: 10.1126/science.aap7706.

[29] L. Morel, Z. Yao, P. Cladé, and S. Guellati-Khélifa, "Determination of the fine-structure constant with an accuracy of 81 parts per trillion," *Nature*, vol. 588, pp. 61–65, 2020. doi: 10.1038/s41586-020-2964-7.

[30] J. D. Laderman, "A noncommutative algorithm for multiplying 3 by 3 matrices using 23 multiplications," *Bulletin of the American Mathematical Society*, vol. 82, no. 1, pp. 126–128, 1976. doi: 10.1090/S0002-9904-1976-13988-2.

[31] I. Newton, *Philosophiæ Naturalis Principia Mathematica* (1687).

[32] KATRIN Collaboration, "Direct neutrino-mass measurement based on 259 days of KATRIN data," *Science* (2025).

[33] Particle Data Group, "Review of Particle Physics," *Phys. Rev. D* **110**, 030001 (2024).

[34] ALEPH Collaboration, "An upper limit on the tau-neutrino mass from three- and five-prong tau decays," *Eur. Phys. J. C* **2**, 395–406 (1998).

[35] NASA/NSSDCA, "Planetary Fact Sheets," Goddard Space Flight Center.

[36] D. S. Spiegel, A. Burrows, and J. A. Milsom, "The Deuterium-Burning Mass Limit for Brown Dwarfs and Giant Planets," *The Astrophysical Journal* **727**, 57 (2011).

[37] I. Esteban, M. C. Gonzalez-Garcia, M. Maltoni, I. Martinez-Soler, J. P. Pinheiro, and T. Schwetz, "NuFit-6.0: Updated global analysis of three-flavor neutrino oscillations," arXiv:2410.05380 (2024).

[38] J. Guéna et al., "Improved Tests of Local Position Invariance Using Rb and Cs Fountains," *Phys. Rev. Lett.* **109**, 080801 (2012).

[39] A. Strominger and C. Vafa, "Microscopic Origin of the Bekenstein-Hawking Entropy," *Physics Letters B* **379** (1996), 99–104.

[40] C. G. Callan and J. M. Maldacena, "D-brane Approach to Black Hole Quantum Mechanics," *Nuclear Physics B* **472** (1996), 591–610.

[41] J. D. Bekenstein, "Black Holes and Entropy," *Physical Review D* **7** (1973), 2333–2346.

[42] S. W. Hawking, "Particle Creation by Black Holes," *Communications in Mathematical Physics* **43** (1975), 199–220.

[43] GRAVITY Collaboration, "The mass distribution in the Galactic Centre from interferometric astrometry of multiple stellar orbits," *Astronomy & Astrophysics* **657** (2022), L12.

[44] J. M. Bardeen and G. T. Horowitz, "The Extreme Kerr Throat Geometry: A Vacuum Analog of $AdS_2 \times S^2$," *Physical Review D* **60** (1999), 104030.

[45] H. K. Kunduri and J. Lucietti, "Classification of Near-Horizon Geometries of Extremal Black Holes," *Living Reviews in Relativity* **16** (2013), 8.

[46] A. P. Porfyriadis, "Near-AdS_2 perturbations and the connection with near-extreme Reissner–Nordström," *Journal of High Energy Physics* **07** (2018), 064.

[47] L. V. Iliesiu and G. J. Turiaci, "The statistical mechanics of near-extremal black holes," *Journal of High Energy Physics* **05** (2021), 145.

[48] G. T. Horowitz, M. Kolanowski, and J. E. Santos, "Almost all extremal black holes in AdS are singular," *Journal of High Energy Physics* **01** (2023), 162.

[49] A. Ciurlo et al., "A population of dust-enshrouded objects orbiting the Galactic black hole," *Nature* **577**, 337–340 (2020).

[50] G. Witzel et al., "Detection of Galactic Center Source G2 at 3.8 μm During Periapse Passage," *Astrophysical Journal Letters* **796**, L8 (2014).

[51] R. Kippenhahn, A. Weigert, and A. Weiss, *Stellar Structure and Evolution*, Springer, 2012.

[52] B. W. Carroll and D. A. Ostlie, *An Introduction to Modern Astrophysics*, 2nd ed., Cambridge University Press, 2017.

[53] I. Labbé et al., "A population of red candidate massive galaxies $\sim$ 600 Myr after the Big Bang," *Nature* **616** (2023), 266–269.

[54] V. Rusakov et al., "JWST's little red dots: an emerging population of young, low-mass AGN cocooned in dense ionized gas," arXiv:2503.16595, 2025.

[55] D. D. Vaida and R. J. Farber, "Little Red Dots: The Assembly of Early Supermassive Black Holes in the JWST Era," arXiv:2601.00089, 2026.

[56] D. J. Fixsen, "The Temperature of the Cosmic Microwave Background," *The Astrophysical Journal* **707** (2009), 916–920.

[57] NASA Goddard Space Flight Center, "CMB Measured Intensity vs Frequency," COBE/FIRAS archive.

[58] E. R. Harrison, *Darkness at Night: A Riddle of the Universe*, Harvard University Press, 1987.

[59] P. S. Wesson, "Olbers' paradox and the spectral intensity of the extragalactic background light," *The Astrophysical Journal* **367** (1991), 399–406.

[60] M. R. Krumholz, "Observing Star-Forming Clouds," in *Star Formation in the Local Universe*, 2010.

[61] N. J. Evans II et al., "Star Formation Occurs in Dense Gas, but What Does 'Dense' Mean?" arXiv:2004.06631, 2020.

[62] M. Su, T. R. Slatyer, and D. P. Finkbeiner, "Giant Gamma-ray Bubbles from Fermi-LAT: AGN Activity or Bipolar Galactic Wind?" *ApJ* **724**, 1044 (2010).

[63] G. Dobler et al., "The Fermi Haze: A Gamma-Ray Counterpart to the Microwave Haze," *ApJ* **717**, 825 (2010).

[64] M. Ackermann et al. (Fermi-LAT Collaboration), "The Spectrum and Morphology of the Fermi Bubbles," *ApJ* **793**, 64 (2014).

[65] Y. Minami et al., "New Extraction of the Cosmic Birefringence from the Planck 2018 Polarization Data," *Phys. Rev. Lett.* **125**, 221301 (2020).

[66] A. G. Riess et al. (SH0ES team), "Latest updates on the Hubble tension from JWST," AAS Meeting #246 (2025).

[67] R. Naidu et al. (JWST/CEERS team), "Improved measurements of the age of JWST galaxies at $z = 6$–10," *MNRAS* (2026).

[68] J. J. Ruan et al., "Toward an Understanding of Changing-look Quasars: An Archival Spectroscopic Search in SDSS," *Astrophysical Journal* **826**, 188 (2016).

[69] C. Ricci and B. Trakhtenbrot, "Changing-look active galactic nuclei," *Nature Astronomy* **7**, 1282–1294 (2023).

[70] Q. Yang et al., "Galaxies Lighting Up: Discovery of Seventy New Turn-on Changing-look Active Galactic Nuclei," *Astrophysical Journal* **980**, 91 (2025).

[71] R. P. Fender and S. E. Motta, "The connection between the fastest astrophysical jets and the spin axis of their black hole," *Nature Astronomy* **9**, 1854–1864 (2025).

[72] N. J. Secrest et al., "A Challenge to the Standard Cosmological Model," *Astrophys. J. Lett.* **937**, L31 (2022).

[73] N. Secrest et al., "Colloquium: The cosmic dipole anomaly," *Rev. Mod. Phys.* **97**, 041001 (2025). arXiv:2505.23526.

[74] K. C. Sarkar, B. Nath, and P. Sharma, "On the origin of the Fermi bubbles," *MNRAS* **453**, 3827 (2015).

[75] D. Lynden-Bell, "Statistical mechanics of violent relaxation in stellar systems," *Mon. Not. R. Astron. Soc.* **136**, 101 (1967).

[76] D. N. Page, "Are Most Particles Gravitons?," arXiv:1605.04351 (2016). Notes that the number of baryons in the observable universe is of order 10^{80}, with photons and neutrinos many orders more numerous.

[77] J.-P. Macquart et al., "A census of baryons in the Universe from localized fast radio bursts," *Nature* **581**, 391–395 (2020). Reports a direct FRB-dispersion census of the cosmic baryon density consistent with CMB and Big Bang nucleosynthesis values.

[78] N. Bohr, "On the Constitution of Atoms and Molecules," *Philosophical Magazine* **26**, 1 (1913).

[79] J. R. Rydberg, "Recherches sur la constitution des spectres d'émission des éléments chimiques," *Kongliga Svenska Vetenskaps-Akademiens Handlingar* **23**, 1 (1890).

[80] F. Evers, A. Aharony, N. Bar-Gill, O. Entin-Wohlman, P. Hedegård, O. Hod, P. Jelinek, G. Kamieniarz, M. Lemeshko, K. Michaeli, V. Mujica, R. Naaman, Y. Paltiel, S. Refaely-Abramson, O. Tal, J. M. van Ruitenbeek, L. Venkataraman, D. H. Waldeck, B. Yan, and L. Kronik, "Theory of chirality induced spin selectivity: Progress and challenges," *Advanced Materials* **34**, 2106629 (2022).

[81] B. P. Bloom, Y. Paltiel, R. Naaman, and D. H. Waldeck, "Chiral induced spin selectivity," *Chemical Reviews* **124**, 1950–1991 (2024).

[82] R. Sala, S. K. Behera, A. R. Karmakar, M. Moioli, R. Martinazzo, and M. Cococcioni, "Spin–orbit coupling and beyond in chiral-induced spin selectivity," arXiv:2601.20475 (2026).

[83] R. B. Griffiths and C.-S. Niu, "Semiclassical Fourier transform for quantum computation," *Physical Review Letters* **76**, 3228–3231 (1996).

[84] J. Chiaverini, D. Leibfried, T. Schaetz, M. D. Barrett, R. B. Blakestad, J. Britton, W. M. Itano, J. D. Jost, E. Knill, C. Langer, R. Ozeri, and D. J. Wineland, "Implementation of the semiclassical quantum Fourier transform in a scalable system," *Science* **308**, 997–1000 (2005).

[85] L. M. K. Vandersypen, M. Steffen, G. Breyta, C. S. Yannoni, M. H. Sherwood, and I. L. Chuang, "Experimental realization of Shor's quantum factoring algorithm using nuclear magnetic resonance," *Nature* **414**, 883–887 (2001).

[86] E. Martín-López, A. Laing, T. Lawson, R. Alvarez, X.-Q. Zhou, and J. L. O'Brien, "Experimental realization of Shor's quantum factoring algorithm using qubit recycling," *Nature Photonics* **6**, 773–776 (2012).

[87] P. W. Shor, "Algorithms for quantum computation: discrete logarithms and factoring," in *Proceedings 35th Annual Symposium on Foundations of Computer Science*, IEEE, 124–134 (1994).

[88] T. Monz, D. Nigg, E. A. Martinez, M. F. Brandl, P. Schindler, R. Rines, S. X. Wang, I. L. Chuang, and R. Blatt, "Realization of a scalable Shor algorithm," *Science* **351**, 1068–1070 (2016).

[89] P. Aumann, M. Fellner, D. Alber, M. Cykiert, C. Fleckenstein, R. ter Hoeven, L. Stenzel, R. J. Valencia-Tortora, and W. Lechner, "Demonstrating record fidelity for the quantum Fourier transform," arXiv:2604.12465 (2026).

[90] U. Skosana and M. Tame, "Demonstration of Shor's factoring algorithm for $N = 21$ on IBM quantum processors," *Scientific Reports* **11**, 16599 (2021).

[91] B. Snios, P. E. J. Nulsen, R. P. Kraft, C. C. Cheung, E. T. Meyer, W. R. Forman, C. Jones, and S. S. Murray, "Detection of Superluminal Motion in the X-Ray Jet of M87," *The Astrophysical Journal* **879**, 8 (2019).

[92] E. T. Meyer, W. B. Sparks, J. A. Biretta, J. Anderson, S. T. Sohn, R. P. van der Marel, C. Norman, and M. Nakamura, "Optical Proper Motion Measurements of the M87 Jet: New Results from the Hubble Space Telescope," *The Astrophysical Journal Letters* **774**, L21 (2013).